

**ULTRAFAST DYNAMICS IN SEMICONDUCTOR
DEVICES**

by

Botao Zhang

B.S., University of Science and Technology of China, 2003

M.S., University of Pittsburgh, 2005

Submitted to the Graduate Faculty of
the Department of Physics & Astronomy in partial fulfillment
of the requirements for the degree of

Doctor of Philosophy

University of Pittsburgh

2010

UNIVERSITY OF PITTSBURGH
DEPARTMENT OF PHYSICS & ASTRONOMY

This dissertation was presented

by

Botao Zhang

It was defended on

October 2010

and approved by

David W. Snoke, Department of Physics & Astronomy

Jeremy Levy, Department of Physics & Astronomy

Kevin P. Chen, Department of Electrical and Computer Engineering

Rob D. Coalson, Department of Chemistry

Vladimir Savinov, Department of Physics & Astronomy

Dissertation Director: David W. Snoke, Department of Physics & Astronomy

ULTRAFAST DYNAMICS IN SEMICONDUCTOR DEVICES

Botao Zhang, PhD

University of Pittsburgh, 2010

This research focuses on three type of GaAs-based semiconductor devices, namely oxide-confined vertical-cavity surface-emitting lasers (VCSEL), GaAs/AlGaAs quantum dots and GaAs microdisk lasers. An individual transverse mode distribution in a VCSEL has been resolved by a scanning confocal microscope in connection with an optical spectrum analyzer. With resonant femtosecond (fs) pulse injection, we directly perturb the cavity field of a VCSEL. After the injection, the lasing and nonlasing mode dynamics are measured. Spatio-temporal resolution of the VCSEL's modes helps us to understand how to lock transverse modes and work toward a new type of mode-locked pulse laser. By injecting cross-polarized laser pulses into a VCSEL cavity, we also studied the ultrafast polarization effects of a single-mode VCSEL. Based on time-resolved microscopic photoluminescence (μ PL) from single self-assembled GaAs/AlGaAs quantum dots, we unambiguously identify one of the emission lines as arising from positive trions (two holes and one electron) in these nominally undoped quantum dots. The trion is formed via tunneling of one electron out of the dot after optical excitation of a biexciton. The rise time of the trion emission line matches the decay time of the biexciton due to electron tunneling. Time-resolved whispering-gallery modes (WGMs) of GaAs microdisk lasers show a red-shift in time. After the fs laser pulse pump, there is a turn-on delay of the microdisk laser lasing emission. With the increasing pump power, the WGMs shift to shorter wavelength.

TABLE OF CONTENTS

| | |
|---|----|
| PREFACE | xi |
| 1.0 INTRODUCTION | 1 |
| 1.1 Overview | 1 |
| 1.2 Semiconductors | 2 |
| 1.2.1 Semiconductor Optics | 4 |
| 1.2.2 Semiconductor Heterostructures | 9 |
| 1.3 Quantum Dots | 14 |
| 1.4 Semiconductor Diode Lasers | 15 |
| 1.4.1 The Principle of Operation | 15 |
| 1.4.2 Vertical-cavity Surface-emitting Lasers | 16 |
| 2.0 EXPERIMENTAL SETUP | 21 |
| 2.1 Optical Spectroscopy | 21 |
| 2.2 Ti:Sapphire Lasers | 22 |
| 2.2.1 Why Ti:Sapphire crystal? | 22 |
| 2.2.2 Producing ultrafast pulses | 23 |
| 2.2.2.1 Q-switching | 23 |
| 2.2.2.2 Mode-locking | 25 |
| 2.2.3 Dispersion compensation | 31 |
| 2.2.4 Ti:Sapphire laser oscillator design | 34 |
| 2.3 Pulse Shaping | 41 |
| 2.3.1 Actively stabilized double pulse generation | 41 |
| 2.3.2 Double-color double pulse generation | 44 |

| | | |
|----------------------------------|--|-----------|
| 2.3.3 | Pulse measurements | 48 |
| 2.4 | Time-Resolved Experiment Setups | 49 |
| 2.4.1 | ULTRAFAST NONLINEAR OPTICAL SAMPLING OSCILLOSCOPE | 49 |
| 2.4.2 | Streak Camera | 54 |
| 3.0 | QUANTUM DOTS | 58 |
| 3.1 | Trion Formation In GaAs-AlGaAs Quantum Dots By Tunneling | 58 |
| 3.2 | Rabi Oscillations | 65 |
| 4.0 | VCSEL MODES | 72 |
| 4.1 | Transverse-Modes And Mode-Locking | 72 |
| 4.2 | Ultrafast Switching Dynamics of Nonlasing Modes of Vertical-Cavity Surface-Emitting Lasers | 79 |
| 5.0 | CONCLUSIONS AND FUTURE WORK | 87 |
| APPENDIX. MICRODISK LASER | | 89 |
| A.1 | Whispering Gallery Modes | 89 |
| A.2 | Time Dependent Measurements | 92 |
| BIBLIOGRAPHY | | 95 |

LIST OF FIGURES

| | | |
|----|--|----|
| 1 | The Brillouin zones. | 3 |
| 2 | (a) Face-centered cubic bravis lattice. (b) GaAs lattice. The images are taken from Ref. [1] | 5 |
| 3 | (a) The first Brillouin zone of fcc lattice; (b) Calculated electron energy band structure of GaAs [2] | 6 |
| 4 | The schematic band structure of GaAs around Brillouin zone center. | 6 |
| 5 | Direct transition and indirect transition. | 7 |
| 6 | (a) Density of states $g(E)$ for semiconductor in the 3D case; (b) Fermi-Dirac distribution for electron; (c) Number of quasi-particles per energy dN/dE | 8 |
| 7 | (a) A simple band structure for p-doped and n-doped semiconductor. (b) The band structure for p-n junction. | 10 |
| 8 | Heterojunction between two different undoped semiconductor materials. | 11 |
| 9 | GaAs/AlGaAs quantum well band structure. | 11 |
| 10 | The schematics of density of states for 2D electron gas, where the dotted lines are for 3D case. | 13 |
| 11 | GaAs/AlGaAs superlattice band structure. | 13 |
| 12 | Schematics of the density of states in 3D, 2D, 1D and 0D cases. | 14 |
| 13 | The double-heterostructure of a diode laser. | 16 |
| 14 | The schematics of an edge-emitting diode laser. | 17 |
| 15 | The field confinement for an edge-emitting laser and a vertical emitting laser. | 18 |
| 16 | The schematics of different VCSEL structures [3]. | 20 |

| | | |
|----|--|----|
| 17 | (a) The absorption cross sections and (b) the fluorescence spectra of a Ti:Sapphire crystal for different polarization. The images are taken from [4] | 24 |
| 18 | The schematics of Ti:Sapphire energy level 2T_2 and 2E transition. | 24 |
| 19 | The operation principle of the Q-switched laser. A periodic modulation of the cavity loss will produce pulsed emission when gain > loss. | 26 |
| 20 | The basic idea of mode-locking. The blue curve shows a pulse with 10 modes locked and the green curve shows a pulse with 20 modes locked. The pulse width of the green curve is half of that of the blue curve. | 27 |
| 21 | The Kerr lensing effect in the gain medium. The pulsed emission is focused much tighter than the CW emission. | 28 |
| 22 | The principle for (a) a slow saturable absorber, where the slow loss modulation alone can only shorten the leading edge of a pulse and a dynamic gain modulation cut off the trailing edge of a pulse; (b) a fast saturable absorber, where the gain relaxation is slow and treated as a constant, and the fast loss modulation can produce the pulse alone. [5] | 30 |
| 23 | The self-phase modulation effect when a Gaussian pulse passes through a Kerr medium. (a) The intensity profile associated with a Gaussian pulse; (b) the nonlinear refractive-index-induced frequency change with the time for the Gaussian pulse. | 32 |
| 24 | The electric field of a Gaussian pulse with (a) no dispersion (b) positive dispersion. | 33 |
| 25 | A prism pair with a folding mirror or four prisms setup for dispersion compensation. The first prism disperses the input beam and the second prism collimates the beam. | 34 |
| 26 | A schematic of (a) a Bragg reflector (b) a simple chirped mirror. | 35 |
| 27 | The simple schematic of Ti:Sapphire laser oscillator. | 37 |
| 28 | The equivalent two mirror cavity for Fig. 27. | 37 |
| 29 | The schematic setup of Ti:Sapphire oscillator with chirped-mirror-only design. | 39 |

| | | |
|----|---|----|
| 30 | A typical spectrum measurement for a pulse with a FWHM on the order of 10 fs (a typical pulse width measurement as shown in Fig. 40) from chirped mirror based cavity. | 39 |
| 31 | The schematic setup of tunable Ti:Sapphire oscillator with prism-pair design. | 40 |
| 32 | The computer-based stabilized double-pulse generation. | 42 |
| 33 | (a) The measured signal from the quadrant photodiode for X and Y detector. (b) The measured ellipse based-on the X and Y signals, which works as the phase reference. | 43 |
| 34 | A measured phase-reference ellipse can be transformed into a simple ellipse. | 45 |
| 35 | The schematic setup for two-color double pulse generation. | 45 |
| 36 | The shaped spectra. | 47 |
| 37 | A typical two-color double-pulse measurement after the pulse shaper. | 48 |
| 38 | The autocorrelator setup. | 50 |
| 39 | A interferometric autocorrelation measurement for a laser pulse with center wavelength at 850 nm. | 51 |
| 40 | The interferometric autocorrelation of a chirped short pulse which is generated by our chirped-mirror-only cavity. | 51 |
| 41 | The pump-probe experiment setup for the VCSEL experiments. | 52 |
| 42 | A typical image of a single-mode VCSEL device. | 55 |
| 43 | The operation principle of streak camera. (The picture is from Hamamatsu.) | 55 |
| 44 | The streak camera experiment setup for quantum dots experiment. | 56 |
| 45 | Time-resolve μ PL measurements of high density QD samples with different barrier thicknesses of $D =$ (a) 10 nm, and (b) 7 nm. (c) The decay dynamics for both samples, where the solid white lines are exponential fits. The pump power is 200 μ W. (d) The process of a biexciton (XX) turning into a positive trion (X^+) by electron tunneling. | 61 |

| | | |
|----|---|----|
| 46 | Time-resolved μ PL for single QD's. (a), (b) and (c) are streak camera images for pump powers of $40\mu W$, $80\mu W$ and $160\mu W$, respectively (The dark line at time zero is scattered light. The intensity is normalized in each image); (d), (e) and (f) are decay dynamics of exciton (X), biexciton (XX) and positive trion (X+), respectively, where the black dots are experimental data and the solid white curves are simulations from the rate equations (3.4). | 62 |
| 47 | A two-dimensional photoluminescence excitation (PLE) measurement on a single quantum dots. The horizontal axis shows excitation wavelength, whereas the vertical axis is the emission spectra. | 66 |
| 48 | A photoluminescence excitation measurement on a single quantum dots. | 68 |
| 49 | A rabi oscillation measurement on a single quantum dots. | 69 |
| 50 | Numerical simulation of Rabi oscillation vs. pump laser frequency detuning. | 70 |
| 51 | The schematics of experiment setup. | 73 |
| 52 | A typical emission spectrum of a multitransverse mode VCSEL at a bias current of 8 mA. | 74 |
| 53 | The spatial-spectrally resolved VCSEL's transverse mode at bias current 8.0 mA. | 74 |
| 54 | a) The first six order of LG modes calculated from equation (4.1). b) Moving spots generated by interference of the six lowest order LG daisy modes. The diagram shows the calculated intensity versus position on a mode-locked VCSEL for constant time steps between $t = 0$ and $1/(2\delta v)$, the time it takes the spots to move half the circle. | 76 |
| 55 | (a) Experimental frequency difference between adjacent LG modes at bias current 8 mA for the modes shown in Fig. 53. (b) Theoretically calculated time-resolved emission from the center strip of the VCSEL with modes shown in Fig. 53. | 78 |
| 56 | The streak camera image of a VCSEL's emission (the slice of the VCSEL as shown on the left) after a laser pulse injection at one of the VCSEL emission mode maxima. This VCSEL has broader active region than the VCSEL used in Fig. 53 and 55. | 78 |

| | | |
|----|---|----|
| 57 | The schematics of the optical up-conversion pump-probe experiment setup. . . | 80 |
| 58 | Continuous-wave emission spectra of a single-mode VCSEL below (thin line) and above (heavy line) the lasing threshold. Inset images: near-field emission patterns for (a) below, and (b) above threshold. The intensities do not have the same scale. | 82 |
| 59 | Time-resolved emission of the VCSEL's nonlasing modes after optical injection at one of the lasing emission maximum, where the strong spikes in the (a) are reflected pump laser pulses. | 83 |
| 60 | (a) and (b) are the Fourier transform of Fig. 59 (a) and (b), respectively. . . | 84 |
| 61 | Time-resolved emission dynamics of a VCSEL for different injection currents after optical femtosecond pulse injection that is sufficiently weak (~ 0.8 pJ) to reduce relaxation oscillation. The black solid lines are exponential fittings. Inset: Fitted decay rate versus current, for the times after 20 ps. The spike at 20 ps is an artifact of reflected light from the back surface of a reflective neutral-density filter. | 86 |
| 62 | A cartoon of whispering gallery modes. | 90 |
| 63 | Simulated whispering gallery modes. | 91 |
| 64 | The measured whispering gallery modes image with different pump location, (a) on the disk center and (b) on the edge of the disk. | 92 |
| 65 | Time resolved whispering gallery modes. | 94 |

PREFACE

This PhD journey definitely influences me most in the future. Without the help and support from others, I certainly can not finish this degree.

I'd like to thanks for Dr. Albert P. Heberle, who mentored me at the beginning of my graduate study. His expertise in lasers and hands-on experience benefitted me a lot in the following research projects.

Much thanks to my advisor Prof. Snoke. His patience and knowledge in physics really guided me through my final stage of the study. It will be an invaluable part of my education.

During these years of graduate school, I get tremendous help from my colleagues and other professors. I can not name all of them here. A special thank to Prof. Jeremy Levy's group and Prof. Hrvoje Petek's group.

This thesis would not have been possible if not for my families, especially my wife, Siyu. Your constant encouragement and support help me conquer challenges in the study and the life.

I also want to thank all my friends. My life is so much enjoyable with you.

Finally, thank you to my committee members, Prof. David W. Snoke, Prof. Jeremy Levy, Prof. Kevin P. Chen, Prof. Rob D. Coalson and Prof. Vladimir Savinov for being kind inquisitioners and thorough readers.

1.0 INTRODUCTION

1.1 OVERVIEW

At the heart of modern human life, communication plays a very important role. Nowadays, people get connected over the internet, such as Facebook, mySpace, twitter or online journals etc. We share information and knowledge in a brand new virtual world. People want to get resources over the internet as fast as possible, which demands more bandwidth and faster devices. In the mobilized 21th century, people also want to access resources anywhere they can go. Therefore, we need highly compact solid-state devices which process information very fast. The advance of information technology lies in the advance of semiconductor materials. To make the full use of semiconductor materials, we first need to know what are the properties of these materials and why devices based on these materials give expected functionalities. In another word, we need to understand the underlying physics of systems.

Since Planck proposed quantized black body emission and Einstein explained intrinsic quantization of electromagnetic field through the famous photoelectric effect, quantum mechanics soon became the foundation of modern physics. It brought a new vision of the microscopic world such as atoms, photons, phonons etc. The work presented here is mainly concerned with the interaction of light and matter in solid-state semiconductor systems. The elemental semiconductor Si accounts for most applications and commercial products due to more advanced processing technology of its oxide [6]. On the other hand, compound semiconductors such as GaAs are more promising for high speed electronic devices due to the high mobility of the charge carriers (e.g. electrons and holes) [2]. The ability to emit light and engineer the bandgap are two other very import properties of these compound semiconductors. For example, the direct bandgap of GaAs makes light emission very efficient and gave

birth to the first semiconductor laser in 1962 [7]. Since then, GaAs became commercially popular and attracted great interest as regards the investigation of the interaction between light and semiconductor materials.

The lack of proper carrier confinement limited the performance of early GaAs homo-junction lasers. Therefore, the double heterostructure was proposed to increase population inversion and confine carriers inside the active region[8, 9]. Semiconductor heterostructures are also essential for making micro- or nano-scale electronic and photonic devices. With the development of molecular beam epitaxy(MBE) [10] and metal organic vapour deposition (MOCVD) [11], monolayer accurate semiconductor films could be grown with high purity and uniformity, which paved the way to produce quantum-well active medium regions. Semiconductor lasers with quantum-well active media have lower threshold current and higher inversion efficiency which gives higher gain. The fast-evolving heteroepitaxy technology and lithography techniques allow many new quantum-based electronic and photonic devices. These devices are usually reduced-dimensional systems in which carriers are confined in one or more directions on the size of a few nanometers (nm). When the confined size is comparable to the electron's De Broglie wavelength, systems will show strong quantum effects. The systems studied here are based on quantum wells or quantum dots which are two-dimensional (2D) and zero-dimensional (0D) systems respectively.

1.2 SEMICONDUCTORS

Most semiconductors are crystals which have periodic placement of atoms. Each atom also contains many electrons. The energy levels of the electrons in an individual atom are discrete and sharp. When atoms form crystal, the distance between adjacent atoms is only around a few tenths of a nanometer. The electron wavefunctions start to have significant overlap and cause energy splitting which leads to the so-called band structure [12]. A lot of semiconductor properties are closely related to the band structure. Since the crystal lattice structure is periodic, we can solve the band structure much more easily. Fig. 1 gives a general idea of periodic electron band structure which is calculated by the Kronig-Penney model [12] for

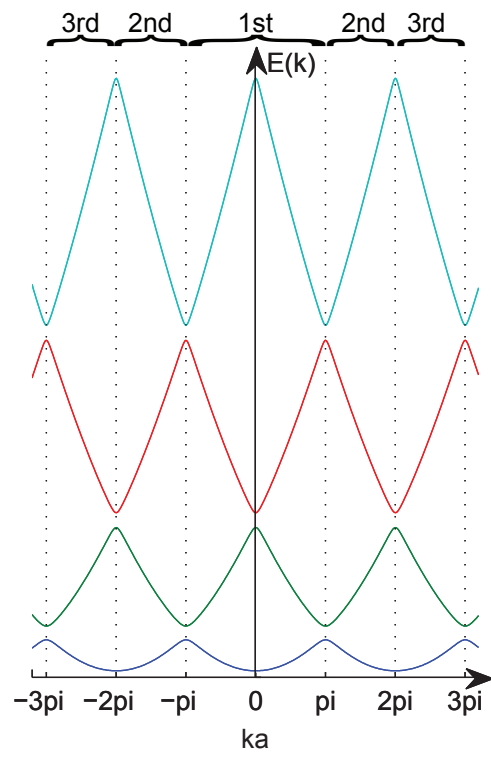


Figure 1: The Brillouin zones.

an infinite periodic one-dimensional structure. The calculation for the three-dimensional (3D) crystal band structure needs more sophisticated models and methods such as the tight-binding approximation, the nearly-free electron approximation and $k \cdot p$ theory, etc. The band structure of a semiconductor is similar to that of an insulator. They have fully filled energy bands called valence bands (VB). Above the valence bands, all the bands are empty, and are called conduction bands (CB). Between the energy of highest valence band and that of lowest conduction band, there is a band gap. GaAs has the Zincblende structure which can be treated as a gallium face-centered cubic (fcc) lattice (Fig. 2a) and an arsenic fcc lattice combined. As shown in Fig. 2b, each atom is bonded to four equidistant nearest neighbors forming a tetrahedron. The first Brillouin zone of the fcc lattice is shown in Fig. 3a. The GaAs electron band structure has been calculated (Fig. 3b). There are four subbands in the valence band. At Γ , the Brillouin zone center, GaAs also features a direct bandgap which means optical transitions are possible without assistance from phonons.

1.2.1 Semiconductor Optics

In a semiconductor, most properties are determined by the electrons at the top of valence band and the bottom of conduction band. In a direct-gap semiconductor, we only need to consider the edges of the VB and CB around $k = 0$ (the Brillouin zone center). In the second-order approximation, we write the electron energy, $E(k)$, as [1]

$$E(k) = E(0) + \frac{\hbar^2 k^2}{2m^*} \quad (1.1)$$

where $m^* = \frac{\hbar^2}{d^2 E / dk^2}$ is known as the electron effective mass.

Fig. 4 plots the schematic band structure of GaAs around the Brillouin zone center. The bands are parabolic and the valence bands have two branches, each of which has two spin states. At temperatures with $k_B T$ well below the gap energy, the VB of GaAs is filled with electrons and the CB is empty. However, we can use optical excitation to remove electrons from the VB and put them into the CB as long as the photon energy $\hbar\omega$ satisfies

$$\hbar\omega \geq E_g, \quad (1.2)$$

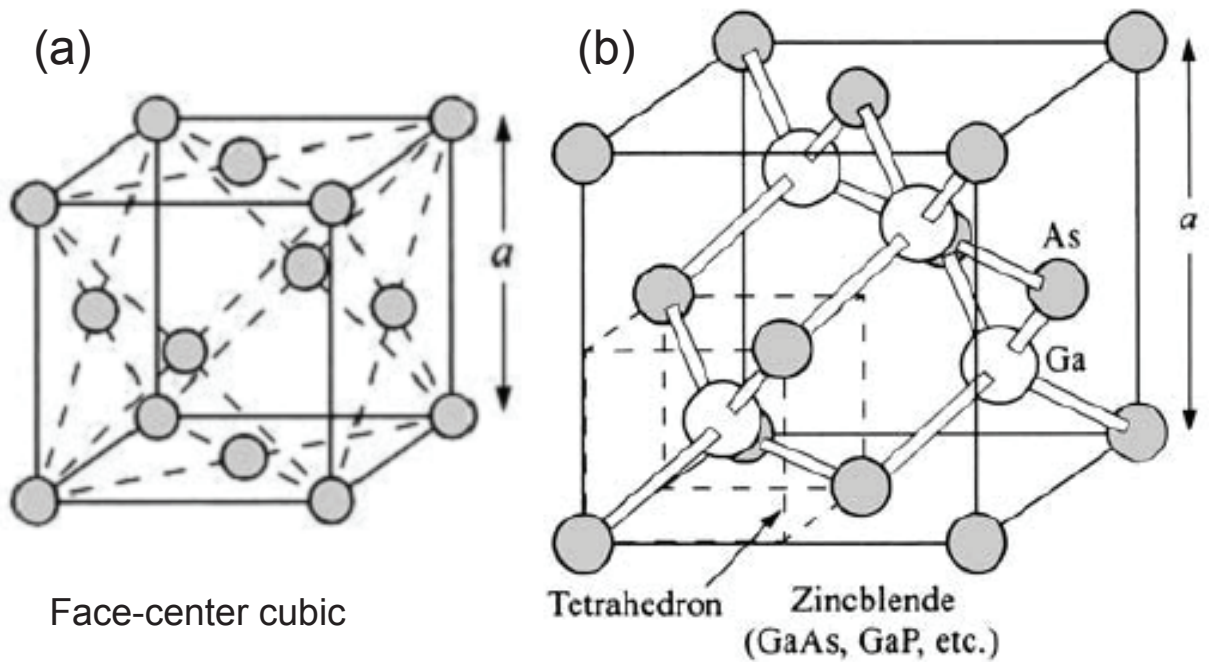


Figure 2: (a) Face-centered cubic bravis lattice. (b) GaAs lattice. The images are taken from Ref. [1]

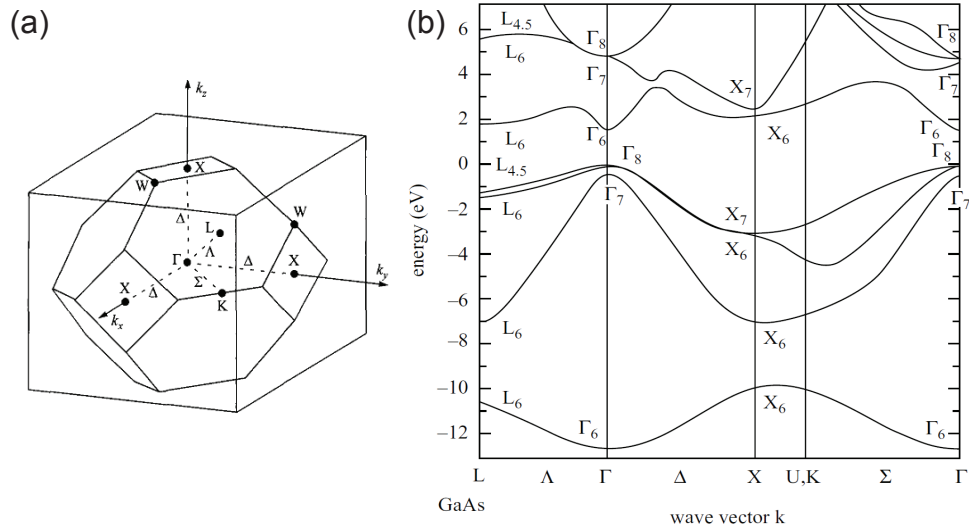


Figure 3: (a) The first Brillouin zone of fcc lattice; (b) Calculated electron energy band structure of GaAs [2]

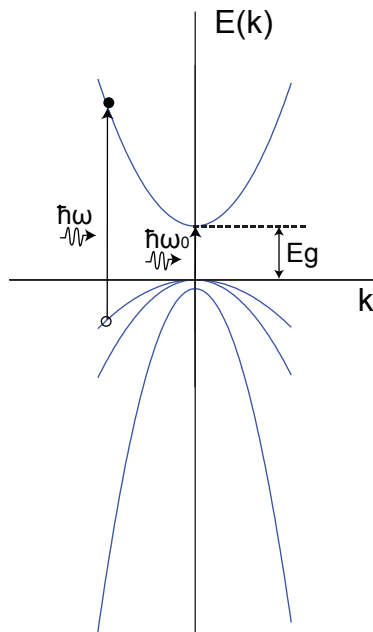


Figure 4: The schematic band structure of GaAs around Brillouin zone center.

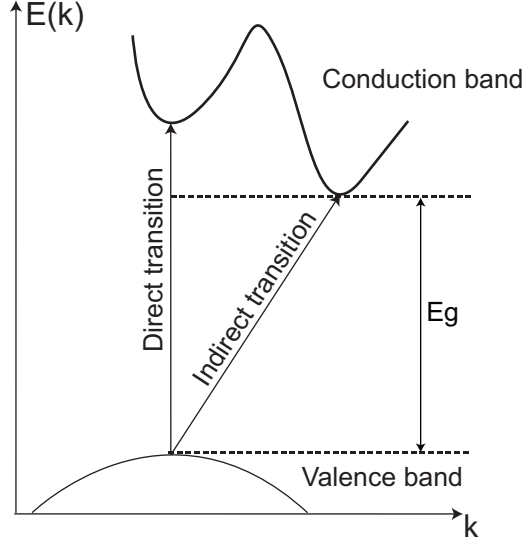


Figure 5: Direct transition and indirect transition.

where E_g is the band gap of GaAs, which is 1.519 eV at 0 K [1]. An empty state in the VB is called a hole in the quasiparticle picture.

An electron in a VB \mathbf{k} state absorbs a photon and jumps to a CB \mathbf{k}' state. Besides the energy conservation, the momentum must be conserved:

$$\hbar\mathbf{k}' - \hbar\mathbf{k} = \mathbf{P}_{photon}. \quad (1.3)$$

The photon momentum is very small compared to electron momentum. Therefore, Eq. (1.3) can be approximated as

$$\mathbf{k}' = \mathbf{k}, \quad (1.4)$$

which is called a direct transition.

An indirect transition is one in which an electron either absorbs or emits a phonon in order to change to different \mathbf{k} state:

$$\hbar\mathbf{k}' - \hbar\mathbf{k} = \mathbf{P}_{photon} \pm \hbar\mathbf{q}, \quad (1.5)$$

where $\hbar\mathbf{q}$ is the momentum of a phonon, as shown in Fig. 5. The indirect transition is actually a two body process which has less probability compared to the direct transition.

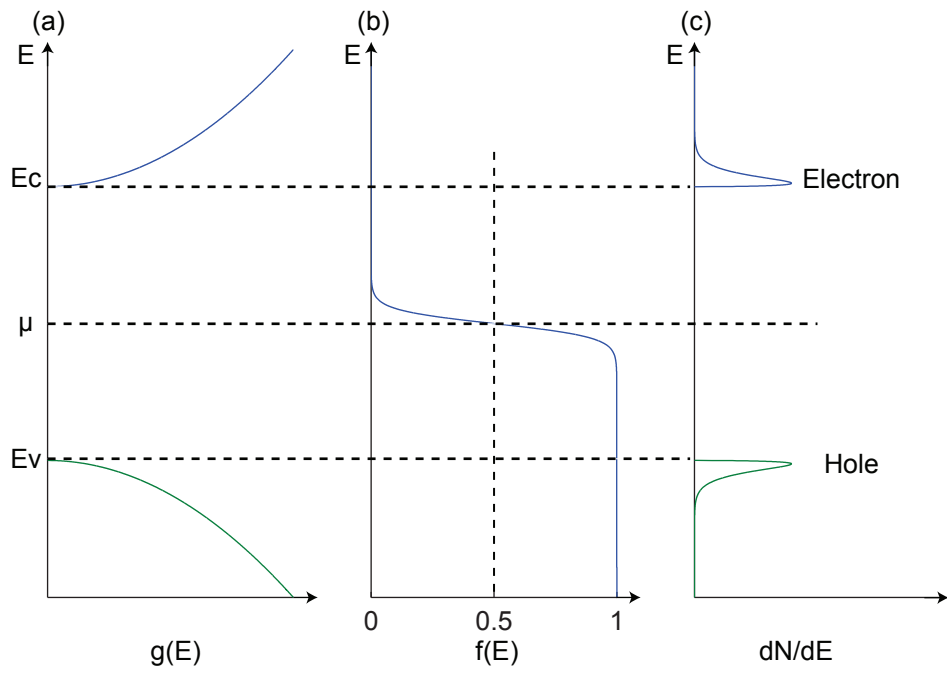


Figure 6: (a) Density of states $g(E)$ for semiconductor in the 3D case; (b) Fermi-Dirac distribution for electron; (c) Number of quasi-particles per energy dN/dE .

Most interesting optical effects are determined by electrons at the edge of each band which is close to the band gap. At a finite temperature $T \neq 0$, electrons of the VB can be excited to the CB by interacting with the lattice and reach a dynamic equilibrium. To understand the distribution of carriers, we need to know the carrier density of states, which is given by [12]:

$$g(E) = \frac{V}{(2\pi)^3} \int d^3k \delta(E_k - E) \quad (1.6)$$

The important states are around the edge of the band, $E(k)$ is given by Eq. (1.1). For the isotropic case, we have:

$$g(E) = \frac{V}{2\pi^2} \frac{(2m^*)^{3/2}}{\hbar^3} (E - E_0)^{1/2} \quad (1.7)$$

Furthermore, the occupation number of the electron state with a energy E , is given by the Fermi-Dirac statistics:

$$f(E) = \frac{1}{1 + \exp(\frac{E-\mu}{k_B T})} \quad (1.8)$$

where the μ is the chemical potential of the fermi gas. Therefore, the number of quasi-particles between E and $E+dE$ is:

$$\frac{dN}{dE} = g(E)f(E) = \frac{V}{2\pi^2} \frac{(2m^*)^{3/2}}{\hbar^3} \frac{1}{1 + \exp(\frac{E-\mu}{k_B T})} (E - E_0)^{1/2}. \quad (1.9)$$

Fig. 6 plots the schematic electron density of states for bulk materials with direct band gap. As we see, electrons in the conduction band and holes in the valence bands mostly distribute at the edges of the bands.

1.2.2 Semiconductor Heterostructures

One of the most important heterostructures is the p-n junction which forms at the interface of a p-doped semiconductor and an n-doped semiconductor [13]. As shown in Fig. 7a, the Fermi level E_{Fn} of an n-type semiconductor is very close to the donor level E_D and the Fermi level E_{Fp} is very close to the acceptor level E_A . In the junction area, electrons flow from the n-type area to the p-type area since $E_{Fp} \geq E_{Fn}$. In equilibrium, the two materials have the same Fermi level and the bands of p-type material are raised by $qV_D = q(E_{Fn} - E_{Fp})$. This kind of band bending effect gives the ability to tailor the band structure of semiconductor heterostructure with advanced fabrication techniques.

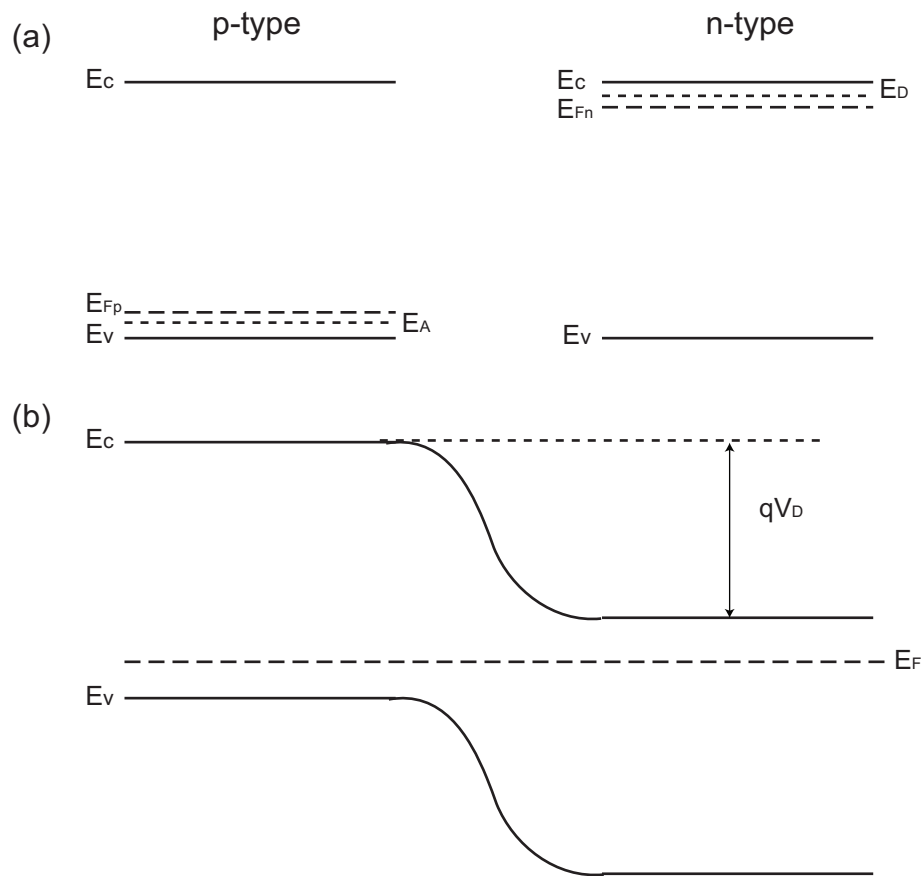


Figure 7: (a) A simple band structure for p-doped and n-doped semiconductor. (b) The band structure for p-n junction.

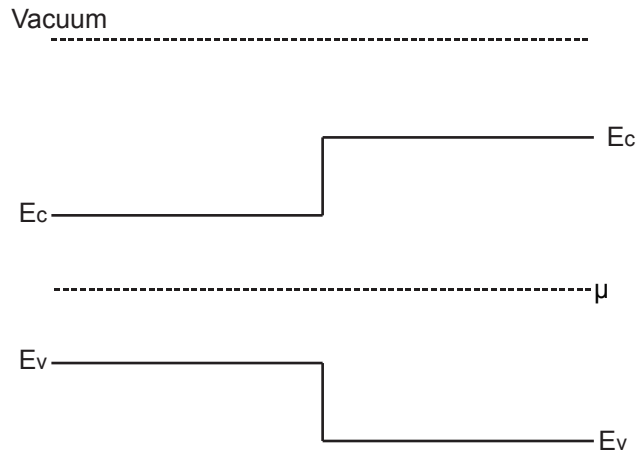


Figure 8: Heterojunction between two different undoped semiconductor materials.

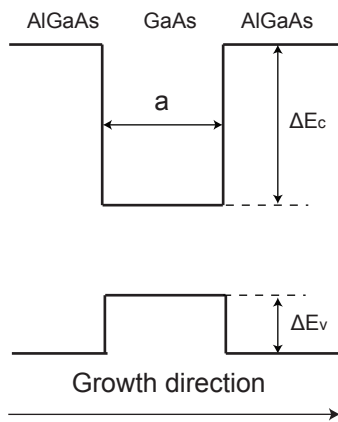


Figure 9: GaAs/AlGaAs quantum well band structure.

Another type of heterojunction is at the interface of two undoped semiconductors with different band gaps E_g , as shown in Fig. 8. This type of heterojunction produces a pretty sharp band offset at the interface. One problem for this heterostructure is the lattice mismatch which causes strain at the interface and can affect device functionality. Fortunately, the lattice constants of GaAs and AlGaAs match very well. With modern epitaxy technology, the thickness of semiconductor thin films can be controlled with atomic accuracy. Based on this type of heterojunction, GaAs/AlGaAs quantum well structures have been developed [14], as shown in Fig. 9. Electrons can freely move along the plane parallel to the interface. These electrons are often called a two-dimensional electron gas [14]. Along the growth direction, electrons are confined by a one-dimensional potential well. When the barrier is infinite, the confinement energy is:

$$E_z = E_n = \frac{\pi^2 \hbar^2 n^2}{2m^* a^2}, \quad (1.10)$$

where n is an integer, m^* is the effective mass and a is the quantum well width in the growth direction. The total energy of the electron is:

$$E = E_z + E_{xy} = E_n + \frac{\hbar^2 k_{\parallel}^2}{2m^*}. \quad (1.11)$$

We can tune the confinement energy by controlling the width of the quantum well. In the 2D system, the density of states also changes, which is given by [1]:

$$g(E) = \frac{m^* A}{\pi \hbar^2} \sum_n \Theta(E - E_n - E_{k_{\parallel}}) \quad (1.12)$$

where

$$\Theta(x) = \begin{cases} 1 & \text{if } x > 0 \\ 0 & \text{if } x \leq 0 \end{cases}. \quad (1.13)$$

As shown in Fig. 10, the density of states is stair-case like for a 2D electron (or hole) gas. Over a certain energy range, $g(E)$ is constant. In most devices, there are usually several quantum wells stacked together (Fig. 11). If the barrier is thick, we can treat each quantum well separately. On the other hand, when the barrier is thin enough, wave functions of the wells start to overlap. Similar to atoms forming a crystal lattice, multiple quantum wells form a so-called heterostructure superlattice when the barriers between quantum wells and the electron wavefunction of individual quantum well start to overlap. As a consequence, the confined energy levels split and form an energy band structure.

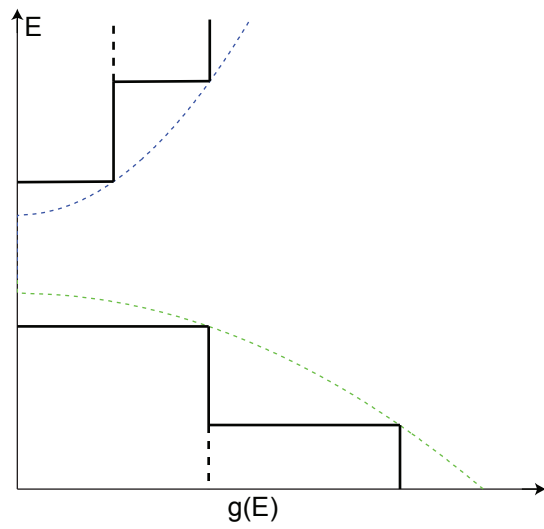


Figure 10: The schematics of density of states for 2D electron gas, where the dotted lines are for 3D case.

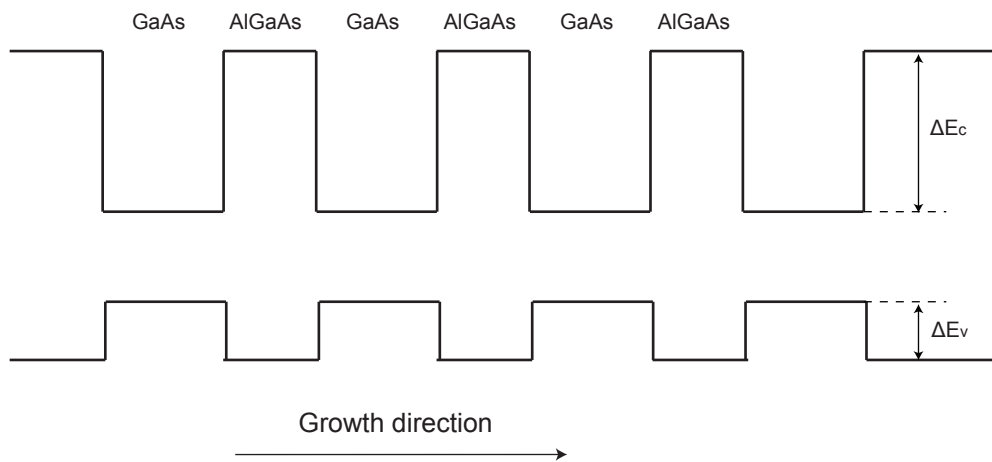


Figure 11: GaAs/AlGaAs superlattice band structure.

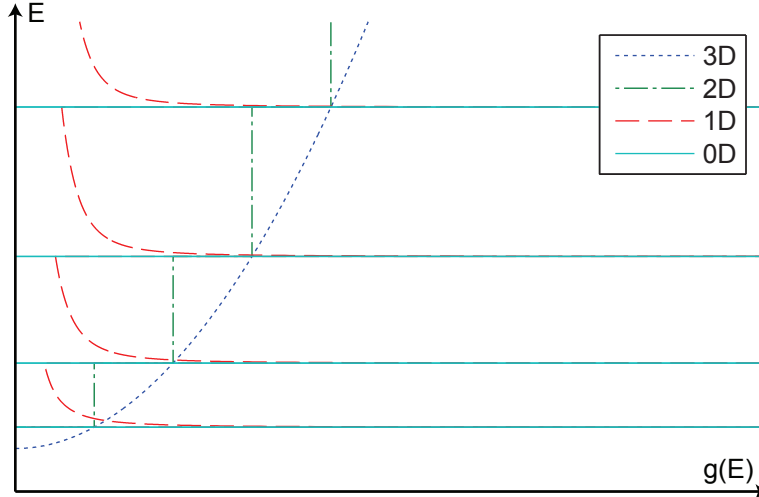


Figure 12: Schematics of the density of states in 3D, 2D, 1D and 0D cases.

1.3 QUANTUM DOTS

One step further, if we confine the 2D electron gas in the lateral directions to tens of nanometers, the system will be zero dimensional (0D). This kind of 0D system is known as quantum dots. Semiconductor quantum dots usually embed in semiconductor heterostructures. Semiconductor quantum dots can be engineered to confine a few electrons or just a single electron. With strong quantum confinement in all three dimensions, semiconductor quantum dots exhibit atom-like sharp electron energy states, as shown in Fig. 12. Therefore, semiconductor quantum dots act like artificial atoms (although quantum dots usually contain thousands of atoms). Electron spin can be controlled through external magnetic field, which makes quantum dots a building block of quantum information and quantum computations.

There are many types of semiconductor quantum dots, such as colloidal nanocrystals made by chemical synthesis, interfacial fluctuation quantum dots and self-assembled quantum dots (SAQD) etc. One of most popular SAQD is self-assembled InAs quantum dots which are grown by the Stranski-Krastanow (SK) growth method [15]. In the SK growth mode, the crystal is grown layer-by-layer. At a certain critical thickness, a 3D crystal island will form at

the surface of the film depending on the lattice mismatch and chemical potential of the film. Therefore, by controlling the thickness and the composition of the film, we can modify the size and shape of the 3D crystal islands. In other words, we can engineer the electronic band structure of the 3D crystal islands. In this work, we studied self-assembled GaAs quantum dots. Since the lattice mismatch between GaAs and AlGaAs is very small, the traditional SK growth mode will not work here. Our collaborators have developed a new method [16] based on the SK growth method, called the hierarchically self-assembled method, which produces high quality and strain-free GaAs quantum dots. Detailed discussion will be given in the following chapter.

1.4 SEMICONDUCTOR DIODE LASERS

Over the past few decades, semiconductor lasers have become a standard light source in many applications such as optical communication networks, spectroscopy, printing and optical storage etc. Thanks to the advance of semiconductor processing technology, semiconductor lasers can be integrated into a very small package. They are pumped directly by current sources and have up to 50% conversion efficiency. On the other hand, regular gas lasers or solid state lasers only have a few percent efficiency. Despite the compact size of semiconductor diode lasers, they can produce tremendous power (a few hundred watts). One of the critical issues for light sources is the aging problem. Unlike other laser sources, semiconductor lasers can last many years without degrading in performance.

1.4.1 The Principle of Operation

Most semiconductor diode lasers are based on the quantum-well heterostructure [17], as shown in Fig. 13. A thin film of undoped GaAs works as the active medium for gain surrounded by undoped AlGaAs, and is located in between p-doped and n-doped AlGaAs slabs. Since the band gap of AlGaAs is larger than that of GaAs, there will be confinement inside the GaAs film. With the proper forward bias, electrons and holes from n-doped and p-

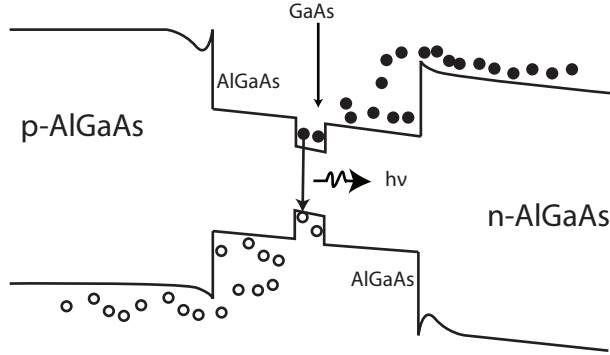


Figure 13: The double-heterostructure of a diode laser.

doped AlGaAs flow to the confined area of GaAs. Unlike a silicon-based transistor, electrons and holes will recombine and emit photons efficiently due to the direct bandgap of GaAs. On the other hand, the emitted photons can not be absorbed by the barrier material because of the larger bandgap compared to the active medium, GaAs. To form a laser, stimulated emission is required to amplify the photon emission. An optical resonant cavity is the key way to provide enough optical feedback. In the case of an edge-emitting diode laser, two cleaved facets can provide about 30% reflectivity at the interface between GaAs and air; these facets act as effective mirrors and form an optical resonant cavity for laser operation. Practically, a laser source also requires lateral confinement in the active medium region. Proper lateral confinement provides guiding for current, carriers and photons and make the laser more energy efficient. Fig. 14 is a typical schematic structure of an edge-emitting laser. The narrow top contact limits lateral spreading of the injection current. At the semiconductor-air interface of the etched pillar shape, the large refraction index difference gives optical guiding.

1.4.2 Vertical-cavity Surface-emitting Lasers

The vertical-cavity surface-emitting laser (VCSEL) is another type of semiconductor laser. In contrast to traditional edge-emitting lasers (EEL), a VCSEL's cavity is perpendicular to the direction of wafer growth. This kind of vertical cavity structure not only makes a VCSEL

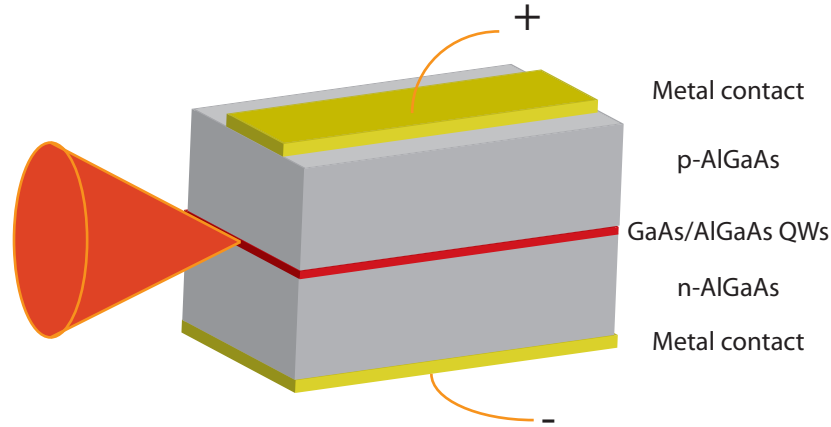


Figure 14: The schematics of an edge-emitting diode laser.

easily integrated with a two-dimensional system, but it also saves manufacturing cost with on-die testing. Another advantage of this vertical cavity is that it enables lower threshold current than that of an EEL due to the fact that the active gain medium covers the whole length of the EEL's cavity. A VCSEL usually has a circular emission window which makes it ideal for coupling to optical fibers. Fig. 15 shows the field confinement for an edge-emitting laser and a vertical-emitting laser.

A typical VCSEL structure contains top and bottom distributed Bragg reflectors (DBR) which have greater than 99% reflectivity and form the VCSEL cavity. Multiple quantum wells are sandwiched in the center of the cavity as the gain medium. In this particular case, the oxide aperture confines the carriers and current laterally. The light emits at the top of the VCSEL.

There are four types of VCSEL structure depending on how the device implements the lateral confinement [3]. Fig. 16(a) shows an etched mesa structure [18]. It is similar to an EEL but has two-dimensional lateral confinement. Since there is no confinement inside the structure, the injected current freely moves in the lateral direction, which creates current leakage for a small size structure. Imperfections of the structure surface can impose higher loss on high-order laser modes. The proton implanted structure [18] in Fig. 16(b) has better

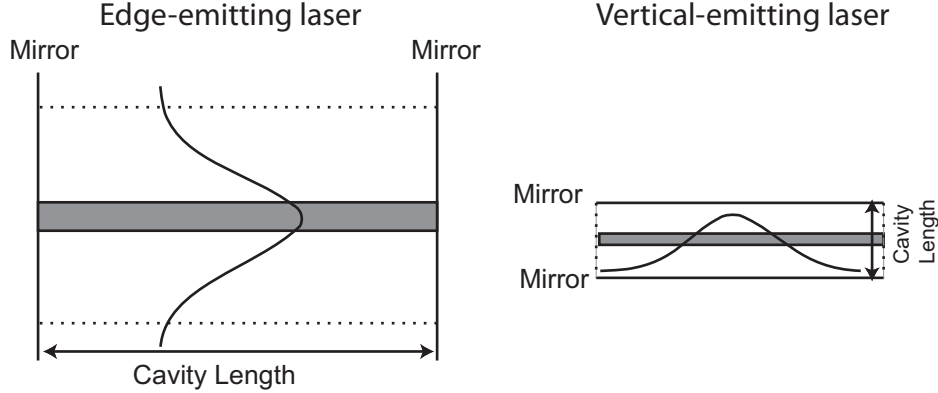


Figure 15: The field confinement for an edge-emitting laser and a vertical emitting laser.

lateral confinement for the current due to the implanted area, which is effectively an insulator. The electrical contact area can be larger than that of a etched mesa structure, which helps to lower the contact resistance. However, in order to reduce the shunt current, the implant must be deep inside the structure. Once the implant penetrates the active region, carrier life time at the edge of the implant will be dramatically reduced, which causes large carrier loss. Another shortcoming for this structure is weak index guiding. A thermal lensing effect can be used to provide optical index guiding which is fine in the continuous wave operation mode, but is problematic in the high-speed modulation mode [19]. Fig. 16(c) is the so-called dielectric-apertured structure [18], which utilizes an oxidized high-aluminum-content film (AlGaAs) as the aperture. The oxide aperture is grown next to the active medium (GaAs) and effectively prevents the shunt current between contacts. On the other hand, it will not damage the active medium and preserves the carrier lifetime. The oxide aperture is located at the antinode of the electric-field standing wave in order to have a tight current aperture without affecting the optical mode. For the purpose of waveguide effects, another oxide aperture can be grown inside the structure to control the transverse modes of lasers. From the manufacturing technique point of view, the electric contact can be easily grown between top and bottom DBRs, which not only eliminates voltage drop across the mirrors but also improves the high speed modulation performance of the device with low current.

This structure is also convenient to make both top and bottom emitting lasers. The best lateral confinement for all current, carrier and photons is given by the buried-heterostructure type of VCSEL [18] shown in Fig 16(d). The idea is to surround the pillar structure with lower refractive index and higher band gap material. However, it is hard to grow this kind of materials over high aluminum content layers. One of the methods to grow a buried heterostructure is to use impurity-induced disorder without the need of regrowth onto the high-aluminum-content layers [3].

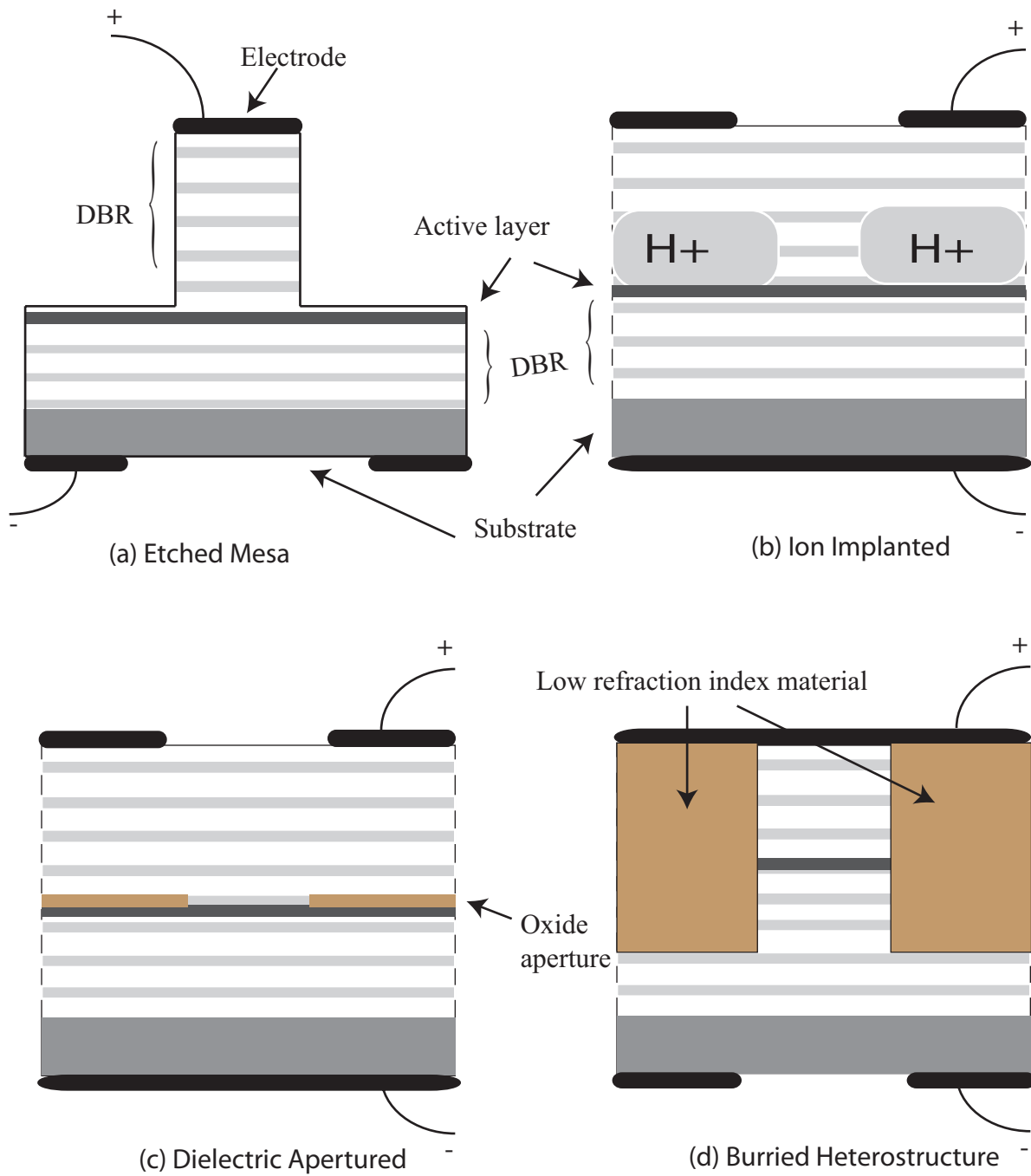


Figure 16: The schematics of different VCSEL structures [3].

2.0 EXPERIMENTAL SETUP

The main technique used for our experiments is ultrafast laser spectroscopy[20]. To study the quantum dots, a high resolution optical confocal microscope setup has been used to accurately address individual quantum dots. At the same time, the transverse-mode distribution of VCSELs and microdisk lasers are on the micron scale, and also benefit from high spatial resolution. Two different approaches have used in the time-resolved experiments: a pump-probe up-conversion technique and a streak camera system.

2.1 OPTICAL SPECTROSCOPY

Optical spectroscopy is a powerful tool to reveal the electronic structure of atoms and molecules or the band structure of semiconductor materials. By measuring the spectrum, we can extract electron energy levels from wavelength information. From Fermi's golden rule, the photon emission intensity is related to the rate of transition between two states. The linewidth also gives the lifetime information about the excited states. Emission and absorption spectroscopy, photoluminescence excitation spectroscopy, Raman spectroscopy and more, all of these spectroscopic techniques focus on frequency domain information. If we want to know the dynamics of a system, time-resolved spectroscopy will be the choice. For example, time-resolved optical gain spectroscopy of semiconductor lasers gives us more information of how well the laser will perform under high-speed modulation. Time-resolved Faraday rotation of a quantum dot system measures the electron spin precession time under external magnetic field.

Generally, the optical spectroscopic setup consists of three main parts: light source,

sample and detector system. Low divergence, monochromaticity and high intensity make a laser source the most important light source for optical spectroscopy. Another advantage of a laser source is the coherence. Using the quantum interference to control dynamic processes of a physical system, known as coherent control, is a unique method in the quantum world. Depending on desired physical parameters and experiment method, detectors can vary from photodiode, CCD camera to current meter etc.

2.2 TI:SAPPHIRE LASERS

Since all the experiments performed in this work are time-resolved spectroscopy, the ultrafast laser source is my primary tool here. To make the full use of the ultrafast laser, the fundamental knowledge of ultrafast lasers has to be understood. In order to tailor the laser to meet the requirements for many specific experiments, I constructed a mode-locked Ti:Sapphire to produce pulses with width of less than 20 femtoseconds at repetition rate of 76 MHz. This laser can also be wavelength tunable. The fastest electrical pulse is on the order of picoseconds, which is still several orders of magnitude slower than an ultrafast laser pulse. Many interesting optical effects are nonlinear effects which require high optical intensity. A Ti:Sapphire laser oscillator can produce about 10 MW peak power with average power of 1 W and 100 MHz repetition rate.

2.2.1 Why Ti:Sapphire crystal?

The Ti:Sapphire oscillator is the most popular ultrafast laser source on the earth. Why is the Ti:Sapphire crystal superior to other gain media? From the Heisenberg uncertainty principle, we know that $\Delta t \Delta \omega \geq 1/2$. To produce shorter pulse width, the bandwidth of the pulse must be bigger. The emission spectrum of a titanium-doped sapphire crystal covers from 650 nm to 1000 nm, as shown in Fig. 17(b), which is good enough for a 10 fs pulse generation. Due to this broadband spectrum, Ti:Sapphire lasers also are widely used for tunable laser light. Compared to other broadband materials, the thermal conductivity of

Ti:Sapphire crystal is 28 W/(m·K), which is crucial for high power operation. For long-term stable operation, Ti:Sapphire benefits from its excellent chemical inertness and mechanical stability.

In the ideal discrete energy case, a four-level energy system is the most efficient lasing system. In the Ti:Sapphire gain medium, the energy levels of the ion Ti^{3+} play the important role here. There is one electron on the 3d shell of the Ti^{3+} ion. When the Ti^{3+} ion replaces Al^{3+} , the 3d shell of Ti^{3+} is under an octahedral field. The 3d level will split into a twofold degenerate ${}^2\text{E}$ level and a threefold degenerate ${}^2\text{T}$ level [21]. Due to the lattice distortion from the Ti^{3+} doping, spin-orbit coupling and the Jahn-Teller effect, the ${}^2\text{E}$ will split into two levels, as shown in Fig. 18(b). The ${}^2\text{E}$ states work as the excited state and the ${}^2\text{T}$ states are ground states of the lasing ion system. Since ${}^2\text{E}$ are the only excited levels, the excited state absorption effect is very small. At the same time, the electronic states (${}^2\text{E}$ and ${}^2\text{T}$) also couple to the lattice vibrations which broaden the states. The absorption transition from ${}^2\text{T}$ to ${}^2\text{E}$ is around 400 nm to 600 nm and the radiation transition (${}^2\text{E} \rightarrow {}^2\text{T}$) is around 600 nm to 1000 nm [4]. Therefore, The Ti:Sapphire can achieve a figure of merit (the ratio of absorption at pump wavelength to absorption at lasing emission wavelength) of 300. This 2E and 2T energy level system works similar to the four level system in the discrete energy case, which is a key success for the Ti:Sapphire crystal as broadband gain medium.

2.2.2 Producing ultrafast pulses

2.2.2.1 Q-switching

The first ultrafast laser pulse was demonstrated using a ruby laser in 1962 by F.J. McClung and R.W. Hellwarth [22]. The pulsed ruby laser is based on the so-called Q-switching method which was first proposed in 1958 by Gordon Gould [23], who was also the first person using the term “laser”. The laser consisted of a ruby rod gain medium and a Kerr cell which actively controlled the Q-factor of the laser. The Q-factor, or quality factor, of a laser cavity is the ratio of the energy stored in the cavity to the dissipated per cycle. Fig. 19 shows the operation principle of the Q-switched laser. Initially, the Q-factor is low, or the loss of the resonator is high. Since the loss is high, simulated emission can not work. The optical pump continues building up the population inversion.

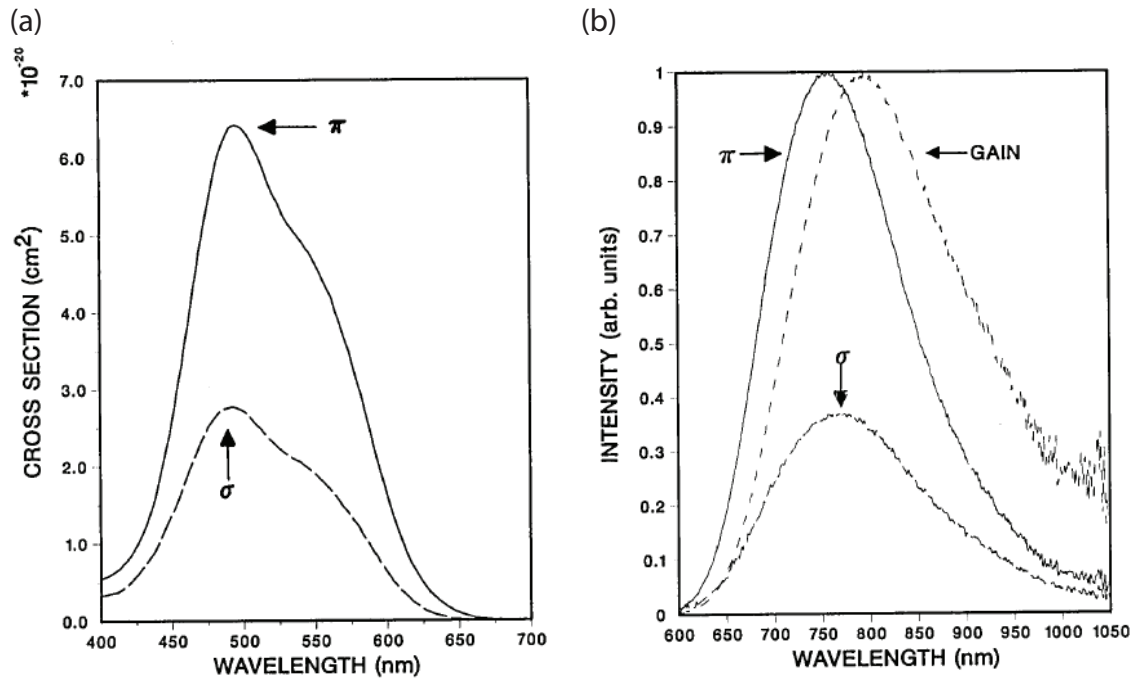


Figure 17: (a) The absorption cross sections and (b) the fluorescence spectra of a Ti:Sapphire crystal for different polarization. The images are taken from [4]

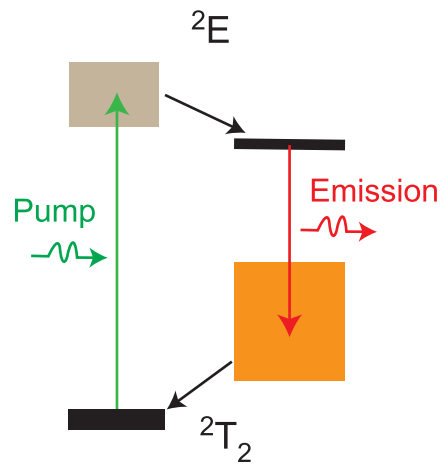


Figure 18: The schematics of Ti:Sapphire energy level 2T_2 and 2E transition.

During this time, spontaneous emission and other non-radiative decay mechanism are major losses of the resonator. When the gain reaches the maximum or gain saturates, the Q-switch increases the Q-factor for a short period of time. The stimulated emission will be triggered and releases the stored energy during a short time window. A short pulse of laser emission is generated. There are two types of Q-switched laser: one is an active Q-switch and the other is a passive Q-switch. An active Q-switched laser usually uses a Kerr cell which deflects the light emission and prevents optical feedback from triggering stimulated emission. By applying a periodic electrical signal to a Kerr cell, the lasing emission can be switched on and off in a precisely controlled manner. One obvious disadvantage is that the pulse repetition rate is slow since it is limited by the speed of electrical response of the Kerr cell. In the passive Q-switched laser, the Q-switch is a saturable absorber which absorbs laser emission and becomes transparent for laser emission when the inverted carriers reach a certain limit. When the absorber saturates, stimulated emission becomes efficient and depletes the carriers for short pulse emission. After the pulse, the absorber starts to absorb more light and the cavity turns into high loss state. Compared to an active Q-switched laser, the repetition rate of a passive Q-switched laser can not be directly controlled. However, a passive Q-switched laser usually produce shorter pulses than an active Q-switched laser.

2.2.2.2 Mode-locking Q-switched lasers produce laser pulse durations on the order of a few nanoseconds. The breakthrough of ultrafast laser pulse generation came with the invention of the colliding-pulse mode-locked dye laser which generate sub-100 fs laser pulse [24]. In the 1990s, the birth of the Kerr-lens mode-locked Ti:Sapphire laser [25, 26] made the ultrafast laser source commercially widely available. Its superior stability and high power intensity make the Ti:Sapphire laser the scientist’s favorite ultrafast laser source. Stabilized Ti:Sapphire oscillators are being used in precision optical frequency metrology.

Fig. 20 shows the basic idea of mode-locking. If all the laser modes have a well-defined phase relation to each other, the quantum interference of all the modes will produce a sharp pulse at a well-defined repetition rate. To have a mode-locked laser, the primary requirement is lasing modes with equidistant frequency difference. A laser cavity naturally defines the longitudinal axis modes with frequency difference of $1/\Delta t$ (where Δt is the roundtrip time

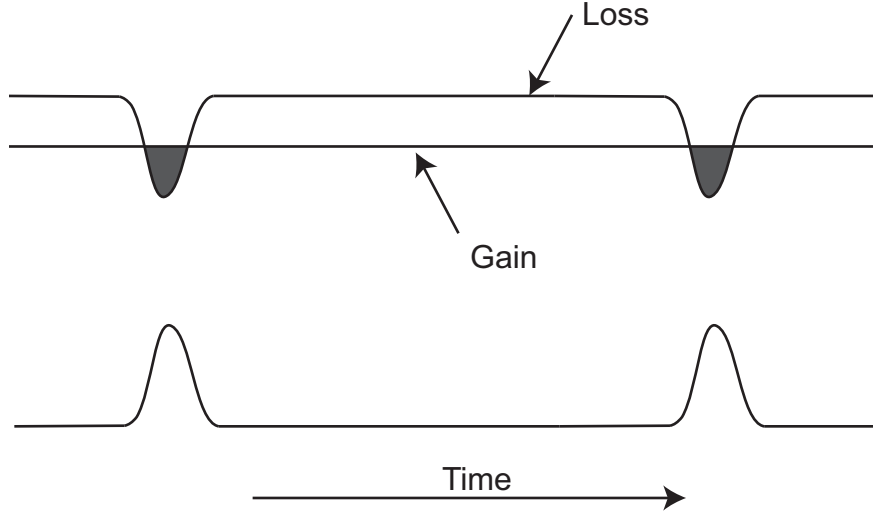


Figure 19: The operation principle of the Q-switched laser. A periodic modulation of the cavity loss will produce pulsed emission when gain > loss.

of the cavity). If there are N modes locked in phase, the resulting pulse width $\tau = \Delta t/N$. For a 10 fs mode-locked laser with a repetition rate of 100 MHz, there should be 1,000,000 modes locked in phase. However, a well-defined frequency alone is not good enough for stable operation. Broadband optics and gain medium are required which defines how short the laser pulse can be. The emission spectrum of Ti:Sapphire, which is over 400 nm wide, is well suited to this application. As the ultrafast short pulse travels through any medium, it will inevitably have dispersion. The dispersion is caused by different refraction index for different wavelength. It essentially adds phase difference for different laser modes which can break the mode-locking. Therefore, a proper dispersion control mechanism is needed for stable mode-locked laser oscillator.

Another key element for stable mode-locking operation is the modulation. There are two kinds of modulation: one is active modulation and the other is passive modulation. Active mode-locking usually uses an external synchronous source to drive a modulator to realize loss modulation or gain modulation. Intrinsically, the speed of the external electronic source limits the performance of the active mode-locking laser to produce ultrashort pulses.

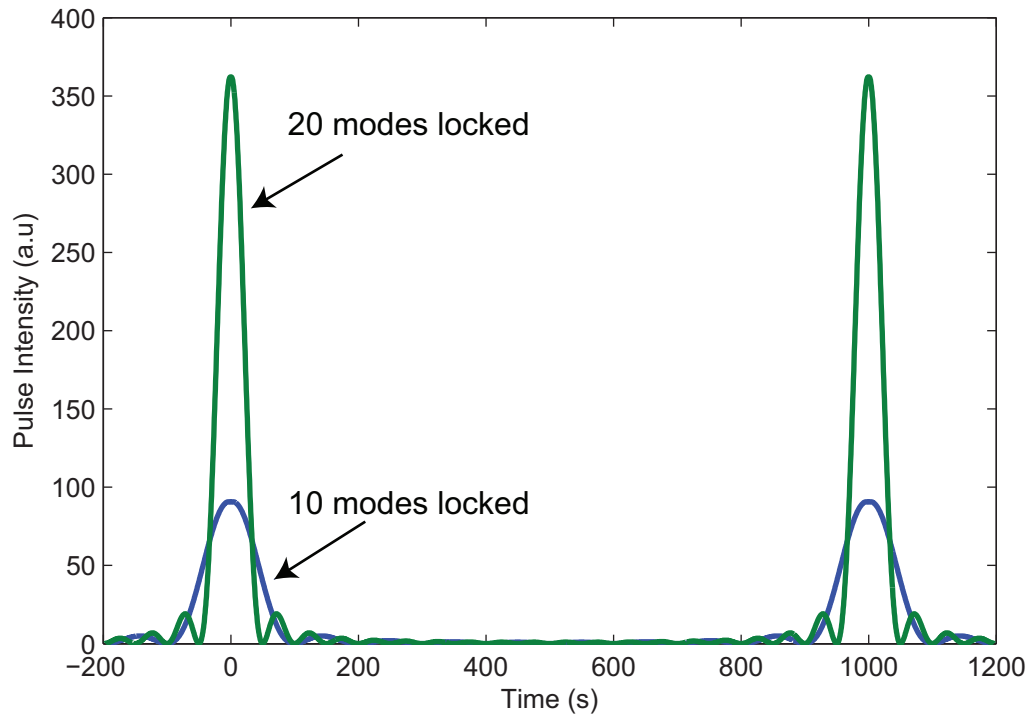


Figure 20: The basic idea of mode-locking. The blue curve shows a pulse with 10 modes locked and the green curve shows a pulse with 20 modes locked. The pulse width of the green curve is half of that of the blue curve.

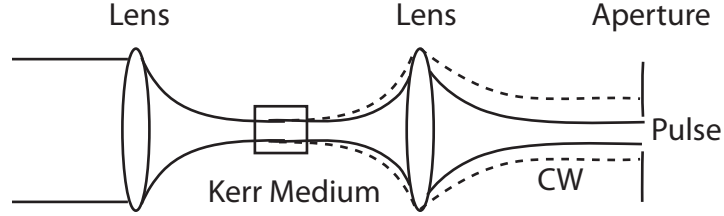


Figure 21: The Kerr lensing effect in the gain medium. The pulsed emission is focused much tighter than the CW emission.

Furthermore, for stable mode-locking operation, the active modulation frequency has to precisely match the repetition frequency of the optical cavity on the order of 1 ppm (part per million) [27]. By contrast, a passive mode-locking mechanism can suppress these problems and can generate much shorter pulses than active mode-locking lasers.

A Ti:Sapphire laser oscillator usually works as a passive mode-locking laser. In particular, it is a so-called Kerr-lens mode-locked laser. In this type of laser cavity, the gain medium Ti:Sapphire crystal has multiple functions which provide gain, self-amplitude modulation, self-phase modulation etc. As discussed before, a Ti:Sapphire crystal has an emission spectrum which is over 400 nm wide, which makes it a ideal broadband gain medium. The nonlinear refraction index of a Ti:Sapphire crystal is another important feature which gives rise to the so-called Kerr-effect. The refractive index can be written as

$$n(t) = n_0 + n_2 I(t), \quad (2.1)$$

where n_2 is known as nonlinear refractive index coefficient, and $I(t)$ is the pulse intensity. Eq. (2.1) shows that the refractive index changes with instantaneous pulse intensity profile, an effect known as the optical Kerr-effect [28]. When $n_2 > 0$, the refractive index is larger for higher laser intensity. For a Gaussian beam profile, the refractive index at the center of the laser beam will be larger than that at the side of the laser beam. Effectively, the Ti:Sapphire crystal becomes a lens known as Kerr-lens. By passing through the Kerr medium, high power laser pulses will experience tighter focus than the CW emission. When an aperture is incorporated inside the cavity, the CW emission will have greater loss than the pulse emission,

as shown in Fig. 21. The Kerr-lens also shapes the temporal profile of the laser pulse by imposing more loss on the leading and trailing part of the laser pulses, a process known as self-amplitude modulation. In other words, the Kerr-lens functions as an equivalent saturable absorber. To be specific, the Kerr-lens is a fast saturable absorber whose response time is on the order of $1 \sim 2$ femtoseconds [29] which is ideal to produce a few-cycle ultrafast laser pulses. By contrast, the mode-locked dye laser uses organic dyes as a saturable absorber. They generate saturable absorption by saturating the carrier population of excited states. Therefore, the response time depends on how fast carriers relax back to ground states. For organic dyes, the relaxation time is on the order of picoseconds. To produce shorter pulse than the response time of saturable absorber, this type of ‘slow’ saturable absorber needs to work with dynamic gain saturation to shape the leading and trailing part of pulse. Since the resonant optically excited excitation is needed to saturate the absorption, this process inevitably adds another bandwidth filtering effect which intrinsically limits how short the laser pulse can be. On the other hand, the Kerr-lens mode-locked Ti:Sapphire laser takes advantage of the Kerr nonlinearity, which is a nonresonant effect, and can make full use of Ti:Sapphire crystal’s broad bandwidth. Fig. 22 shows the fundamental mechanism for a slow saturable absorber and a fast saturable absorber.

Besides the self-amplitude modulation, the nonlinear refractive index of a Kerr medium can alter the instantaneous pulse phase. The phase change caused by the Kerr effect is:

$$\Delta\phi = -\frac{2\pi}{\lambda}L\Delta n_2 I(t), \quad (2.2)$$

where λ is the wavelength, $I(t)$ is the pulse intensity and L is the length of the Kerr medium. If we take the first derivative of Eq. (2.2) over the time, we can write the frequency change:

$$\Delta\omega = \frac{2\pi}{\lambda}Ln_2 \frac{dI(t)}{dt}. \quad (2.3)$$

When $I(t) = A \exp(-(t/\tau)^2)$, a Gaussian pulse, then:

$$\Delta\omega = \frac{2\pi}{\lambda}Ln_2 A \frac{2t}{\tau^2} \exp(-(\frac{t}{\tau})^2). \quad (2.4)$$

As plotted in Fig. 23, the self-phase modulation by the Kerr effect gives a red shift in frequency for the leading part of the pulse and blue shift for trailing part of the pulse. As a

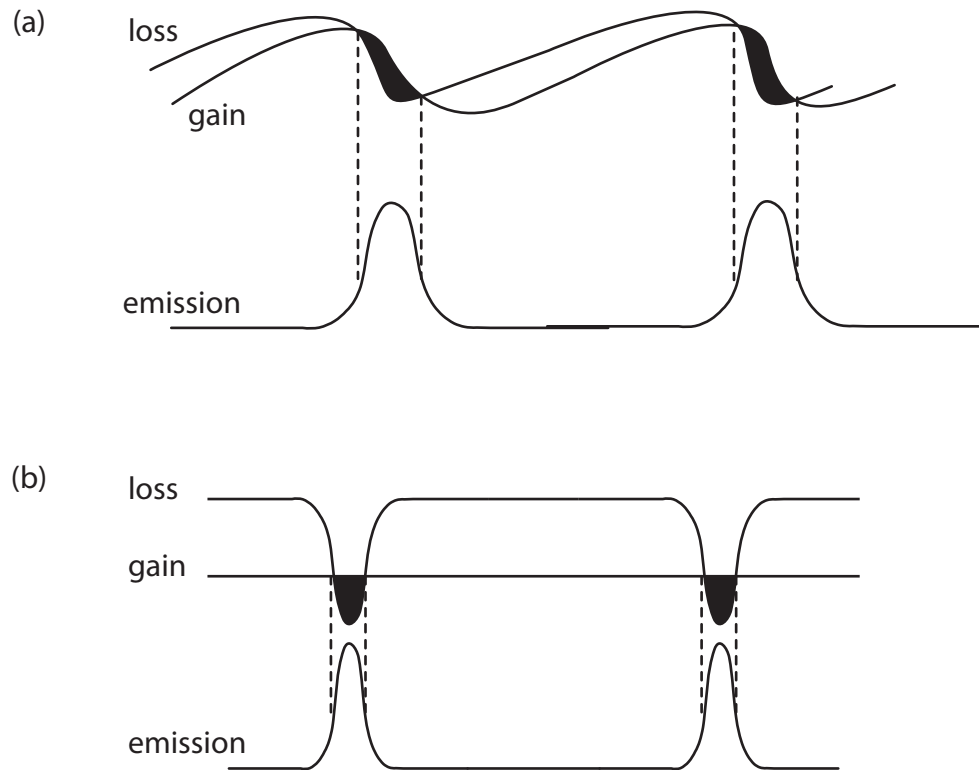


Figure 22: The principle for (a) a slow saturable absorber, where the slow loss modulation alone can only shorten the leading edge of a pulse and a dynamic gain modulation cut off the trailing edge of a pulse; (b) a fast saturable absorber, where the gain relaxation is slow and treated as a constant, and the fast loss modulation can produce the pulse alone. [5]

consequence of the self-phase modulation, the available bandwidth of a Ti:Sapphire crystal is further broadened to produce shorter laser pulses.

2.2.3 Dispersion compensation

As the laser pulse circulates inside the cavity, it will pass through air, the Ti:Sapphire crystal and other optical components. The dispersion of the material will change the spectral phase of the laser pulse. The phase change is defined as

$$\phi(\omega) = k(\omega)z, \quad (2.5)$$

where the ω is the frequency, k is the wavevector and z is the length of the medium. Taking the first derivative of Eq. (2.5), we get

$$\frac{d\phi}{d\omega} = \frac{dk}{d\omega}z = \frac{z}{v_g}, \quad (2.6)$$

where $v_g = d\omega/dk$ is the group velocity. Eq. (2.6) is usually called group delay (GD), which measures the delay of the wave packet. Another important measure is the second order derivative of phase (2.7), known as group delay dispersion (GDD):

$$\frac{d^2\phi}{d\omega^2} = \frac{d^2k}{d\omega^2}z = \frac{z}{c}\left(n + \omega \frac{dn}{d\omega}\right). \quad (2.7)$$

GDD tells us the dispersion between different groups of the wave packet with different wavelengths. If $GDD \neq 0$, the laser pulse will be broadened and degrade eventually. Usually, the refractive index of normal material decreases with increasing wavelength, which makes the longer wavelength part of the laser pulse faster than shorter wavelength part, as shown in Fig. 24. In order to maintain a stable pulse generation, a proper dispersion control is required for a Ti:Sapphire laser oscillator. Since the normal dispersion is positive, we need to create negative dispersion to compensate.

One popular solution is angular dispersion, given by [30]

$$\frac{d^2\phi}{d\omega^2} \approx -\frac{L}{c}\omega\left(\frac{d\theta}{d\omega}\right)^2, \quad (2.8)$$

where L is the travel distance of pulse after bending and θ is the angle change. From Eq. (2.8), we know the angular dispersion is always negative. Prisms and gratings are common

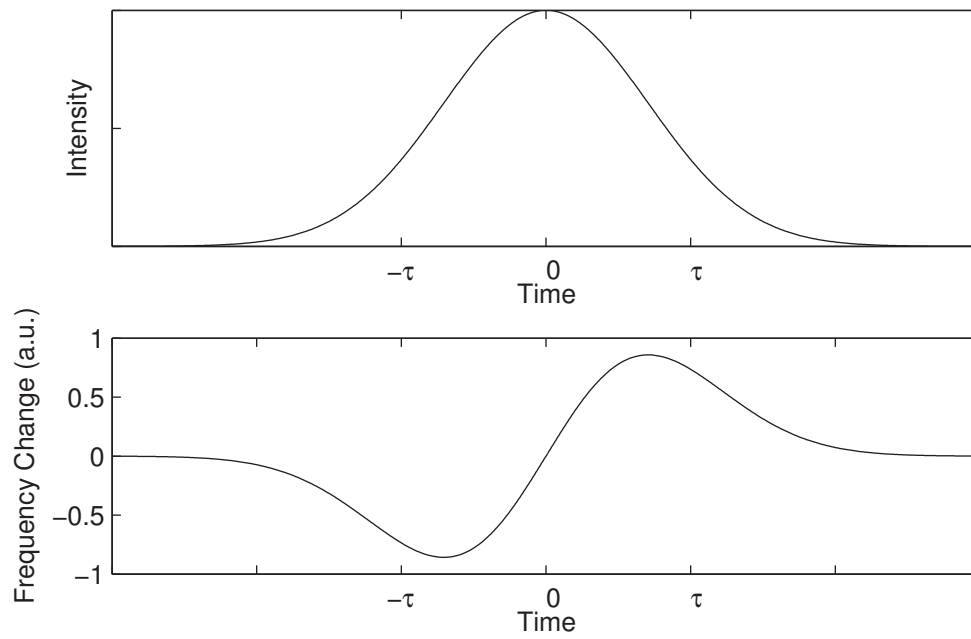


Figure 23: The self-phase modulation effect when a Gaussian pulse passes through a Kerr medium. (a) The intensity profile associated with a Gaussian pulse; (b) the nonlinear refractive-index-induced frequency change with the time for the Gaussian pulse.

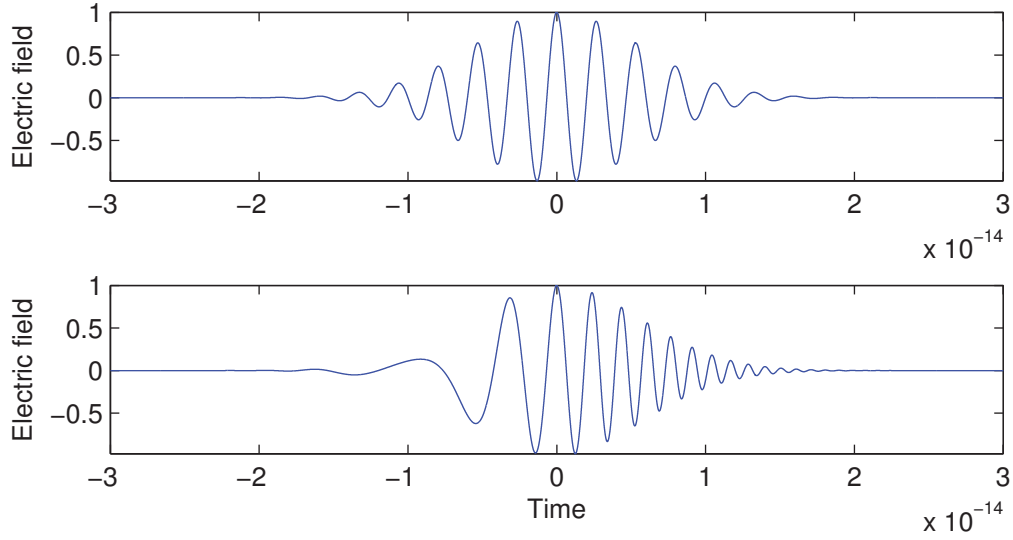


Figure 24: The electric field of a Gaussian pulse with (a) no dispersion (b) positive dispersion.

optical components to produce the angular dispersion. However, as shown in Ref. [30], a single prism cannot provide negative dispersion in a laser cavity. Therefore, a prism pair is used to compensate positive dispersion. In practice, four prisms or two prisms with a folding mirror are commonly used to avoid spatial dispersion, as shown in Fig. 25.

In the generation of a few femtosecond laser pulse, it is crucial to compensate not only second order dispersion but also higher order dispersion [31]. Prism pairs can not compensate higher order dispersion too well. Another approach for negative dispersion is called a chirped mirror. The chirped mirror was first invented by Szipöks et al. [32]. These are stacks of alternating dielectric films with high refractive index (n_H) and low refractive index (n_L). Unlike a Bragg reflector with fixed thickness ($\lambda/4$) for each layer, a chirped mirror has a series of dielectric films with slowly varying thickness. By knowing the precise refractive index of each thin film, arbitrarily high reflectivity can be designed for a chirped mirror if there is no limit to the number of deposit layers. At the same time, the penetration depth of higher frequency waves is shorter than that of lower frequency waves. In other words, negative dispersion is imposed by reflecting the laser pulse from a chirped mirror. The basic

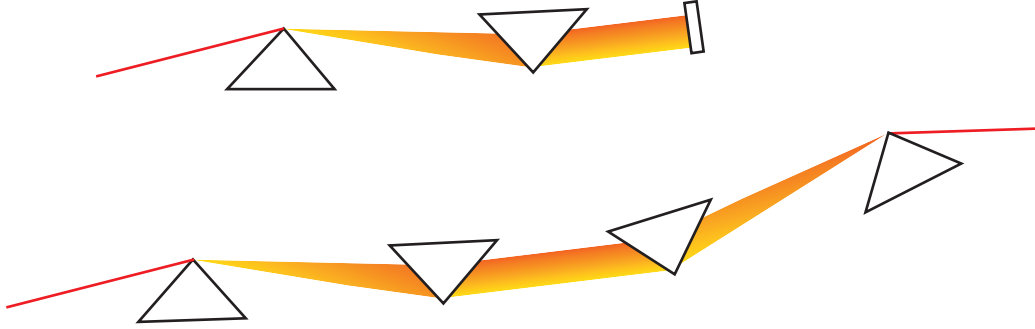


Figure 25: A prism pair with a folding mirror or four prisms setup for dispersion compensation. The first prism disperses the input beam and the second prism collimates the beam.

idea of a chirped mirror is shown in Fig. 26. Compared with a prism pair, a chirped mirror has much higher reflectivity over a very broad wavelength range and much less insertion loss. By carefully designing the chirped mirror, higher order dispersion can be compensated for specific application requirements. Since a chirped mirror is a type of interferometric structure which contains a partial reflector and a high reflector, the group delay will have Gires-Tournois-like oscillation [33]. To make a smoother dispersion compensation, chirped mirrors usually are used in pairs, so that one of the chirped mirror has an extra $\lambda/4$ phase shift in order to cancel out the oscillation effect. Over time, chirped mirror performance has been improved with many new designs, such as a double-chirped mirror [34] and a back-side-coated chirped mirror [35] etc.

2.2.4 Ti:Sapphire laser oscillator design

Fig. 27 is a schematic setup of a Kerr-lens mode-locked laser oscillator which includes a Kerr medium, an end mirror, two lenses and an output coupler. In order to provide stable optical feedback, a laser cavity needs to be able to trap radiation inside the cavity. A simple cavity design method is called the ABCD matrix formalism which can predict the beam focus and characteristics [36]. In Fig. 27, the focal length of lens is f , the distance between the lenses

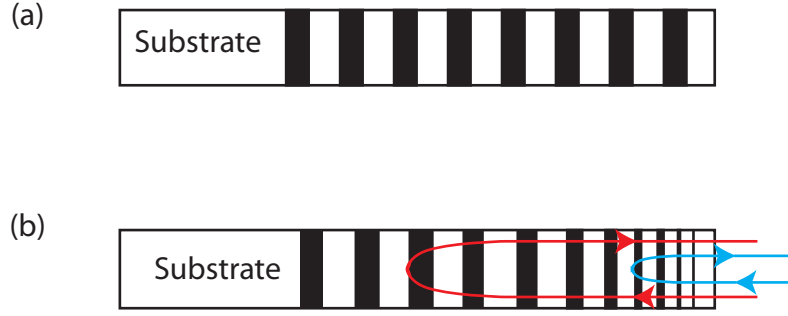


Figure 26: A schematic of (a) a Bragg reflector (b) a simple chirped mirror.

is $L_0 = 2f + \delta$, one arm length is L_1 and the other is L_2 . For convenience, the cavity in Fig. 27 is equivalent to a simple two-mirror cavity [37] as shown in Fig. 28, where

$$\begin{aligned}
 R_1 &= -\frac{f^2}{L_1 - f} \\
 R_2 &= -\frac{f^2}{L_2 - f} \\
 L &= R_1 + R_2 + \delta.
 \end{aligned} \tag{2.9}$$

Following the beam path for a round trip, we can get the transfer matrix:

$$\begin{aligned}
 M &= \begin{bmatrix} A & B \\ C & D \end{bmatrix} \\
 &= \begin{bmatrix} 1 & L \\ 0 & 1 \end{bmatrix} \begin{bmatrix} 1 & 0 \\ \frac{2}{R_2} & 1 \end{bmatrix} \begin{bmatrix} 1 & L \\ 0 & 1 \end{bmatrix} \begin{bmatrix} 1 & 0 \\ \frac{2}{R_1} & 1 \end{bmatrix} \\
 &= \begin{bmatrix} 1 + \frac{2L}{R_2} + \frac{4L}{R_1} + \frac{4L^2}{R_1 R_2} & \frac{2L(R_2 + L)}{R_2} \\ \frac{2(2L + R_1 + R_2)}{R_1 + R_2} & 1 + \frac{2L}{R_2} \end{bmatrix}
 \end{aligned} \tag{2.10}$$

From the ABCD matrix law, the following relation has to be satisfied if a cavity is stable:

$$\left| \frac{A + D}{2(AD - BC)} \right| \leq 1 \Rightarrow 0 \leq \left(1 + \frac{L}{R_1}\right) \left(1 + \frac{L}{R_2}\right) \leq 1. \tag{2.11}$$

Substituting Eq. (2.9) into Eq. (2.11), we get $0 \leq \delta \leq -R_1$ or $-R_2 \leq \delta \leq -(R_1 + R_2)$. The oscillator will have stable CW emission within these two ranges. If $R_1 \neq R_2$ or $L_1 \neq L_2$, there will be a gap between two stable zones.

So far, the dispersion and Kerr effect have not been included in the above analysis. More comprehensive treatments are the ‘‘Theory of mode locking with a fast saturable absorber,’’ proposed by Haus et al. [38] and ‘‘Pulse formation is dominated by the interplay between self-phase modulation and negative dispersion,’’ by Brabec et al. [25, 39]. From these previous studies, it is known that a stable pulsed emission needs efficient modulation processes such as self-amplitude modulation (SAM) and self-phase modulation (SPM). However, SPM induced by the Kerr-effect also adds a positive chirp to the pulse, which will degrade spatial soliton formation. Negative dispersive components such prism pairs or chirped mirrors can compensate this negative effect from SPM.

Another parameter to measure the cavity is the asymmetric parameter [39]:

$$\gamma = \frac{R_2}{R_1} = \frac{L_1 - f}{L_2 - f}. \quad (2.12)$$

Assuming $\gamma \geq 1$ or $L_1 \geq L_2$, the gap between the two stable zones becomes larger with increasing γ . In order to favor soliton pulse formation, γ must be greater than 1, and the effective modulation index has to be greater than 0 [39]. From these analytical calculations, it turns out the effective modulation is more efficient near the edge of the stable zones. Therefore, there will be a trade-off between modulation and stability. γ around 2 has been found is a good balance between modulation efficiency and cavity stability. By taking account for SAM, SPM and GDD, the FWHM (full width half maximum) of the pulse duration is given by [40],

$$\tau = \frac{3.53|D|}{\phi W} + \alpha\phi W \quad (2.13)$$

where D is the round-trip GDD, ϕ is the Kerr nonlinearity, W is the pulse energy and α is a coefficient that depends on the position of the pulse inside the cavity.

Fig. 29 shows one of our laser cavity configurations. This oscillator is an X-shape configuration with three pairs of negative dispersive mirrors (M1 to M6). These chirped mirrors have 99.9% reflectivity over the 650 nm to 1020 nm range and $-50 \pm 20 fs^2$ negative dispersion per bounce. The folding mirrors M1 and M5 have a radius of curvature of 75 mm

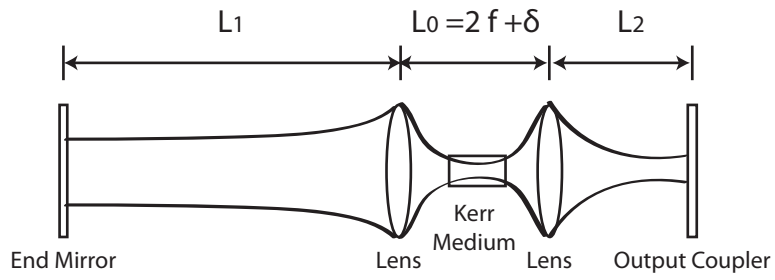


Figure 27: The simple schematic of Ti:Sapphire laser oscillator.

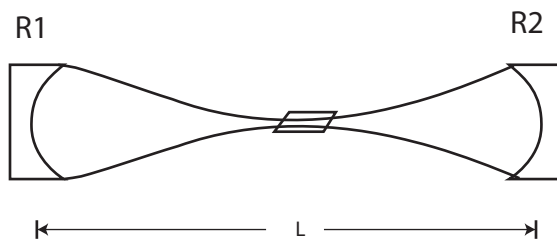


Figure 28: The equivalent two mirror cavity for Fig. 27.

for the front surface and are coated with antireflection film on the front and back surfaces, which has less than 5% reflectivity for 490 nm to 540 nm. The pump source is a frequency-doubled diode-pumped solid state Nd:YAG CW laser emitting at 532 nm. The total cavity length is designed for 76 MHz repetition rate. The transmission rate of the output coupler is about 15% for 600 nm to 1200 nm, which is measured with another commercial Ti:Sapphire oscillator. The cavity is asymmetric and the value of γ is 2 to intensify the pulse modulation.

As mentioned before, the Kerr-effect and a hard aperture near one of the cavity ends create an equivalent saturable absorber. Here, we do not have a hard aperture inside. Instead, we use a concept of “soft-aperture”. The CW pump beam is tightly focused onto the Ti:Sapphire crystal which gives a spatial varying gain profile. At the same time, Kerr-effects produce an ultrafast self-focusing for pulsed emission. Depending on how the emission overlaps with the gain profile, tighter focused pulse emission will experience larger gain than CW emission. In another word, the beam waist of the focused pump beam works as a aperture inside the cavity.

A Brewster-cut Ti:Sapphire crystal, which is often called a Brewster cell, is the gain medium. The thickness of the crystal is 4 mm and the absorbance is 5 cm^{-1} for a 532 nm pump laser, which gives about 80% absorption of pump power. The Brewster cut reduces the reflection loss for p-polarized emission but also adds astigmatism on the beam [41] when the Brewster cell is located at the focal point. The astigmatic distortion degrades the performance of the internal focusing. At the same time, tight focusing is preferred for large Kerr nonlinearity. Fortunately, as Ref. [41] pointed out, the astigmatism caused by the Brewster-cut crystal can be compensated by tilting the folding mirrors (M1 and M2) at a certain angle. The folding angle θ , as shown in Fig. 29, is given by [41]:

$$\sin(\theta) \tan(\theta) = \frac{2t(n^2 - 1)\sqrt{n^2 + 1}}{n^4 R}, \quad (2.14)$$

where t is the thickness of the Ti:Sapphire crystal, n is the refractive index of the crystal and R is the radius of curvature of the folding mirror. For example, in our cavity, with $t = 4$ mm, $n = 1.75$ and $R = 75$ mm, we can get $\theta = 17.5^\circ$.

Chirped mirrors can only compensate a fixed amount of dispersion without any fine tuning. To minimize the pulsed width, the total GDD should be a little below 0 [39]. In

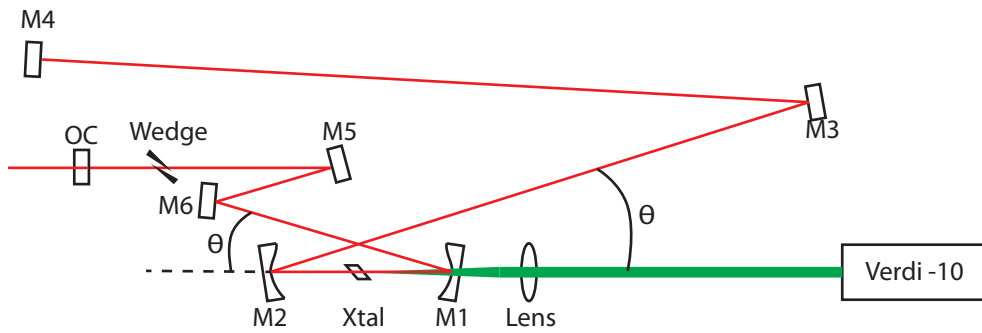


Figure 29: The schematic setup of Ti:Sapphire oscillator with chirped-mirror-only design.

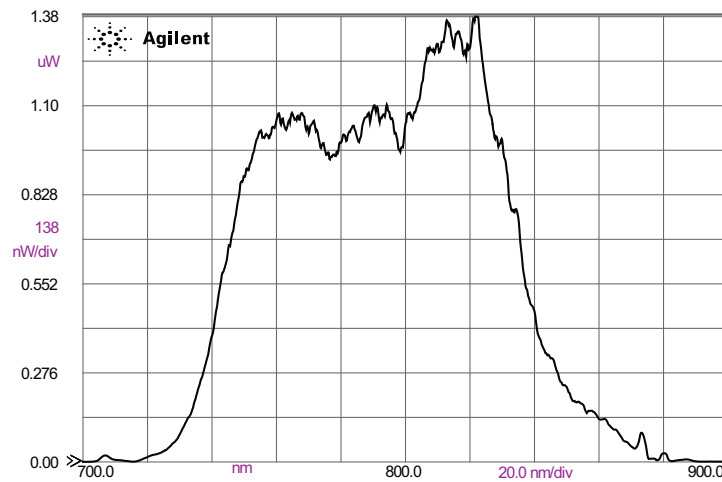


Figure 30: A typical spectrum measurement for a pulse with a FWHM on the order of 10 fs (a typical pulse width measurement as shown in Fig. 40) from chirped mirror based cavity.

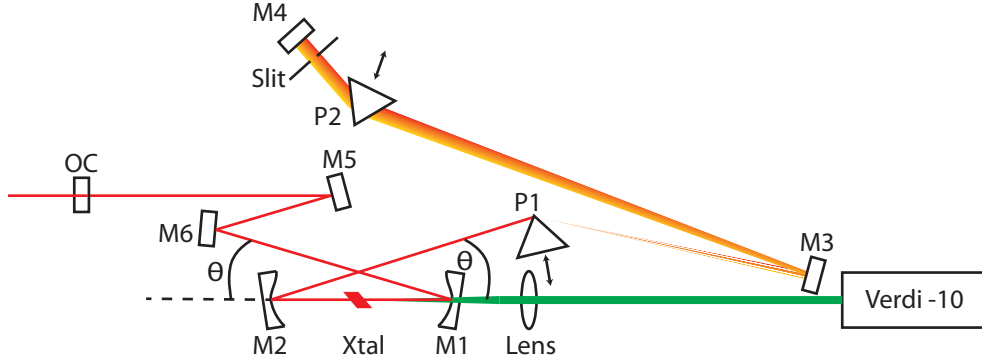


Figure 31: The schematic setup of tunable Ti:Sapphire oscillator with prism-pair design.

order to fine tune the dispersion, a pair of fused silica wedges is placed inside the cavity. The wedge has an apex angle of 11° and the minimum thickness is about 1 mm. With this cavity, we were able to generate a laser pulse with a bandwidth of 100 nm (FWHM), as shown in Fig. 30 and a typical pulse width measurement is shown in Fig. 40.

A Kerr-lens mode-locked laser based on chirped mirrors can be very compact and easy to align. It is an ideal choice if you just want to produce the shortest pulse possible. However, in some applications, wavelength tuning is desired. In this application, a mode-locked laser with a prism-pair is more versatile. Fig. 31 is a schematic setup for our laser cavity which includes a pair of prisms. The prism pair is made of fused silica and has the Brewster cut for minimizing the insertion loss when aligning the laser with minimum deflection angle. With a prism pair, the dispersion can be fine tuned by moving the prisms in or out of the beam. After the laser beam passes through the prism, it will be dispersed over a range of angles depending on the individual wavelengths. A variable slit is placed at the end mirror side after two prisms. By adjusting the width of the slit, we can control the spectral range of the laser pulse. The desired center wavelength can be selected by moving the slit across the beam.

One of the shortcomings of the Kerr-lens mode-locked lasers is that the pulsed emission does not self-start [27]. However, a fast disturbance of the cavity usually starts the mode-locking. Changing the cavity length rapidly is a commonly used method for starting the

mode-locking. For example, I just tapped one of the folding mirrors (M1 and M2) for chirped-mirror-only cavity or quickly moved the prism in and out for a prism-based cavity to initialize the pulsation. When the cavity is perfectly aligned, a high frequency vibration of the optical table can start the mode-locking.

2.3 PULSE SHAPING

An ultrafast laser pulse is extremely narrow in the time domain and very broad in the frequency domain. It has been proved to be an important super-speed laser source for ultrafast optical impulses. However, a single laser pulse generated from the ultrafast laser oscillator is a little “boring” sometimes. For many applications, the demand for more control of laser pulses is critical, such as optical coherent control, high power laser amplification, and optical frequency metrology etc. Pulse shaping is a very broad topic which exists in any process to alter the pulse envelope, the phase of pulse or the power of pulse, and so on. Actually, a Kerr-lens mode-locked laser cavity itself involves many pulse shaping process such as self-amplitude modulation, self-phase modulation and dispersion control, etc.

2.3.1 Actively stabilized double pulse generation

One of the most common pulse shaping techniques is double pulse generation. Basically, a single pulse splits into two pulses with a well defined time delay between them. For some applications like optical coherent control of excitation states [42], the phase difference has to be well defined. For many challenging experiments, the signal output is weak, so a long time integration is needed. Therefore, the phase difference also needs to be maintained for a long measurement time.

Fig. 32 shows the schematic setup for a computer controlled Mach-Zehnder interferometer. The setup has two input ports, one is for a CW HeNe laser and the other is for the Ti:Sapphire laser. The two beams have different linear polarization which are perpendicular to each other, and a polarizing beamsplitter combines the two beams. At the output port,

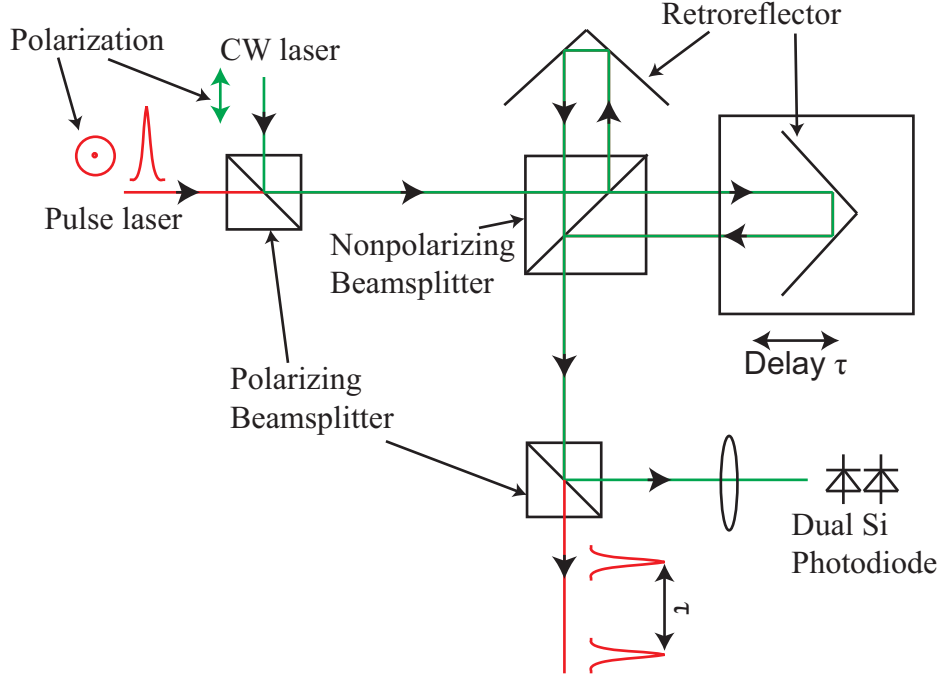


Figure 32: The computer-based stabilized double-pulse generation.

another polarizing beamsplitter directs the CW laser to a quadrant photodiode and the laser pulse to the experiment. Since the pulse laser has very short coherence length, the CW laser is used to track the path length for two beams. At the quadrant diode side, the HeNe laser produces an interference pattern which is magnified by a lens. We only use two detectors of the quadrant diode for the detection of the interference pattern. For the best result, the adjacent detectors have $\pi/2$ phase difference for the interference. To reduce the influence of ambient light, a bandpass filter for the HeNe laser is attached to the quadrant photodiode. The path difference is controlled by a speaker which is driven by a National Instruments (NI) data acquisition (DAQ) card.

As shown in Fig. 33 (a), the x and y signals are from two adjacent detectors which measure the interference of the CW HeNe lasers. The phase shift between two detectors is about 0.56π or 0.28 cycle. If we plot x versus y as in Fig. 33 (b), we will get a complete ellipse for a full interference period. Therefore, each point on the ellipse has a unique polar angle which corresponds to a phase angle within a 2π phase cycle. Before every experiment,

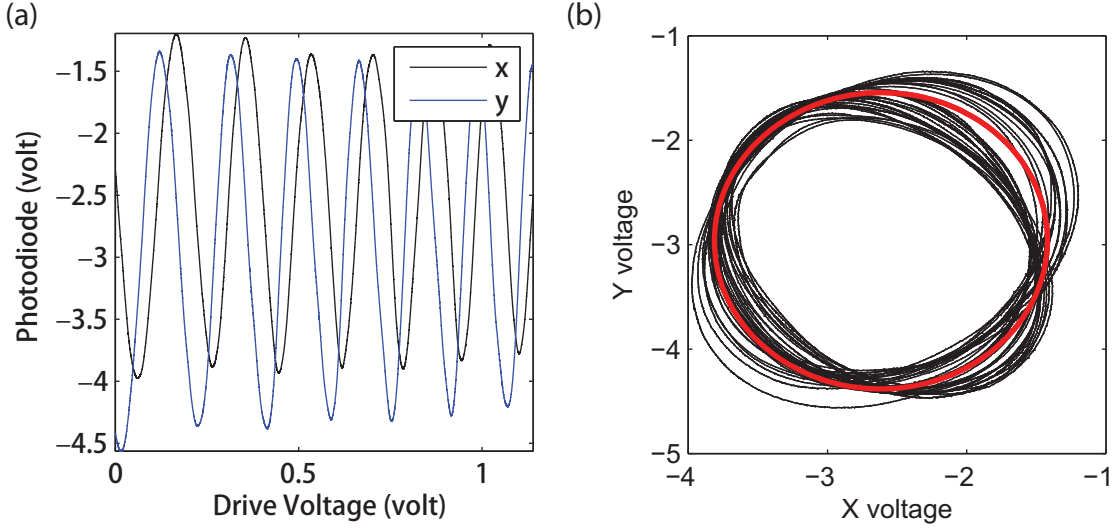


Figure 33: (a) The measured signal from the quadrant photodiode for X and Y detector. (b) The measured ellipse based-on the X and Y signals, which works as the phase reference.

the unique ellipse has to be defined first, which then works as a phase reference. Usually, we measured the full travel range of the speaker and used the Levenberg-Marquardt algorithm [43] to find the reference ellipse. The red ellipse in Fig. 33 (b) is the fitted ellipse.

A standard ellipse equation is the following:

$$\begin{cases} x = a \cos(\theta) \\ y = b \sin(\theta) \end{cases} \quad (2.15)$$

which is a simple ellipse centered at the origin, with a and b the half-axis lengths. Any other ellipse can be transformed from Eq. (2.15) by rotation and translation operations:

$$\begin{bmatrix} x' \\ y' \end{bmatrix} = T + R \cdot \begin{bmatrix} x \\ y \end{bmatrix}, \quad (2.16)$$

where

$$T = \begin{bmatrix} x_0 \\ y_0 \end{bmatrix}$$

$$R = \begin{bmatrix} \cos(\alpha) & -\sin(\alpha) \\ \sin(\alpha) & \cos(\alpha) \end{bmatrix}.$$

Basically, measured ellipses can be transformed back to a simple ellipse (Fig. 34). By scaling the x and y coordinates with the half-axis lengths, a simple ellipse can be turned into a circle which makes phase calculation even easier.

In practice, a computer-based proportional-integral-derivative (PID) loop stabilized the path difference based on the feedback from the quadrant photodiode. Since all the calculations and controls are performed by a computer, the setup is easier and more flexible than an analog PID device. A phase change bigger than 2π can also be tracked by implementing a proper algorithm, and the accumulated phase change can be calculated as long as the speed of speaker movement is slower than the PID loop rate. The Labview program we used has up to 1 kHz rate. For higher speed and more determined time control, a real-time operating system targeted PC is recommended. The PID loop rate is up to 1 MHz for the real-time Labview program.

For more critical and stable experiments, a piezo actuator works better. However, the travel range is only a few hundred micrometers. To realize long pulse delay, a stepper motor can work together with a piezo actuator which can be easily programmed. This flexible computer-based stabilized interferometer can maintain the path difference within 2% of the HeNe laser wavelength (632 nm). It gives a 0.04 fs accuracy on the time delay between two pulses.

2.3.2 Double-color double pulse generation

On the femtosecond scale, it is hard to directly modify the time profile in the time domain. The most effective way is to manipulate the amplitude and phase of pulse spectrum. Dispersion control setup based on prism pairs or grating pairs are literally pulse shapers which modify the phase information for different wavelength components. By controlling the dispersion, we can compress or stretch the pulse's time profile. This type of pulse shaper was first demonstrated for picosecond pulses [44] and then extended to the application of femtosecond pulses.

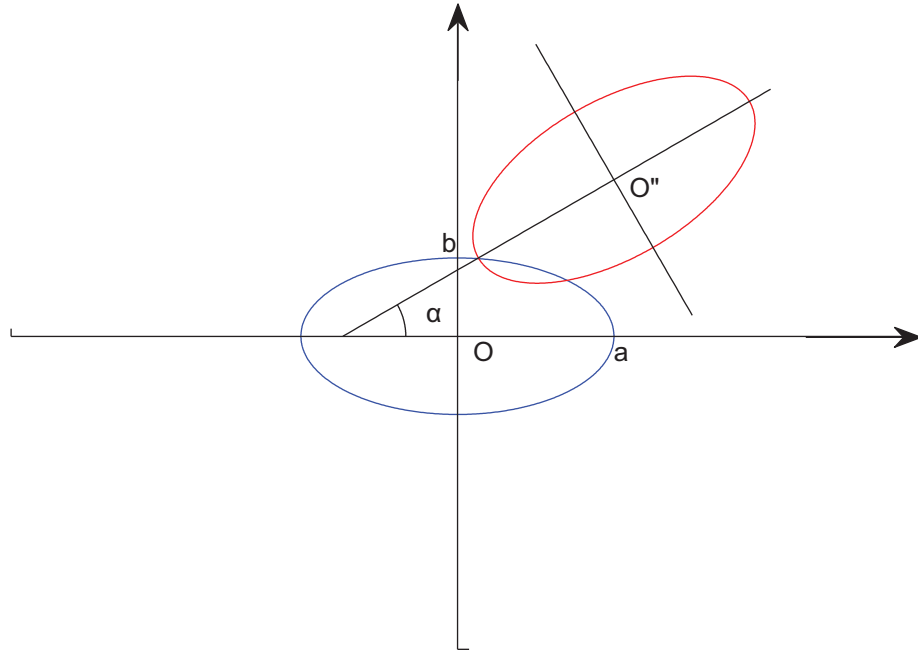


Figure 34: A measured phase-reference ellipse can be transformed into a simple ellipse.

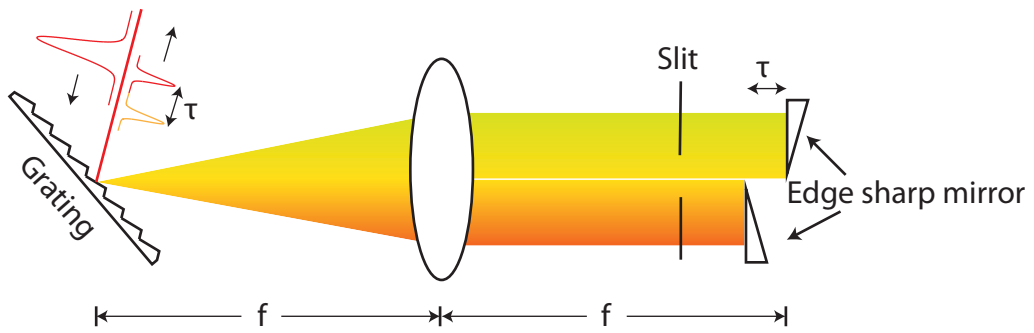


Figure 35: The schematic setup for two-color double pulse generation.

The pulse shaper consists of three main parts: the Fourier transform of the pulse, an amplitude and phase mask, and the inverse Fourier transform. The Fourier transform of the pulse is usually done by a prism or grating, which disperses the pulse in the frequency domain,

$$E(w) = \mathfrak{F}[E(t)], \quad (2.17)$$

and the function of amplitude and phase mask is,

$$M(w) = t(w)e^{-i\phi(w)}. \quad (2.18)$$

After the mask, we get,

$$E'(w) = M(w) \cdot E(w). \quad (2.19)$$

At last, by doing the inverse Fourier transform, we can get the shaped pulse,

$$E'(t) = \mathfrak{F}^{-1}[M(w)] \otimes \mathfrak{F}^{-1}[E(w)] = M(t) \otimes E(t), \quad (2.20)$$

where \otimes stands for the convolution. Fig. 35 shows a typical spectral filtering pulse shaper. The Ti:Sapphire laser pulse was collimated and aligned parallel to the optical table surface. At the entrance of the setup, an 800 lines/mm grating was aligned with the input beam close to the Littrow condition for the maximum diffraction efficiency where the diffracted beam is collimated with the incident beam [45]. The spectrally dispersed pulses were collimated by a lens which was one focal length away from the grating. After the lens, a high reflector was placed on the focal plane of the lens. The laser beam was sent back to the entrance and slightly off from the original beam height in order to pick up the modified pulses. The alignment was a little tricky since we wanted to keep the distance between the grating, lens and the reflector exactly at the focal length. If the distance between the lens and the grating is not equal to the focal length, the pulse shaper will add chirp to the pulse which will stretch or compress the output pulse. By looking at the output pulse width, we were able to find out the correct distance between the lens and the grating. If the distance between the lens and the reflector is not equal to the focal length, the output beam will diverge. Therefore, by collimating the output beam, the distance between the lens and the reflector can be proper

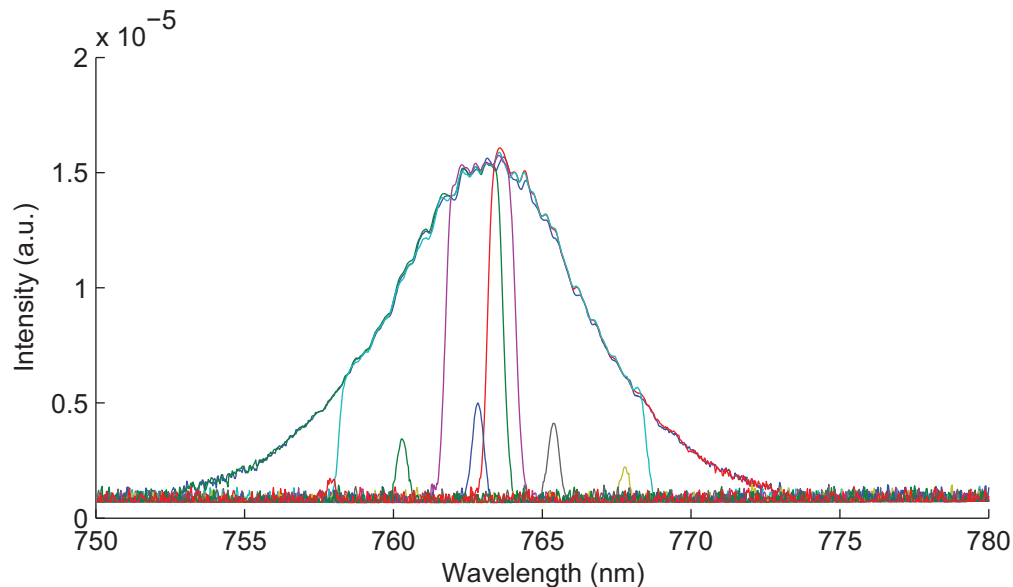


Figure 36: The shaped spectra.

adjusted. However, this aligning procedure needed several iterations since the two distances are not independent.

In the Fig. 35 setup, two D-shaped edge mirrors are close together instead of a single piece of reflector. An adjustable slit is also placed in front of the two edge mirrors. By adjusting the slit width, the total bandwidth of the laser pulse can be tuned. As a result, the pulse width will change accordingly. The distance of the two mirrors in the direction perpendicular to the beam can also be changed, which gives the desired energy splitting for output double pulses. The most intriguing feature of this setup is the ability to produce a delayed double pulse by changing the distance between the two mirrors in the direction of the beam.

Fig. 36 shows several measured shaped Ti:Sapphire laser spectra. The spectrum bandwidth and the center wavelength can be easily tuned. The minimum bandwidth is down to 0.3 nm (or 0.6 meV). Fig. 37 shows a time-resolved measurement for a two-color double pulse. The energy splitting of the two pulses is 3.3 meV and the time delay is 12.6 ps.

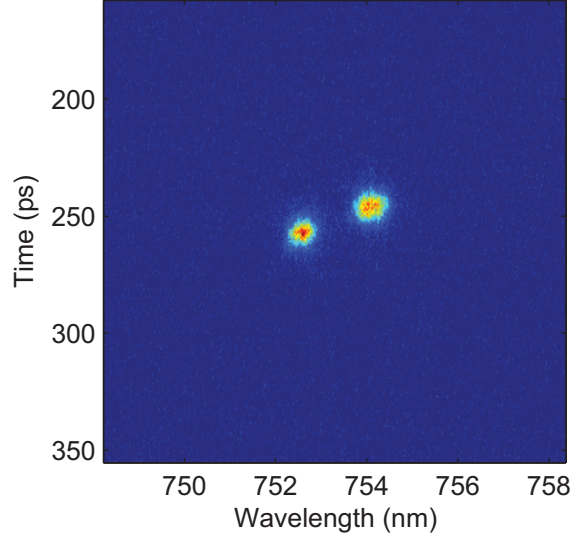


Figure 37: A typical two-color double-pulse measurement after the pulse shaper.

2.3.3 Pulse measurements

The femtosecond laser pulse is too short to be measured directly by photodetectors. The only thing is comparable to the pulse is the pulse itself. Fig. 38 is a typical schematic setup, called an autocorrelator, which uses the pulse itself to measure the pulse width. The setup is based on a Mach-Zehnder interferometer which is symmetrical for the two beam path. One of the retroreflectors is driven by a speaker (actually a voice coil). The detector is a GaP photodiode which is only sensitive to 150 - 550 nm wavelength range. The Ti:Sapphire laser pulse is around 700 -1000 nm. The detector also involves a nonlinear up-conversion process, called two-photon absorption [46]. In order to measure pulse width and the dispersion, two beams collinearly hit on the photodetector. A function generator drives the speaker at 3 Hz and triggers an oscilloscope which acquires the signal from the photodetector. The speed of the acquisition has to be much faster than the period of the speaker in order to resolve interference fringes. The two-photon absorption signal is proportional to

$$D(\tau) = \int_{-\infty}^{\infty} |[E(t) + E(t - \tau)]|^2 dt. \quad (2.21)$$

Fig. 39 is an interferometric autocorrelation measurement for the laser pulse generated from our prism-based Ti:Sapphire oscillator. The measured pulse width is about 353 fs and the spectral bandwidth is 3 nm, which gives $\Delta\tau\Delta\nu \approx 0.4$ as predicted in [30] for a Gaussian shaped pulse.

Fig. 40 is an autocorrelation measurement for a laser pulse from our chirped-mirror-based Ti:Sapphire oscillator. The setup used in this measurement was a little different from Fig. 38. Instead of a GaP photodiode, a light-emitting diode (LED) was used as the nonlinear detector. The band gap of the LED gain material is higher than the photon energy from a Ti:Sapphire oscillator, which means it needed a two-photon process to excite an electron from the valence band to the conduction band. As seen in this figure, the measured pulse was highly chirped. Due to the low number of sampling points, there was some distortion on the measured signal which is supposed to be symmetric.

2.4 TIME-RESOLVED EXPERIMENT SETUPS

From previous sections, we have well-prepared Ti:Sapphire laser pulses as a tool to explore ultrafast dynamics in several semiconductor systems. In this section, two kinds of time-resolved detection apparatus are introduced: one is a pump-probe setup for femtosecond dynamics measurements; the other is a streak camera system which features a 2 ps resolution and photon counting sensitivity.

2.4.1 ULTRAFAST NONLINEAR OPTICAL SAMPLING OSCILLOSCOPE

The pump-probe setup is the most popular approach for time-resolved experiments. Usually, a laser pulse, called the pump laser, first excites a system and induces some property change. The change often varies with time. Another laser pulse, called the probe laser, has a certain time delay τ with respect to the pump pulse to detect the property at different time τ . Depending on the property we are interested in, different detecting methods are used such as transmission, reflection and emission etc.

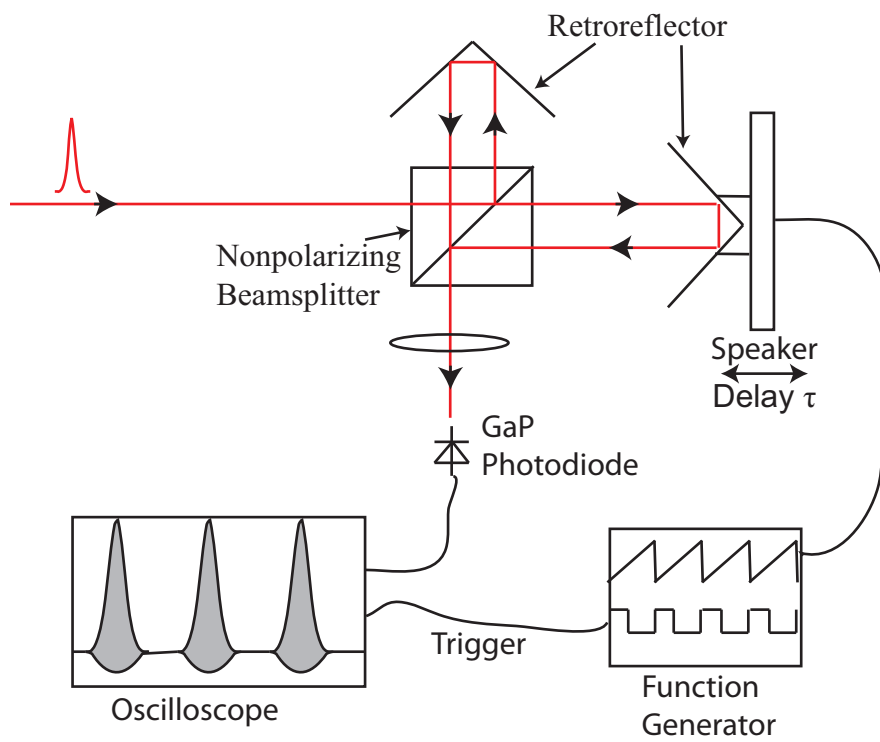


Figure 38: The autocorrelator setup.

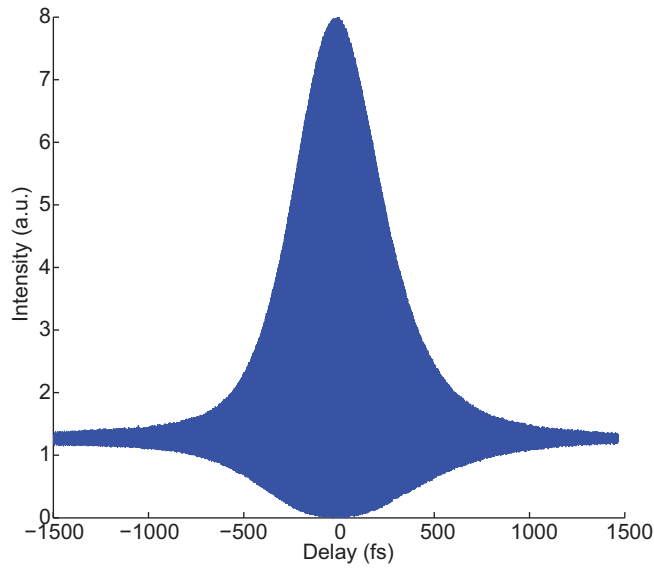


Figure 39: A interferometric autocorrelation measurement for a laser pulse with center wavelength at 850 nm.

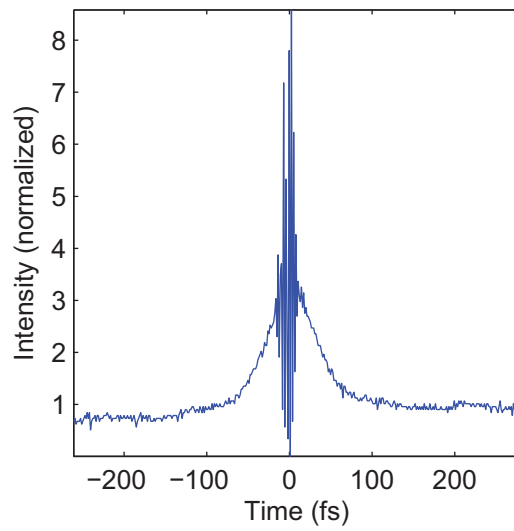


Figure 40: The interferometric autocorrelation of a chirped short pulse which is generated by our chirped-mirror-only cavity.

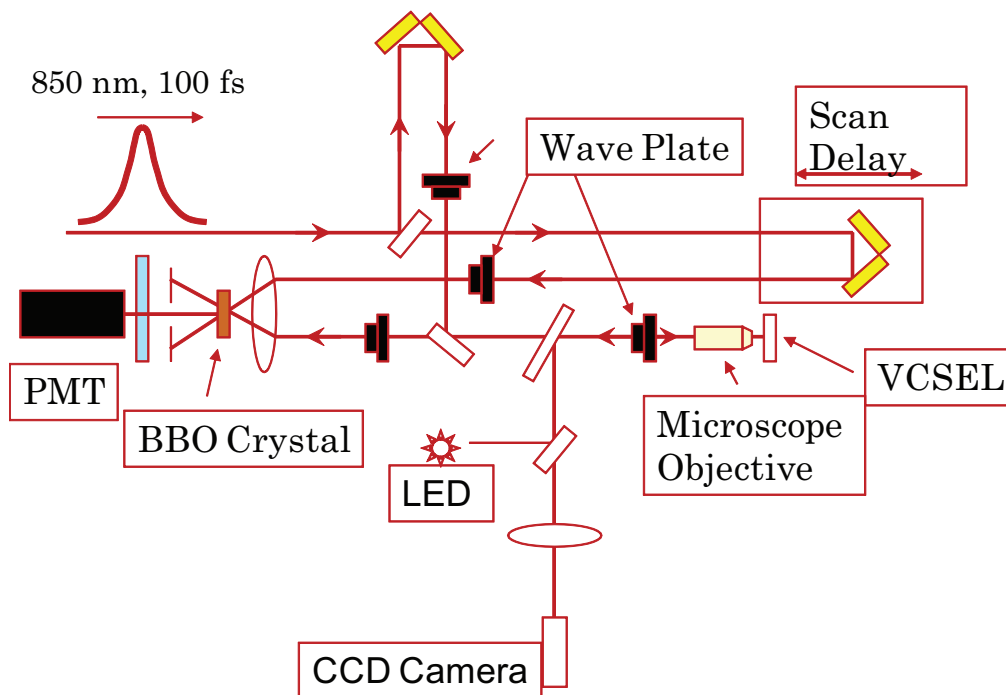


Figure 41: The pump-probe experiment setup for the VCSEL experiments.

Fig. 41 shows the pump-probe setup for resonant injection and probing ultrafast dynamics from a VCSEL. The injection laser pulse is from our home-built tunable Ti:Sapphire laser. The center wavelength of the laser pulse was tuned resonant to the emission wavelength of the VCSEL. The bandwidth of the injection laser pulse is usually around 5 nm, which covers the whole emission range of the VCSEL. Since the emission window of the VCSEL is on the order of tens of microns, a confocal microscope was built to monitor the injection location on the surface of the VCSEL wafer. Fig. 42 shows a single-mode VCSEL device image taken with a 40X microscope objective.

The delay scan was driven by a 100 mm travel stepper motor stage with 1 μm resolution. The signal was detected by a photomultiplier tube (PMT) with a preamplifier and collected with a National Instruments multi-function data acquisition card. The stage was set up in a way that sent out the trigger signal to the DAQ card and synchronized the data acquisition with the delay scan.

Many single-mode VCSELs have a preferred linear polarization due to the strain built in at the manufacturing stage. In order to study modes with different polarization, two half-waveplates and two quarter-waveplates were used to control the injected laser pulse polarization and the detection of the VCSEL emission polarization.

At the detection stage, an optical up-conversion technique is implemented. The key component is a nonlinear crystal, which is a β -BaB₂O₄ (BBO) crystal in our case. The emission from the VCSEL is up-converted by second harmonic generation. The probe pulse works as a gating signal. The up-converted signal only occurs when both probe pulse and the light emission from the VCSEL interact with the BBO crystal at the same time.

The second harmonic generation is related to the nonlinear response for electric field. The polarization density can be expressed as [46]:

$$\mathbf{P} = \chi\epsilon_0\mathbf{E} + 2\chi^{(2)}\mathbf{E}^2 + \dots$$

where the first term is the linear response and the higher order term is related to nonlinear response. The second order term represents the process of two photons forming a single higher energy photon, which has to be satisfied with the energy conservation,

$$\hbar\omega_{probe} + \hbar\omega_{VCSEL} = \hbar\omega_{signal}$$

and the momentum conservation,

$$\vec{k}(w_{probe}) + \vec{k}(w_{VCSEL}) = \vec{k}(w_{signal}).$$

These two requirements are known as the phase-matching condition. Since all the materials have dispersion, the phase-matching condition can not be satisfied automatically. In the case of a crystal, the birefringence makes the phase-matching possible in a certain direction. For the single-axis crystal BBO, there are two kinds of phase-matching condition, depending on the polarization of input signal: one is that the probe beam and VCSEL emission have same polarization, known as type-I phase-matching; the other is that the probe beam and VCSEL emission are cross-polarized, called type-II phase-matching [47]. In the VCSEL experiments, we used type-I phase-matching due to the higher up-conversion efficiency.

2.4.2 Streak Camera

Although the ultrafast optical up-conversion technique has time resolution limited by the pulse width, the alignment is tricky and the detection efficiency and sensitivity are low. If the dynamics of the studied system are on the order of picosecond, a streak camera system will suit the application better.

Fig. 43 shows a schematic setup for a commercial Hamamatsu streak camera system. An optical signal first hits on a fast-response photocathode which converts photons to electrons. The electrons are accelerated to fly through the streak tube which is in a high vacuum state. As electrons pass through the streak tube, a vertical electrical field disperses the electrons along the vertical direction. In the time order of the photons hitting on the cathode, electrons will hit on different positions of a phosphor screen. At the phosphor screen, electrons are converted to photons and then detected by a CCD camera which converts photons back to electrons again.

Compared to the optical sampling method, a streak camera system is much more sensitive over 300 nm to 850 nm range. The setup is much easier and there is no need for a time delay scan, which increases the measurement stability and speed. In most cases, the optical sampling method only samples one point at a time. Instead, a streak camera system can

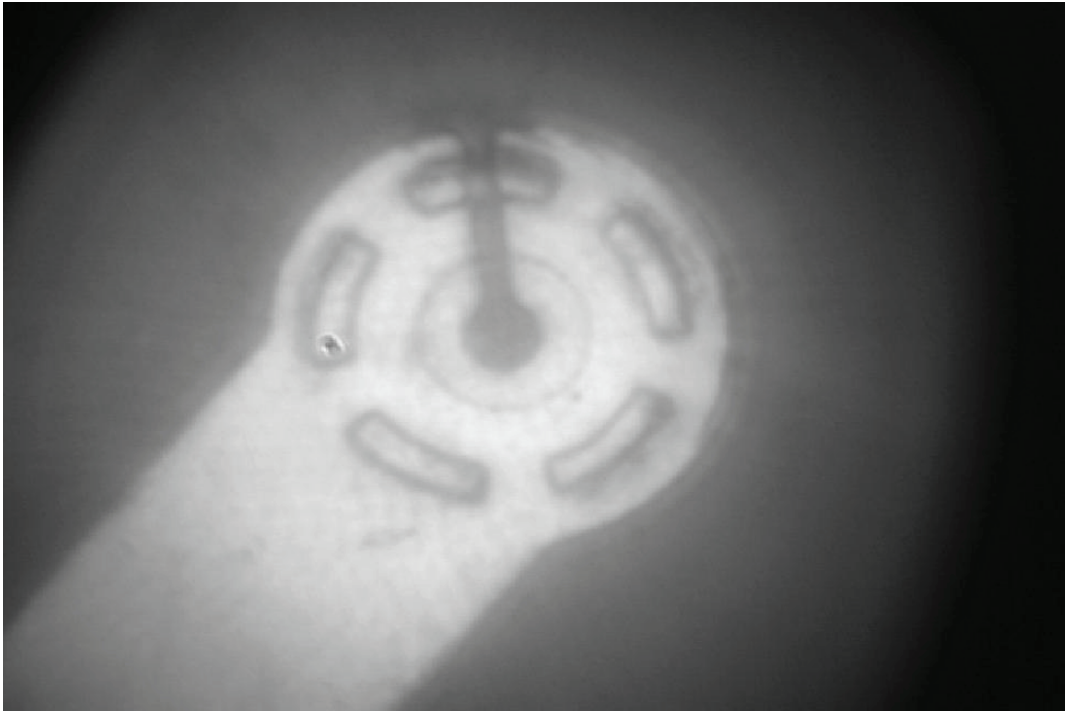


Figure 42: A typical image of a single-mode VCSEL device.

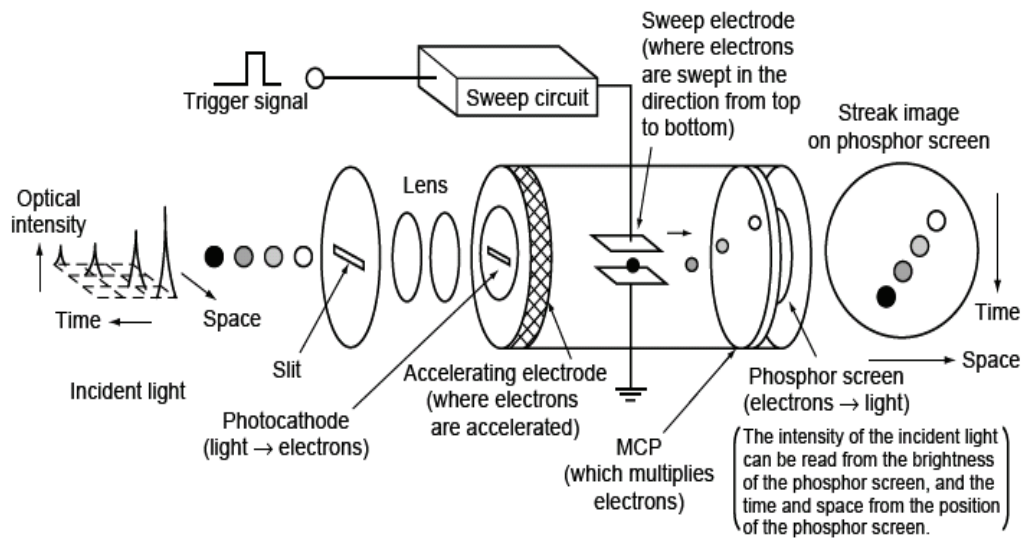


Figure 43: The operation principle of streak camera. (The picture is from Hamamatsu.)

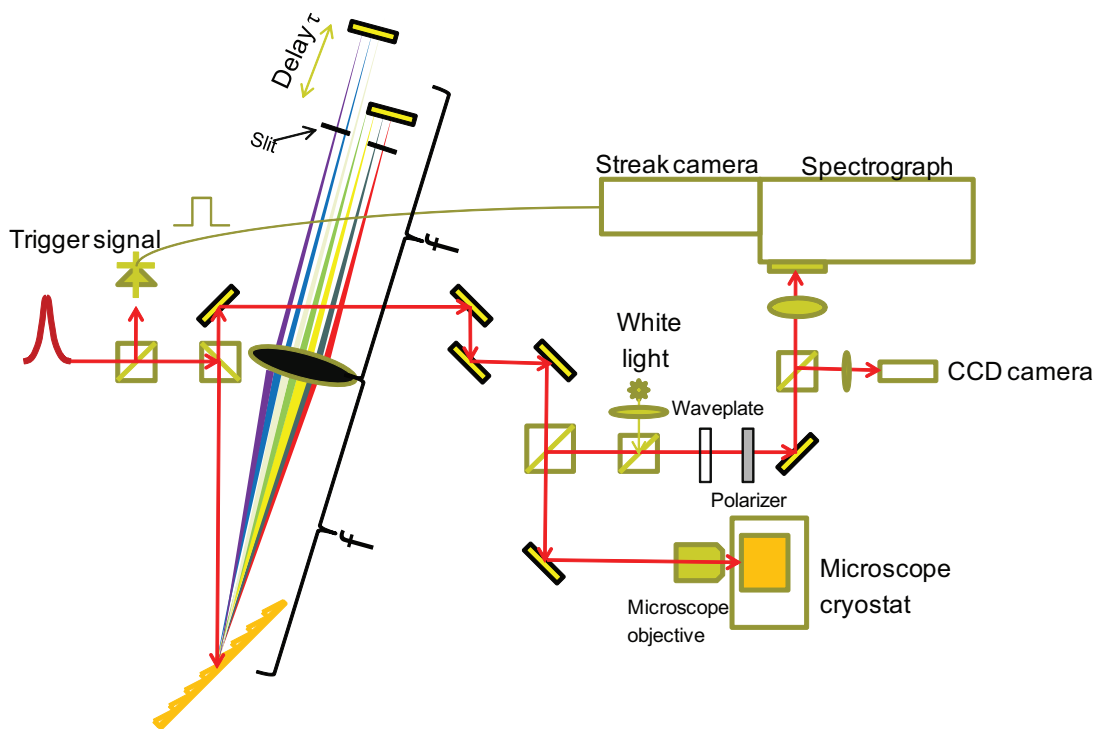


Figure 44: The streak camera experiment setup for quantum dots experiment.

time-resolve one line at a time. If a spectrometer is connected to the streak camera, multi-channel time-resolved spectra can be done pretty quickly. The optical sampling method only measures the signal average over millions of pump pulses. In addition, streak cameras can do single-shot measurements, which are useful for studying correlations between different pump laser pulses.

Fig. 44 is the schematic setup for the streak camera system which was used to measure our quantum dots emission dynamics. Before being sent to the sample stage, the Ti:Sapphire laser pulse passed through a pulse shaper which can tune the laser resonant to the quantum dots excitation state and limit the bandwidth of the laser pulse.

3.0 QUANTUM DOTS

In this chapter, we identify one of the emission lines as arising from positive trions (two holes and one electron) in nominally undoped quantum dots, based on time-resolved microscopic photoluminescence (μ PL) from single self-assembled GaAs/Al_xGa_{1-x}As quantum dots. The trion is formed via tunneling of one electron out of the dot after optical excitation of a biexciton. The rise time of trion emission line matches the decay of the biexciton due to electron tunneling [48].

3.1 TRION FORMATION IN GAAS-ALGAAS QUANTUM DOTS BY TUNNELING

When more than one electron and hole occupy the same quantum dot (QD), Coulomb and exchange interactions lead to energy shifts and altered lifetimes which often make it hard to identify the optical lines and the mechanisms for their appearance and decay. These shifts can be used for useful nonlinear effects for single photon sources [49], quantum logic gates [50], and quantum dot lasers [51]. Time-resolved microphotoluminescence (μ PL) spectroscopy provides a powerful way to study single dots precisely and understand excitonic relaxation in atomic-like systems [52].

In neutral, undoped quantum dots under increasingly strong optical excitation, one naturally expects emission lines from excitons (1e1h), biexcitons (2e2h), and higher orders of electron-hole pairs as single dots absorb additional photons. When the dots have unmatched holes and electrons, emission lines can come from charged states, such as positive trions (1e2h) or negative trions (2e1h). Few-particle effects caused by these extra charges lead to

an energy splitting between neutral states and charged states [53]. While it is easy to see how trions could arise in doped dots with excess charged carriers [54], for trions to appear in undoped dots either extra free carriers must be captured from outside the dot, or photo-excited carriers must escape the dot. In nominally undoped InAs [55] and CdSe [56] dots, the appearance of trions has been attributed to capture of free carriers excited in the substrate by photons with energy well above the band gap of the barrier material.

Here I present evidence that trions in a new type of undoped GaAs quantum dots [16] can even appear for below-barrier excitation. The trions are formed when electrons escape the dots by tunneling as shown by time-resolved studies in samples with different barrier thicknesses. This interpretation explains why time integrated spectra [57] show a trion line that is much more intense than the bi-exciton emission.

The structures studied here consist of hierarchically self-assembled GaAs/ $\text{Al}_x\text{Ga}_{1-x}\text{As}$ QD's grown by molecular beam epitaxy combined with in situ etching of GaAs-capped InAs QDs [16]; the samples are very similar to those studied in Ref. [57], and the binding energy of 2.9 meV for the trion determined in Ref. [57] is very close to the value of 3.0 meV which we determine here. The QD size dispersion produces inhomogeneous broadening of about 10 meV for the ground state emission, which is less than that of "natural" QD's occurring due to thickness fluctuations of GaAs/AlGaAs quantum wells (QW). Since the dot material is GaAs, the emission wavelength range is well matched to the multi-alkali photo cathode in our streak camera system, which makes the ultra high speed and high sensitivity measurements possible. Compared to self-assembled InAs QD's, the QD's studied here have an inverted shape, and they are located under a thin GaAs QW (see Ref. [16]). The GaAs QD's are sandwiched between two $\text{Al}_x\text{Ga}_{1-x}\text{As}$ layers. The bottom $\text{Al}_{0.45}\text{Ga}_{0.55}\text{As}$ layer (thickness D) inherits the nanohole structures from InAs quantum dots after etching. By varying the barrier thickness D , different sizes of nanoholes on the top of the $\text{Al}_{0.45}\text{Ga}_{0.55}\text{As}$ layer can be realized. For the samples investigated here, with $D = 7$ and $D = 10$ nm, the holes have a depth of 4.1 and 3.2 nm, respectively, and a lateral width of 50 nm (see Ref. [16]).

The QD samples were mounted inside a continuous flow microscope cryostat, and all of the experiments were performed at a temperature of 10 K. A tunable mode-locked ultrafast Ti:Sapphire oscillator with a repetition rate of 76 MHz was used as pump laser. The laser

pulse spectral width (FWHM) was 3 nm. The measurement stage of the experimental setup consisted of a confocal microscope and a spectrograph connected to a Hamamatsu streak camera system with a time resolution down to 3 ps. Using a high numerical aperture ($N_A = 0.8$) microscope objective, we were able to focus the laser beam down to 1 μm . In this experiment, we studied two kinds of samples with different QD surface densities: two high-density quantum dot (HDQD) samples with 40 dots per μm^2 , and one low-density quantum dot (LDQD) sample with an average of 0.5 dots per μm^2 .

Figure 45 shows the time-resolved μPL of HDQD samples with different barrier thicknesses D for near-resonant excitation with a photon energy of 1.699 eV, which is above the dot luminescence energy and below the energy of the QW's (1.777 eV) next to the dots. The fundamental emission energy is higher for the sample with the thicker barrier, which indicates stronger confinement [16]. The linewidth of the emission peak is 10 meV. We extracted the decay dynamics for each emission maximum of the two QD samples, shown in Figure 45(c), by integrating over a 10 meV spectrum width. Both samples have similar rise times of ~ 38 ps but different decay times, 318 ± 4 ps for the $D = 10$ nm QD sample and 254 ± 4 ps for the $D = 7$ nm sample.

The total decay rate, τ_{tot}^{-1} , of excitons is the sum of radiative decay rate, τ_{rad}^{-1} , and the rate for electron (or hole) tunneling out of the dot, τ_{tun}^{-1} , i.e.,

$$\frac{1}{\tau_{tot}} = \frac{1}{\tau_{rad}} + \frac{1}{\tau_{tun}} \quad (3.1)$$

The stronger confinement of the dots with thicker barrier should imply larger oscillator strength, which means shorter decay time [58], but here the sample with thicker barrier has longer lifetime. Therefore, we attribute the significant decay time difference for the two samples to tunneling through the barrier between the QD's and the QW's. Since the effective mass of heavy holes is much larger than that of electrons, the rate of heavy hole tunneling is much lower than that of electrons (still shorter than laser pulse interval). Hence, electron tunneling should contribute most to the initial stage of tunneling decay. Exponential dependence of tunneling time with barrier thickness has been shown for AlAs/GaAs double quantum well samples [59] and vertically aligned double quantum dots [60].

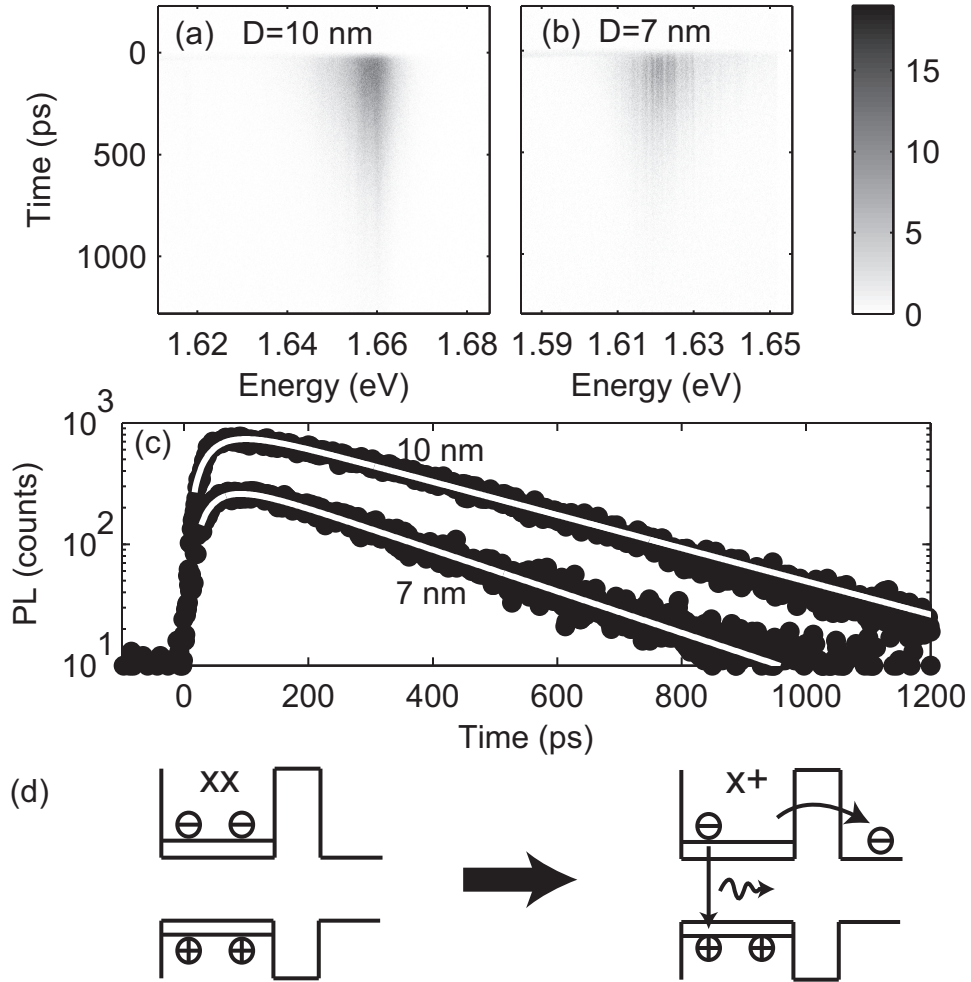


Figure 45: Time-resolve μ PL measurements of high density QD samples with different barrier thicknesses of $D =$ (a) 10 nm, and (b) 7 nm. (c) The decay dynamics for both samples, where the solid white lines are exponential fits. The pump power is 200 μ W. (d) The process of a biexciton (XX) turning into a positive trion (X^+) by electron tunneling.

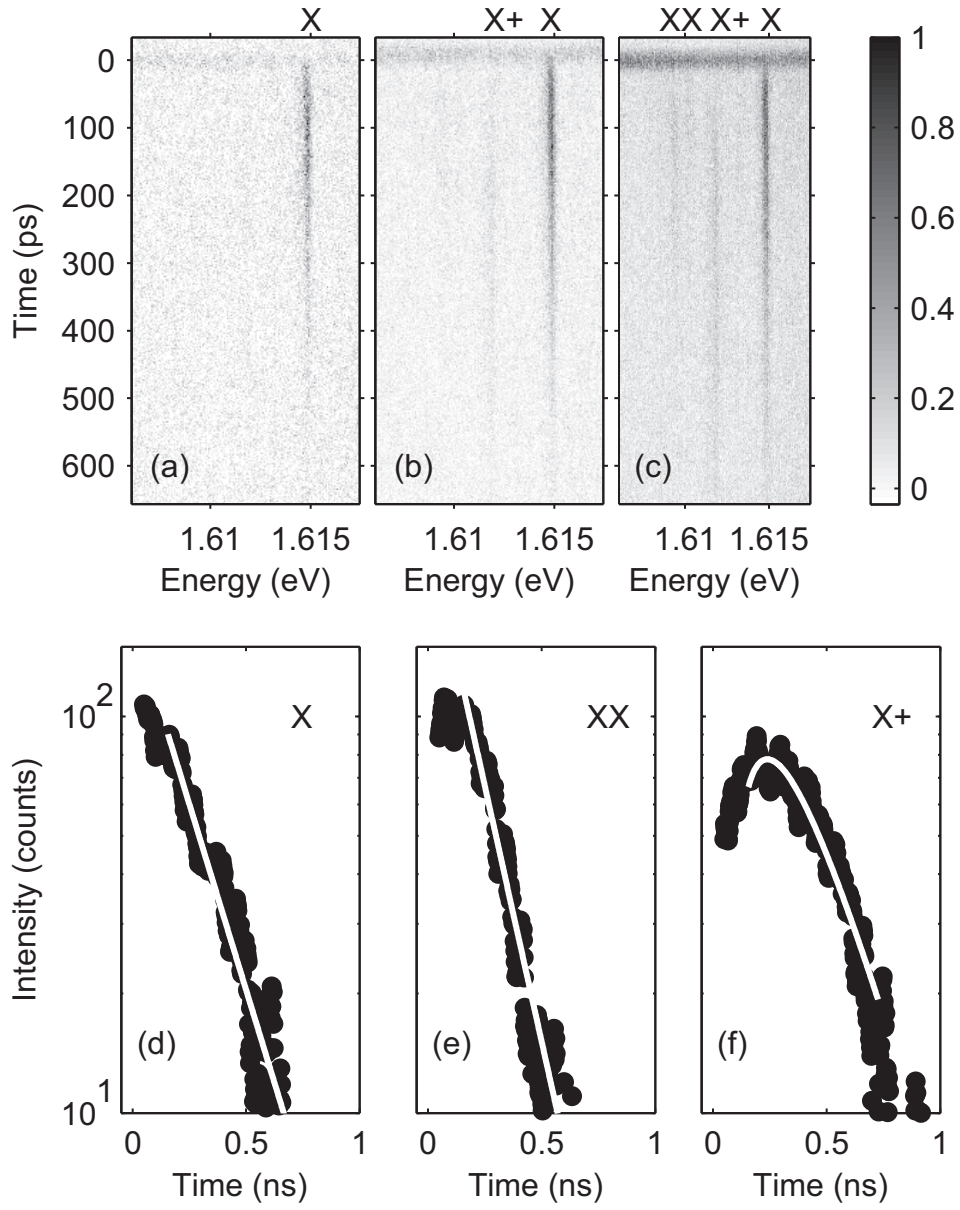


Figure 46: Time-resolved μ PL for single QD's. (a), (b) and (c) are streak camera images for pump powers of $40\mu W$, $80\mu W$ and $160\mu W$, respectively (The dark line at time zero is scattered light. The intensity is normalized in each image); (d), (e) and (f) are decay dynamics of exciton (X), biexciton (XX) and positive trion (X+), respectively, where the black dots are experimental data and the solid white curves are simulations from the rate equations (3.4).

Since the lateral sizes of our QD's are large compared to their heights, we can approximate tunneling as a one-dimensional process. By solving the one-dimensional Schrodinger equation, the transmission coefficient T is

$$T = \left(1 + \frac{(k^2 + \beta^2)^2}{4k^2\beta^2} \sinh^2 \beta D\right)^{-1} \stackrel{\beta D \gg 1}{\approx} \Delta \exp(-2\beta D), \quad (3.2)$$

where $k = \sqrt{2m_{1,e}E}/\hbar$, $\beta = \sqrt{2m_{2,e}(V_0 - E)}/\hbar$, $\Delta = 16k^2\beta^2/(k^2 + \beta^2)^2$, and $m_{1,e}$ and $m_{2,e}$ are the effective electron masses of GaAs and GaAs/Al_{0.45}Ga_{0.55}As, respectively; V_0 is the conduction band offset for GaAs/Al_{0.45}Ga_{0.55}As heterostructures, and E is the electron confinement energy inside the quantum dots. Under the WKB approximation, the tunneling time varies exponentially with the barrier thickness D according to [61]

$$\tau_{tun} \approx \frac{2m_{1,e}a}{\hbar k T} \approx \frac{2m_{1,e}a}{\hbar k \Delta} \exp(2\beta D), \quad (3.3)$$

where a is the height of the QDs. Therefore, the QD sample with $D = 10$ nm has a tunneling time of the order of several tens of ns. We can approximately treat the total decay time as mainly radiative decay time for this thicker-barrier sample. From Eq. (3.1) and the fitted decay time for the thinner-barrier sample, we obtain an electron tunneling time of 1.262 ns. By comparison, Equation (3.3) gives us an electron tunneling time of 1.1 ns for a barrier thickness of $D = 7$ nm, which is in fairly good agreement with the value extracted from the experimental data.

Tunneling of an electron from a biexciton should produce a positive trion that can be resolved in single dot experiments due to the absence of inhomogeneous broadening and the resulting emission line width. With the LDQD samples, we were able to excite single QD's without a mask mesa pattern or etching the samples, as was necessary in Ref. [55]. The LDQD sample we used here had a barrier thickness of $D = 7$ nm. As Figure 46 (a)-(c) shows, the single QD spectra have sharp emission lines with 240 μ eV line width, which is limited by the system resolution. At very low pump power, the single QD's only show a fundamental excitonic line (X) at 1.615 eV. With increasing pump power, we can clearly see two more emission lines at 1.612 eV and 1.609 eV. As discussed in the following, these lines correspond to the positive trion (X+) and the biexciton (XX), respectively.

From Figure 46 (c), the X+ line shows a clearly delayed emission with respect to the XX and X lines. In principle, multi-excitonic complexes could also arise from extra carriers excited in the material surrounding the dots, followed by migration into the dots [62], since the background doping is nominally around 10^{15} cm^{-3} in GaAs-based structures [63]. Creation of these complexes due to in-tunneling of carriers would imply a much longer rise time for the biexciton emission, however, as carriers diffuse to the dots. Since we excited below the barrier, we do not expect this to be a strong process, although a small amount due to two-photon absorption is possible. The long rise time of the trion line compared to the rise time of the biexciton line gives a clue to the positive trion formation process: a biexciton loses an electron through tunneling, leaving behind a positive trion. At the same time, a biexciton can also decay by photon emission, leaving behind an exciton. Keeping these points in mind, we can write a simple set of rate equations to explain the multi-excitonic decay dynamics:

$$\left\{ \begin{array}{l} \frac{dN_{xx}}{dt} = -\frac{N_{xx}}{\tau_{xx,rad}} - \frac{N_{xx}}{\tau_{xx,tun}} \\ \frac{dN_x}{dt} = -\frac{N_x}{\tau_{x,rad}} - \frac{N_x}{\tau_{x,tun}} + \frac{N_{xx}}{\tau_{xx,rad}} \\ \frac{dN_t}{dt} = -\frac{N_t}{\tau_{t,rad}} - \frac{N_t}{\tau_{t,tun}} + \frac{N_{xx}}{\tau_{xx,tun}} \end{array} \right. \quad (3.4)$$

where $N_x(t)$, $N_{xx}(t)$ and $N_t(t)$ are the ensemble average at a single point in time of the number of excitons, biexcitons and trions, respectively, for a single dot excited many times by the repeated laser pulse. The lifetimes $\tau_{x,rad}$, $\tau_{xx,rad}$ and $\tau_{t,rad}$ are the radiative decay times for excitons, biexcitons and trions, respectively, and $\tau_{x,tun}$, $\tau_{xx,tun}$ and $\tau_{t,tun}$ are the electron out-tunneling decay times for the excitons, biexcitons and trions.

Eq. (3.4) implies that the biexciton population has single exponential decay. Since the density of biexcitons is small compared to that of excitons, the contribution to the exciton population due to biexcitons radiatively decaying into excitons is negligible. Therefore, the exciton line also has approximately single exponential decay. Since the biexciton and exciton data can each be fit by single parameter fits, we have a simple two-parameter fit for the trion decay. At high pump power, because we excite the dots with photon energy

above the lowest confined states (but still well below the barrier height), there is an initial population of excitons and biexcitons in excited states. This means that the population is not entirely in the lowest exciton and biexciton states until after a thermalization time of around 150 ps. Therefore, we only fit the intensity decay data after $t = 156$ ps.

As shown in Figure 46 (d)-(e), we can obtain good fits to all three time-resolved intensity plots, for $\tau_{x,tot} \approx 232$ ps, $\tau_{xx,rad} \approx 446$ ps, $\tau_{t,rad} \approx 289$ ps, $\tau_{xx,tun} \approx 271$ ps and $\tau_{t,tun} \approx 572$ ps. The electron out-tunneling time for the trion, $\tau_{xx,tun}$, is almost twice of $\tau_{t,tun}$ consistent with the fact that the biexciton has two electrons, which doubles the total tunneling rate.

The consistency of these fits confirms the identification of the line we have identified as coming from the trion. Although in some cases the positive trion line can lie higher in energy than that of the exciton [64], it can have lower energy than the exciton for relatively large QD's [63], as seen here. The energy shift is also confirmed by polarization dependence measurements [57].

In conclusion, time-resolved μ PL measurements of unstrained self-assembled GaAs/Al_xGa_{1-x}As QDs with high spectral resolution are consistent with the picture that at high excitation density, biexcitons are formed in the dots, followed by electron tunneling out of the QDs, leaving behind a positively charged trion. This indicates that for the thin barrier samples, the tunneling effect is an important source for the excitonic decay.

3.2 RABI OSCILLATIONS

The broadband femtosecond laser source was initially used to do time-resolved photoluminescence experiment. On the other hand, the energy splitting between exciton and biexciton energy level is on the order of a few meV at the temperature of 10 K. Therefore, it is impossible to selectively excite different transitions. As discussed in Section 2.3.2, the constructed femtosecond laser pulse shaper is able to trim down the pulse bandwidth to 0.6 meV. A well-defined two-color double pulse can address the excitonic and biexcitonic transitions for the control of condition quantum gate operation.

Fig. 47 is a two-dimensional photoluminescence excitation (PLE) measurement on a

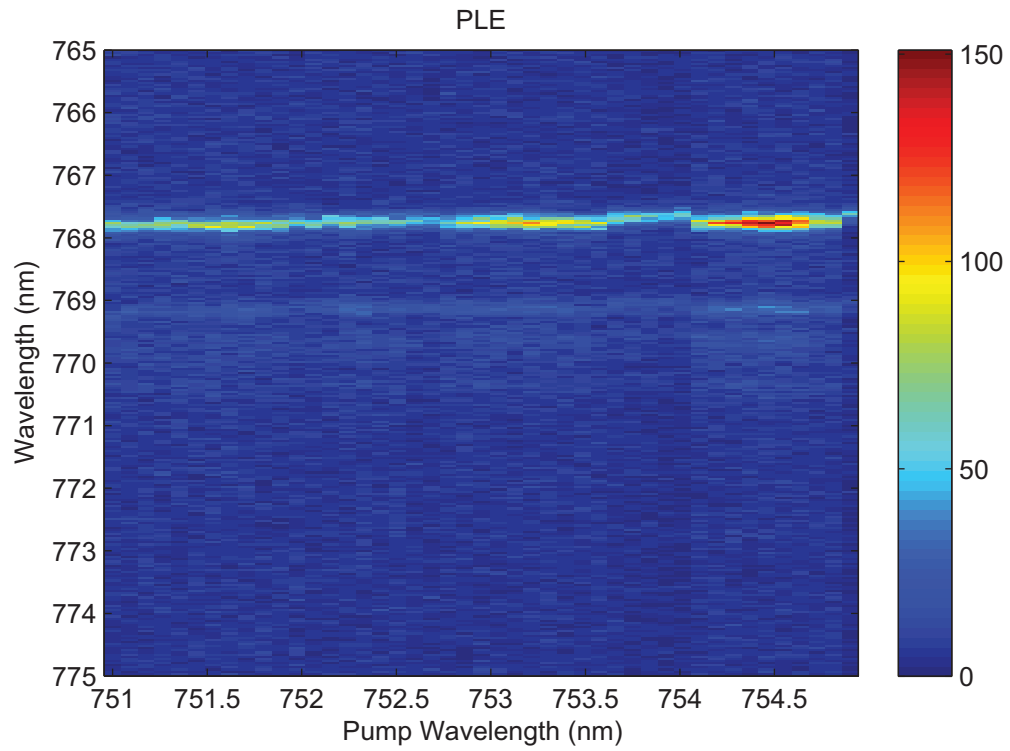


Figure 47: A two-dimensional photoluminescence excitation (PLE) measurement on a single quantum dots. The horizontal axis shows excitation wavelength, whereas the vertical axis is the emission spectra.

single quantum dot. The pump beam was focused down to a sub-micron spot size in order to excite as few dots as possible on a low-density quantum dots sample. To isolate a single dot, the pump laser with a bandwidth of 0.6 meV was tuned resonant to an excited state for a single quantum dots. The horizontal axis is the excitation wavelength and the vertical axis is the emission wavelength. At 768.2 nm emission wavelength, there is a sharp line which is much stronger than the line around 769 nm emission wavelength. That is because the excitation laser only has 0.3 nm bandwidth which mainly excites single excitons. At the same time, the pump power is sufficiently low so that it does not saturate the excitonic transition.

With the sharp resonance, I can also select the quantum dots I want to excite and differentiate different quantum dots by their resonant frequency. Fig. 48 shows the photoluminescence measurement from three quantum dots by scanning the excitation wavelength. Dot 1 and dot 2 show pretty sharp resonance which means the lower-order excited states have pretty narrow linewidth. However, Dot 3 shows pretty constant PL at 769 nm which might be caused by broad high-order, excited-states resonance. For each dot, the fundamental excitonic line is much stronger than the trion line on the lower energy side.

Rabi oscillation is a unique signature of light-matter quantum interaction for a two-level system which is analogous to a classical harmonic oscillator. At resonant excitation, the PL of quantum dots exhibit a sinusoidal oscillation versus the excitation pump power, which is proportional to the field integral [65],

$$\theta(t) = \int_{-\infty}^t pE(t')/\hbar dt', \quad (3.5)$$

where p is the transition dipole matrix element and E is the electric field of the excitation pulse.

Fig. 49 (a) shows the luminescence intensity versus the square root of the power for the exciton line at 762.8 nm. The emission saturates for increasing power and shows damped oscillatory behavior. This power dependence indicates Rabi oscillations between the unexcited state and the E_2 single exciton state, as shown in the Fig. 49 (b). The excited excitons relax to E_0 where they produce the observed excitons. The diagram does not take into account

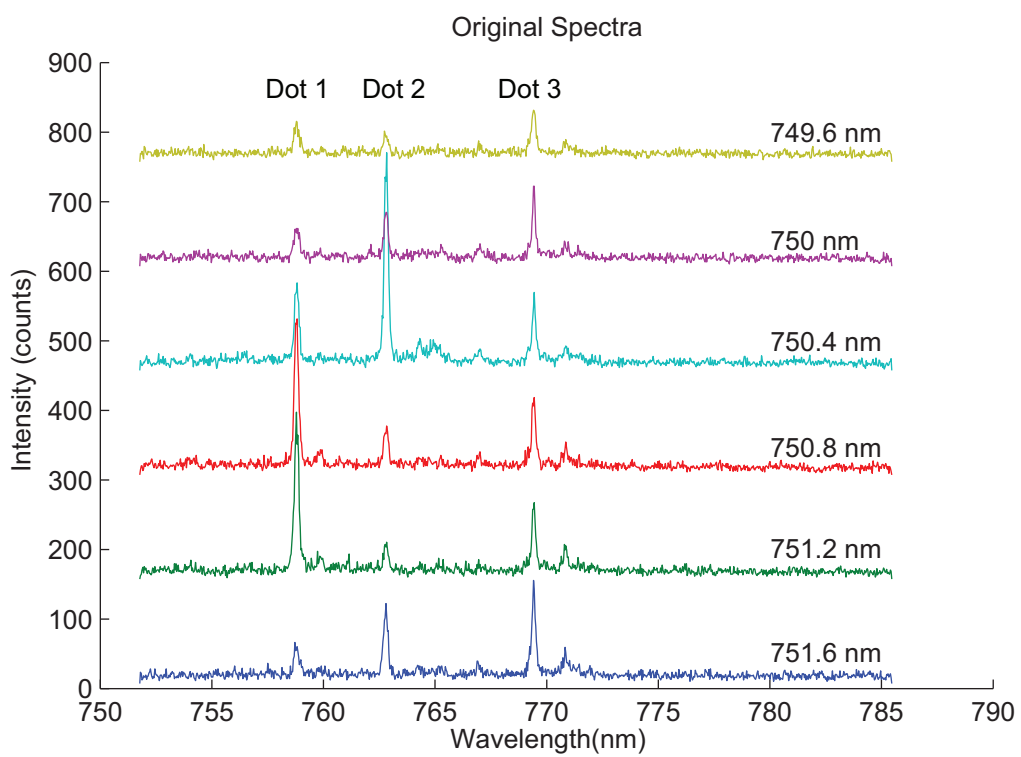


Figure 48: A photoluminescence excitation measurement on a single quantum dots.

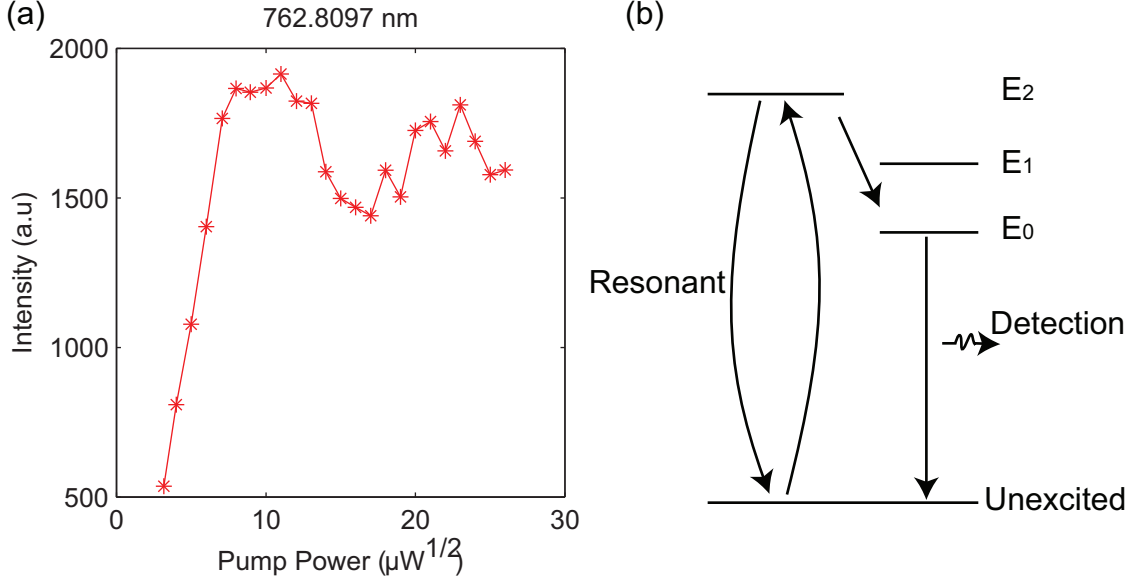


Figure 49: A rabi oscillation measurement on a single quantum dots.

the level fine structure or multiple exciton behavior. The relaxation process disrupts the Rabi oscillations and leads to the damping of the amplitude.

A simple approach for a resonant interaction system is called the rotating wave approximation, which is commonly used in the magnetic pseudospin problem [12]. In the optical resonance case, the pseudospin is actually the Bloch vector which stands for the state of a two-level system. In the rotating wave approximation, the Bloch vector,

$$\rho = (u, v, w) \quad (3.6)$$

works as a solid body which will precess around a certain axis under the external “torque”, the driving electric field. The motion of the Bloch vector can be interpreted by

$$\frac{d\rho}{dt} = \Omega \times \rho$$

and

$$\Omega = \begin{bmatrix} \frac{-pE}{\hbar} \\ 0 \\ \Delta \end{bmatrix}, \quad (3.7)$$

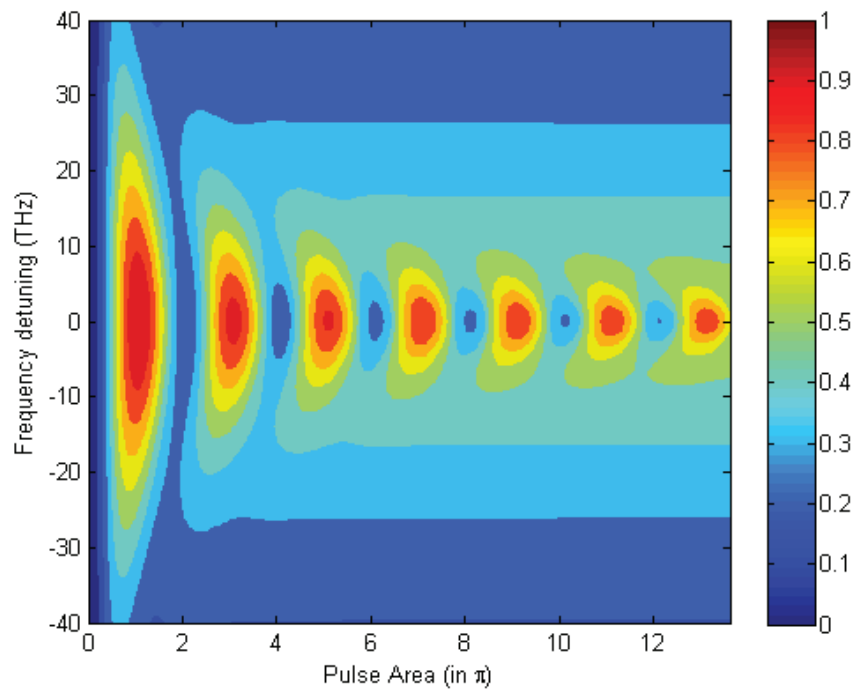


Figure 50: Numerical simulation of Rabi oscillation vs. pump laser frequency detuning.

where Δ the frequency detuning from the resonant frequency. In matrix expression, the optical Bloch equation is

$$\frac{d}{dt} \begin{bmatrix} u \\ v \\ w \end{bmatrix} = \begin{bmatrix} 0 & -\Delta & 0 \\ \Delta & 0 & pE/\hbar \\ 0 & -pE/\hbar & 0 \end{bmatrix} \begin{bmatrix} u \\ v \\ w \end{bmatrix} \quad (3.8)$$

Fig. 50 shows a calculation for the Rabi oscillation versus detuning at the presence of a 2 ps optical pulse excitation. For direct Rabi oscillation observation, the resonant excitation to the E_0 transition should be used. However, it is impossible to do so in the current streak camera setup. For such experiments, a pump-probe setup needs to be added.

4.0 VCSEL MODES

There are two sections in this chapter. For the first section, we have investigated the lasing modes of oxide-confined vertical-cavity surface emitting lasers (VCSEL). The individual Laguerre-Gaussian modes have been spectrally and spatially resolved with scanning confocal microscope with time resolution of 4 ps. Subject to the injection of ultrafast laser pulses, the VCSEL showed irregular pulsed emission which indicates the potential for transverse mode-locking of the VCSEL [66]. In the second section, single-mode vertical-cavity surface-emitting lasers (VCSEL) have been investigated with ultrafast optical modulation. After injection of a subpicosecond laser pulse into the VCSEL cavity, nonlasing modes were excited and produced optical beating in the emission of the VCSEL. By measuring the decay time of nonlasing modes, we find the round-trip gain of nonlasing modes and the stability of the single-mode operation of the VCSELS. At high power, the VCSEL also shows polarization switching effects [67].

4.1 TRANSVERSE-MODES AND MODE-LOCKING

With the mode-locking method, semiconductor lasers can produce picosecond laser pulses at high repetition rates. Besides the pulse generation, mode-locked semiconductor lasers have been used for all-optical clock generation [68] and producing frequency combs for optical metrology [69].

There are two kinds of mode-locking method: active configuration with external modulation and passive configuration with a fast saturable absorber. Since mode-locking requires equidistant mode spacing, the longitudinal modes well-defined by the cavity length are the

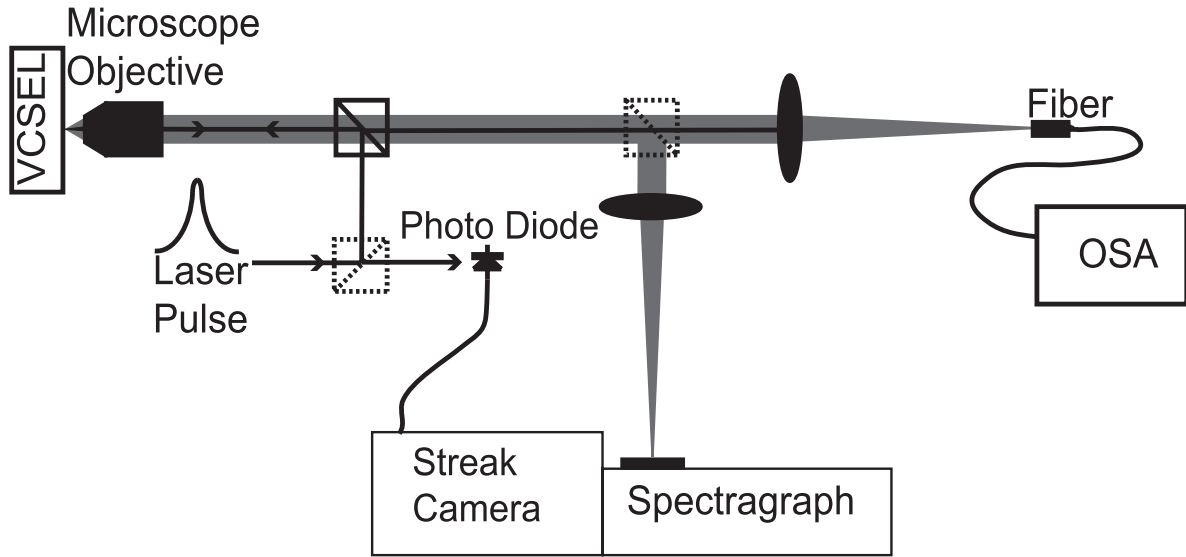


Figure 51: The schematics of experiment setup.

natural choice for the mode-locking. These have been demonstrated with edge-emitting devices in monolithic and external-cavity configurations [70], as well as in vertical external cavity surface emitting lasers (VECSEL) [71]. On the other hand, a VCSEL only has one accessible longitudinal mode due to the short cavity length, which is not possible to be locked. But most VCSELs have complicated transverse modes, and [72] showed these mode-locked lateral modes generated picosecond pulse trains with ion-implanted VCSELs. In principle, these transverse modes can be equally spaced in frequency, allowing mode-locking. This type of mode-locked laser pulse will circulate around the VCSEL's surface. Compared with proton implanted VCSELs, oxide-confined VCSELs have better index guiding and more symmetric mode profile which should work better for transverse mode-locking.

Here, I describe the spatial-spectrally resolved transverse modes of oxide-confined VCSELs. The transverse modes dynamics following ultrafast laser pulse injection were also explored. The competition of the transverse modes led to an irregular pulsed emission.

The multitransverse mode VCSELs we studied are commercially available oxide-confined VCSELs. This type of VCSEL uses lateral wet oxidation of an AlAs layer to produce the aperture necessary for current and optical guiding. The threshold current of our samples is

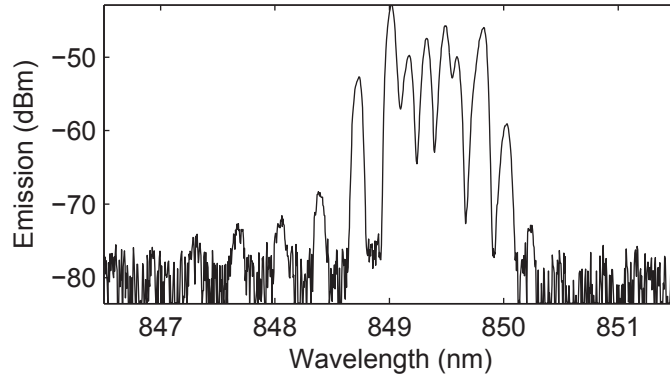


Figure 52: A typical emission spectrum of a multitransverse mode VCSEL at a bias current of 8 mA.

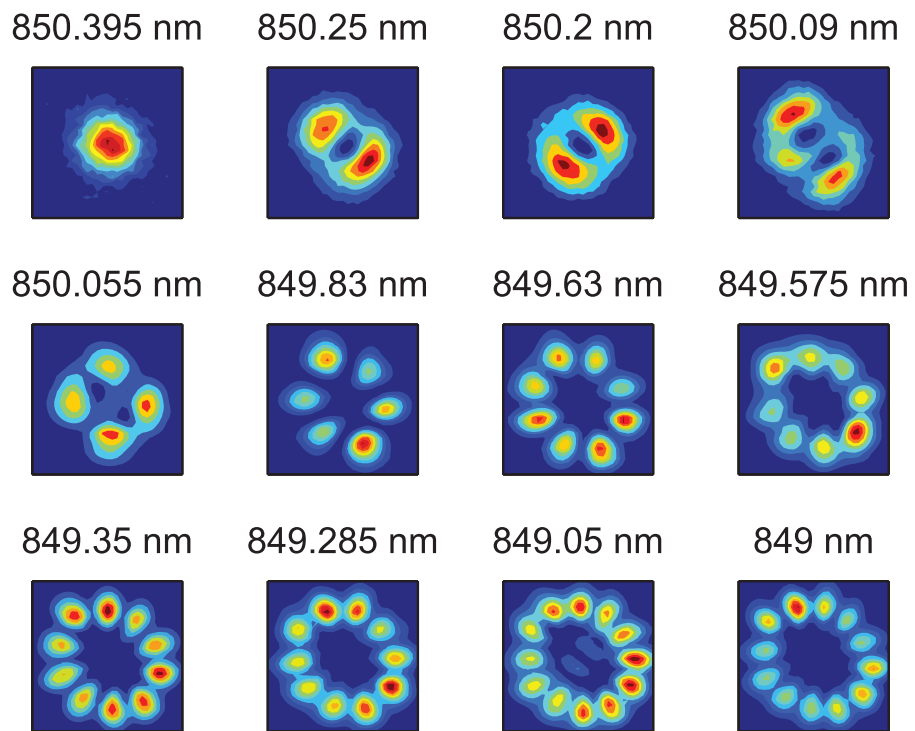


Figure 53: The spatial-spectrally resolved VCSEL's transverse mode at bias current 8.0 mA.

1.6 mA and the emission aperture is 15 μm . The typical emission wavelength is around 852 nm. A 100x microscope objective and a lens with 150 mm focal length were used in a scanning confocal microscope configuration, as shown in Fig. 51, to give us 65x magnification. With an optical spectrum analyzer (OSA) as a detector, we studied the spatial distribution of each transverse mode. A mode-locked femtosecond laser was tuned to a wavelength center at 850 nm with 3 nm bandwidth which covers the whole wavelength range of the VCSEL's emission. After the optical injection, the spatio-temporal resolved emission dynamics were measured by an imaging spectrometer and streak camera system.

As seen in Figure 52, this type of broad-area VCSEL usually shows multimode behavior in a spectrum measurement. Experimentally observed spatial images for each transverse mode are shown in Figure 53. In this spatial-resolved mode experiment, the VCSEL was biased at 8 mA, without any optical injection. We can clearly resolve the spatial distribution of each mode. Similar mode images have been shown by [73] with an etalon filter and an imaging spectrometer. Pereira et al. [74] excited unprocessed VCSEL layers with a ring-shaped optical beam to demonstrate lasing in daisy-shaped Laguerre-Gaussian (LG) modes.

Commercial oxide-confined VCSELs usually have top ring-shaped contacts which inject carriers annularly. The profile of the complex refractive index determines the transverse mode distribution. A comprehensive model [75] has been applied to proton-implanted VCSELs which shows parabolical carrier concentration and temperature distribution near the center active region of VCSELs. From the temperature dependence of the index of refraction [76], we can get a temperature-induced parabolic profile of the index of refraction. The transverse modes have well-known analytical solutions for this kind of so-called square law medium, i.e., $n_r = n_0 - \frac{1}{2n_0}a^2r^2$, where n_r is the effective refraction index, n_0 and a are constants[74]. The normalized mode intensity is given by [74]:

$$I(r, \theta) = \frac{4}{l!} \frac{1}{w^2} \left(\frac{2r^2}{w^2}\right)^l \exp(-2r^2/w^2) \frac{1}{\pi} \cos^2(l\theta), \quad (4.1)$$

where r and u are the radial and azimuthal coordinate, respectively. The waist parameter is given by $w^{-2} = k_0a/2$, and the frequency separation between consecutive high-order modes with increasing l is constant at $\delta v = ac/(2\pi n_0^2)$, where c is the speed of the light.

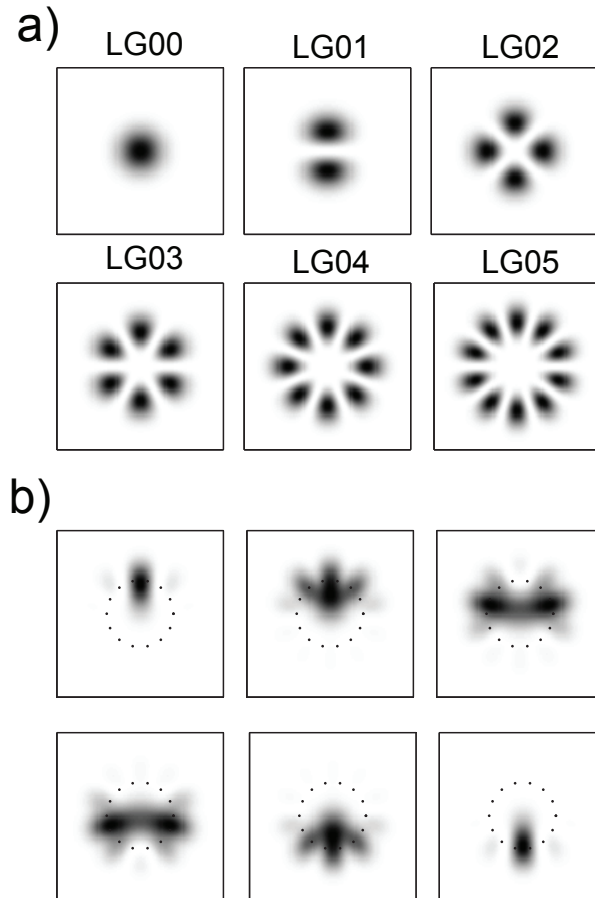


Figure 54: a) The first six order of LG modes calculated from equation (4.1). b) Moving spots generated by interference of the six lowest order LG daisy modes. The diagram shows the calculated intensity versus position on a mode-locked VCSEL for constant time steps between $t = 0$ and $1/(2\delta v)$, the time it takes the spots to move half the circle.

Figure 54(a) shows the profile of a few LG modes calculated by Equation (4.1). Since the LG modes have constant frequency difference, locking these modes so that they are exactly in phase at times $t = n/(\delta\nu)$ (where n is integer), produces two bright spots going around a circle in opposite directions with frequency $\delta\nu$. Figure 54(b) shows the motion of the spots for half a period, calculated under the assumption that the fields of the modes can be superposed linearly and that nonlinear effects are weak. The diagram shows that the emission spot evolves during the motion due to the discrete nature of the modes.

Unfortunately, as shown in Figure 55(a), the mode spacing of our laser is not constant. Presumably, small deviations from a perfectly parabolic index profile (seen in the non-perfect circular symmetry in the mode shapes of Fig. 53) lead to the deviation from even spacing. The non-perfect circular symmetry also breaks down the degeneracies of the LG modes with $\pi/2$ phase shift, such as LG_{01} and LG_{01^*} at 850.25 and 850.20 nm.

Although we do not expect periodic mode-locking when the modes are not evenly spaced, we can still see pulsed behavior. Based on the mode images and frequencies from Fig. 53, we calculate the time dependence of the emission pattern of the measured VCSEL by simple superposition. The theoretical time-resolved emission from the center strip of the VCSEL is shown in Fig. 55(b). There are two types of mode-beating patterns: one is the mode interference between different order of LG modes such as LG_{00} , LG_{01} and LG_{02} etc. The beating frequency is on the order of 100 GHz. On the top of the fast mode beating, there is slowly varying modulation which is on the order of 20 GHz. This slow modulation is caused by the splitting between two degenerate modes such as LG_{01} and LG_{01^*} . For proper mode-locking operation, the slow modulation should be avoided.

Under normal circumstances, a VCSEL will not start mode-locking automatically. It usually requires some mechanism to synchronize the phase of different transverse modes first. In the experiments, we used ultrafast pulse injection to give all the lasing modes a well-defined starting phase, as in the work of [72]. Figure 56 shows the time-resolved emission at two lasing mode maxima after an injected 150 fs laser pulse. The injection laser was focused into one of the lasing maxima located at the side of the emission aperture. The VCSEL started to produce pulsed emission after the laser excitation. The time intervals between pulses are not constant, and the mode-locked pulse can not be sustained, as expected for

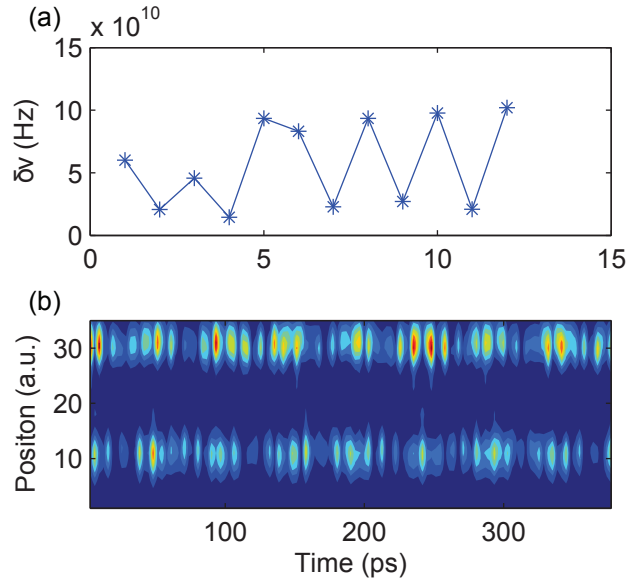


Figure 55: (a) Experimental frequency difference between adjacent LG modes at bias current 8 mA for the modes shown in Fig. 53. (b) Theoretically calculated time-resolved emission from the center strip of the VCSEL with modes shown in Fig. 53.

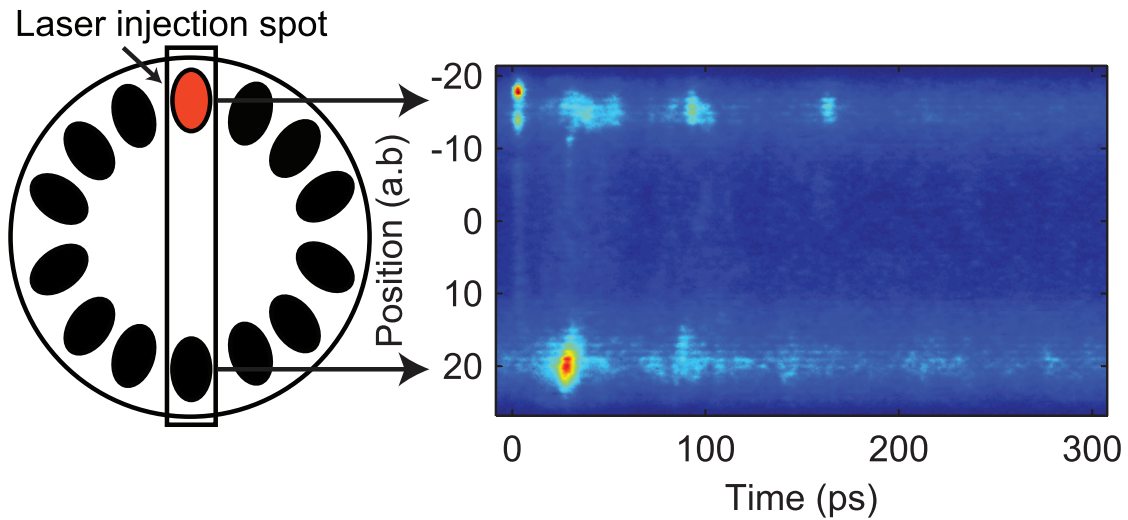


Figure 56: The streak camera image of a VCSEL's emission (the slice of the VCSEL as shown on the left) after a laser pulse injection at one of the VCSEL emission mode maxima. This VCSEL has broader active region than the VCSEL used in Fig. 53 and 55.

non-equidistant mode spacing.

We have spatial-spectrally resolved the emission from commercial oxide-confined VCSELs. Our studies show that LG transverse modes can be used to mode-lock the lasers. Subject to the synchronization of ultrafast laser injection, the laser shows irregular pulsation effects. For excitation of evenly spaced LG modes in energy, we need a well-defined parabolic index of refraction profile. Here, the temperature-indexed parabolic index of refraction profile has asymmetrical shape which leads to non-periodic pulsing. In the future, we propose to introduce a built-in parabolic index of refraction profile by tuning the material index during the growth process.

4.2 ULTRAFAST SWITCHING DYNAMICS OF NONLASING MODES OF VERTICAL-CAVITY SURFACE-EMITTING LASERS

Vertical-cavity surface-emitting lasers (VCSELs) have been widely used in optical communication and laser spectroscopy. A VCSEL's cavity, which is typically one and a half wavelength long, will support only one longitudinal mode and a few transverse modes. By lateral optical confinement, the number of lasing transverse modes can be controlled. One of the methods is to use oxidized AlGaAs layers as an aperture which provides excellent optical guiding and current injection confinement. To achieve single-mode operation of VCSELs, the oxide aperture usually is about $3 \mu m$ [77]. Due to the directional asymmetry, e.g. crystal structure, strain, etc., the emission of a single-mode VCSEL usually has one preferred polarization [77]. However, under high frequency or high current modulation, single-mode VCSELs can have multimode emissions which can contaminate the quality of the single-mode emission.

In this section we demonstrate a new method to study the lifetime and round-trip gain of nonlasing modes of single-mode VCSELs and investigate the GHz/THz behavior of VCSELs for ultrafast all-optical switching. Many time-resolved measurements of VCSELs have used off-resonant injection to introduce an ultrafast current pulse [78, 77, 79]. Here, femtosecond (fs) laser pulses with center wavelength resonant to the VCSEL's emission wavelength were injected into a sample laser to perturb the intra-cavity light field directly. After the optical

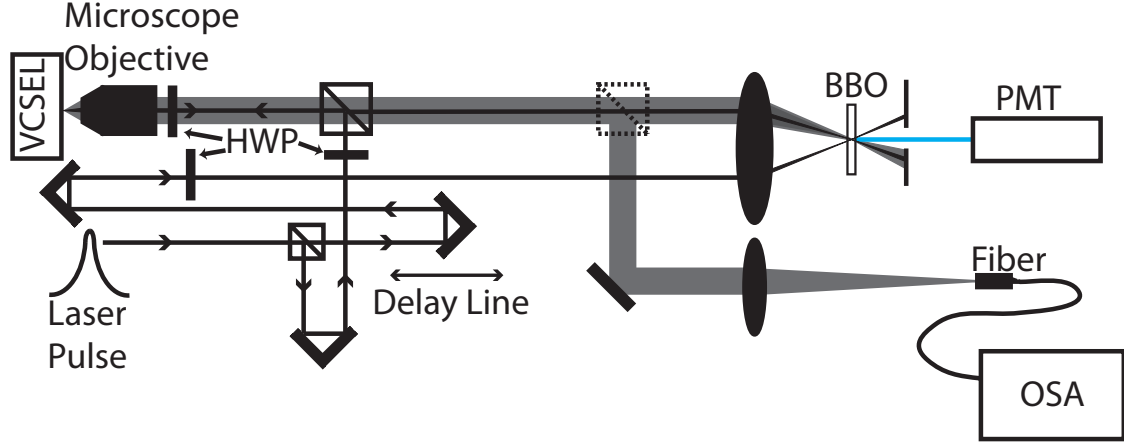


Figure 57: The schematics of the optical up-conversion pump-probe experiment setup.

injection, the subsequent emission dynamics of the lasing and nonlasing modes of the VCSELs were measured by a pump-probe optical up-conversion technique [72, 79].

The single-mode VCSELs we investigated are commercial oxide-confined lasers. The lasing threshold is 1.0 mA and the center emission wavelength is around 852 nm. The oxide aperture tightly restricts the optical emission window to suppress high-order transverse modes. Above the threshold, the VCSEL's emission is linearly polarized and shows redshift with increasing injection current. To investigate the nonlasing mode behavior, we used cross-polarized injection geometry (e.g. the VCSEL's emission polarization is perpendicular to that of the injected laser pulses). The laser pulses were produced by a mode-locked Ti:Sapphire oscillator pumped by a solid state Nd:YVO₄ laser. The center wavelength of the fs laser pulses was tuned to 852 nm, with 200 fs duration, which covers all the emission wavelength range of our single-mode VCSELs.

Figure 57 shows the schematic experimental setup. The injection laser pulse polarization was controlled by a half waveplate. In front of the VCSEL, there is another half waveplate to rotate the polarization of VCSEL's emission. The reflected pump laser pulses, VCSEL emission and probe laser pulses were focused onto a nonlinear β -bariumborate(BBO) crystal. Type-I phase matching was used in the experiment to have better quantum efficiency for weak continuous wave (CW) emission from the VCSEL. A slit can block most of the strong

Ti:Sapphire laser pulses by taking advantage of the cross-correlation setup. A BG40 color filter further suppresses non-upconverted signals. Up-converted signals were detected by a photomultiplier tube (PMT) which is only sensitive to 300 to 650 nm wavelength. The scan delay stage and data acquisition system were controlled by a Labview program. Usually, we measured each time-resolved emission trace 100 times and averaged them in order to get a better signal-to-noise ratio. The pump laser was focused down to a few μm and injected into a VCSEL by a microscope objective. A charge-coupled device (CCD) camera monitored the emission pattern and helped locate the injection position. This all-optical up-conversion technique can have pump laser pulse-width-limited time resolution [78].

Due to the temperature-induced parabolic refraction index profile of VCSELs, they usually emit Laguerre-Gaussian (LG) modes[74] which are given by:

$$I(r, \theta) = \frac{4}{l!} \frac{1}{w^2} \left(\frac{2r^2}{w^2}\right)^l \exp(-2r^2/w^2) \left[\frac{1}{\pi} \cos^2(l\theta)\right] \quad (4.2)$$

where r and θ are the radial and azimuthal coordinates, respectively. The waist parameter is given by $w^{-2} = k_0 a/2$, and the frequency separation between consecutive high-order modes with increasing l is constant at $\delta v = ac/(2\pi n_0^2)$, where c is the speed of the light.

Figure 58 presents a VCSEL emission pattern and spectrum under different bias currents. Above the lasing threshold, the VCSEL emits a LG_{00} mode with linear polarization and 3 μm waist. Below the lasing threshold, the spectrum of VCSEL has three distinct peaks at 849.2 nm, 851.1nm and 852.1 nm. On the mode image, there is an additional ring-like mode around the emission center which are higher order transverse modes, as shown in Figure 58(a).

At constant bias current, the single-mode VCSEL we studied has linearly polarized emission. In this experiment, the polarization of the pump laser was perpendicular to that of VCSEL's emission. We only detected the signal with same polarization as the pump laser. There are two types of dynamics of the VCSEL after strong and fast optical modulation. Figure 59 (a) shows a slowly varying emission which is the relaxation oscillation due to the interplay between cavity photon density and carrier density. On the other hand, within the first 20 ps, the VCSEL emission has a faster and irregular oscillation pattern which is optical

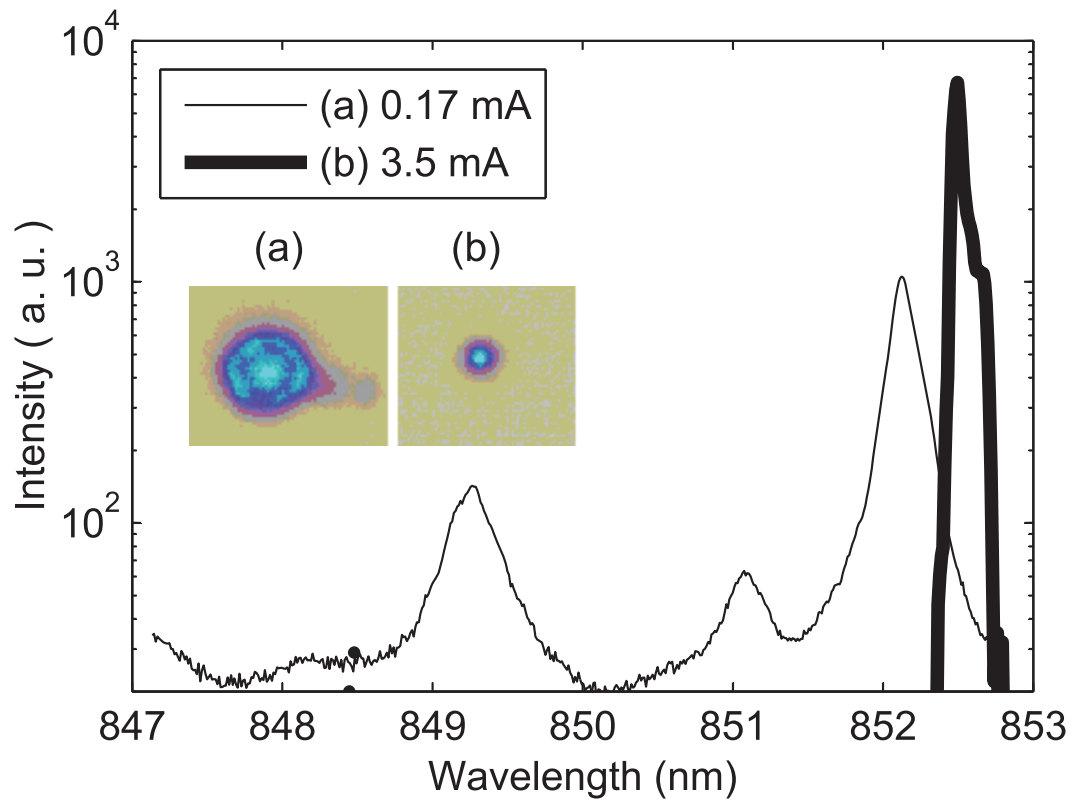


Figure 58: Continuous-wave emission spectra of a single-mode VCSEL below (thin line) and above (heavy line) the lasing threshold. Inset images: near-field emission patterns for (a) below, and (b) above threshold. The intensities do not have the same scale.

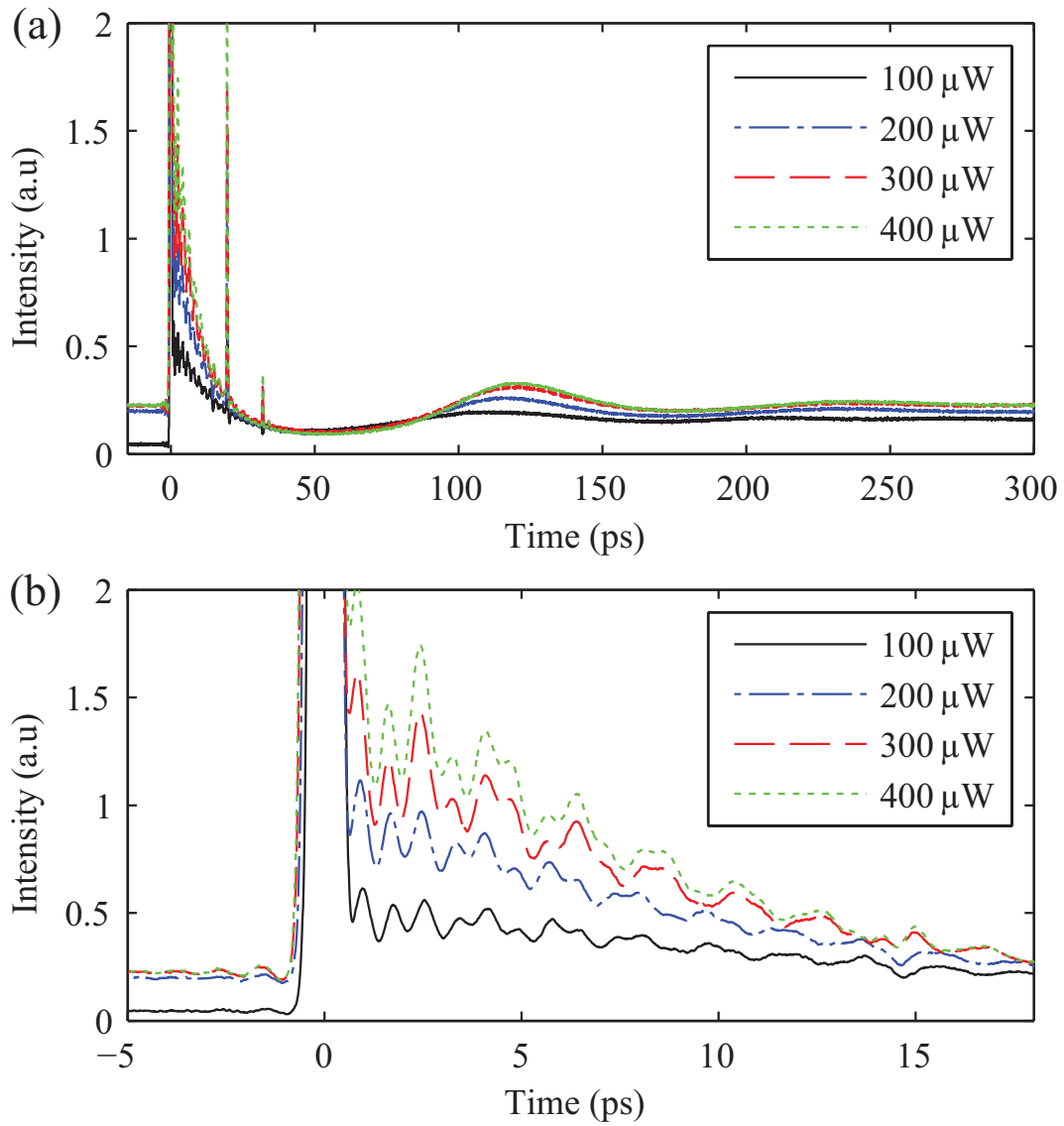


Figure 59: Time-resolved emission of the VCSEL's nonlasing modes after optical injection at one of the lasing emission maximum, where the strong spikes in the (a) are reflected pump laser pulses.

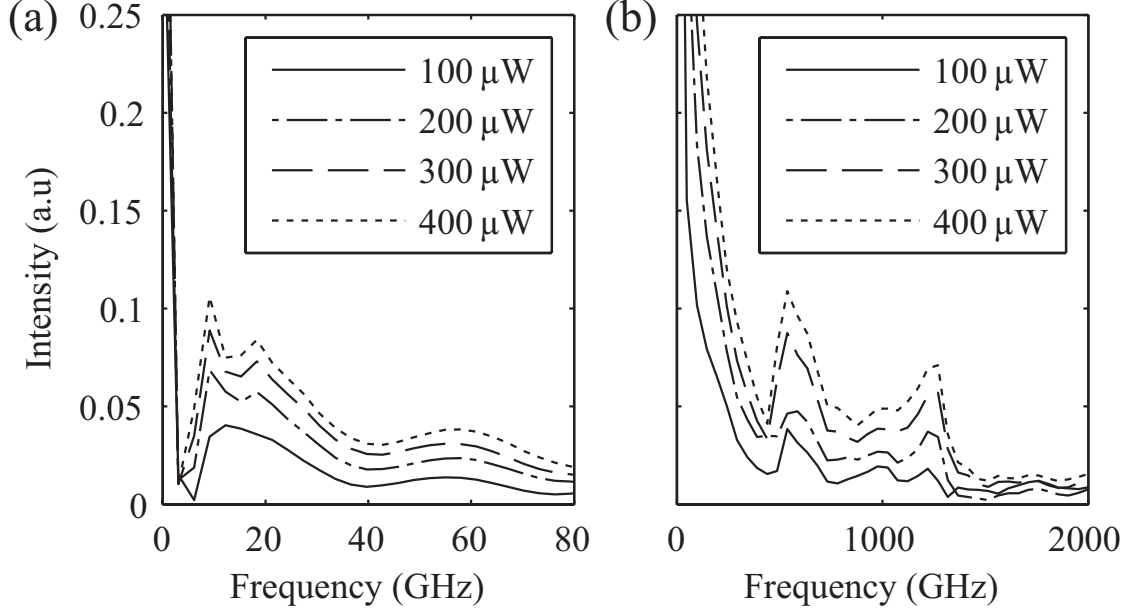


Figure 60: (a) and (b) are the Fourier transform of Fig. 59 (a) and (b), respectively.

beating of different VCSEL emission modes. By doing the Fourier transform of the time-resolved VCSEL emission, shown in Figure 59, we found the relaxation oscillation frequency of 10 GHz and optical beating frequencies of 540 GHz and 1.2 THz. The optical beating frequencies are close to the mode spacing for the different emission peaks below the lasing threshold, seen in Figure 58. The spacings between different peaks are 414 GHz, 789 GHz and 1202 GHz. Since we were detecting the signal whose polarization is perpendicular to the VCSEL's lasing emission, we were actually measuring the VCSEL's nonlasing modes excited by the resonantly injected fs laser pulses.

At high bias current and high pump laser power, these nonlasing modes live much longer and emit light for longer periods than the pump laser repetition time. In other words, the cross-polarized nonlasing VCSEL modes can be “switched on” and begin to lase. To measure the lifetime of these modes, we needed to suppress the slowly varying relaxation-oscillation background. With very low injection laser power, the relaxation oscillations were limited. Figure 61 shows the nonlasing modes' emission after injected laser pulses. The inset depicts

the decay rate of the sub-threshold modes versus bias current. The decay rate falls strongly as the current goes towards threshold (1 mA) and then saturates around a value of 0.05/ps, at which point the original nonlasing modes tend to lase.

In the absence of the external pump, the lasing mode prevents other modes from lasing, since the total carrier density is clamped: higher carrier density causes greater lasing gain, which shortens the carrier lifetime and thus limits the carrier density. However, when a seed pulse from the external pump excites the cross-polarized mode, this mode can win out over the main mode. Our measurements of the main lasing mode power show that it decreases to well below the power of the cross-polarised mode when lasing in the cross-polarized mode is switched on. The short lifetime of the carrier states emitting the cross-polarized mode means that carriers will continually refill these states rather than scatter into the states which participate in the main lasing mode. As shown in Figure 61, at a current of 3 mA, the sub-threshold mode becomes stable and has nearly no decay at late times during the 16 ns pulse repetition time of the Ti:sapphire laser if the injected pulse energy is high enough.

Although lasing in the cross-polarized mode is undesirable for single-mode operation, it is promising for ultrafast optical polarization switching [80, 81, 82]. With this system at the proper bias condition, the polarization of VCSELs can be switched with an external trigger light pulse. Our studies show that this system can work as an optical memory which changes its steady-state polarization, with switching due to an injection pulse on time scales of 100 fs. The injected pulse causing the polarization switching also induces fast transient intensity oscillations which last for about 15 ps and slow relaxation oscillations which last about 150 ps.

In conclusion, luminescence up-conversion with cross-polarized resonant femtosecond optical pulse injection is a powerful method for studying VCSEL emission dynamics. Our measurements show that the emission polarization can be switched into different metastable states on ultrafast time scales.

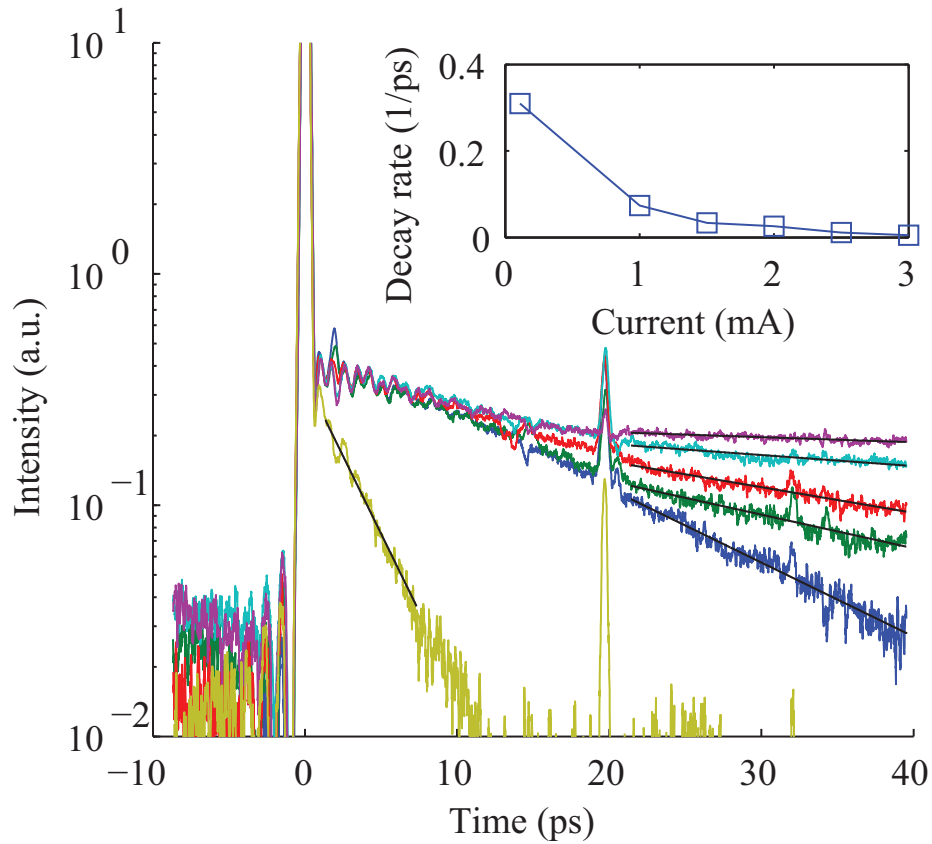


Figure 61: Time-resolved emission dynamics of a VCSEL for different injection currents after optical femtosecond pulse injection that is sufficiently weak (~ 0.8 pJ) to reduce relaxation oscillation. The black solid lines are exponential fittings. Inset: Fitted decay rate versus current, for the times after 20 ps. The spike at 20 ps is an artifact of reflected light from the back surface of a reflective neutral-density filter.

5.0 CONCLUSIONS AND FUTURE WORK

In this thesis, I used two types of time-resolved experimental apparatuses (Chapter 2) to study three different GaAs semiconductor devices: hierarchically self-assembled GaAs/AlGaAs quantum dots(Chapter 3), oxide-confined vertical-cavity surface-emitting lasers (Chapter 4) and GaAs microdisk lasers (Appendix). The size of these devices are on the nanometer or micron scale, which has huge potential for highly integrated solid-state device. The structures are relatively simple, which make them good test beds for some basic physical principles such as conditional quantum gates, coherent control etc. On the other hand, these devices are easily scalable to larger size. I constructed a tunable Kerr-lens mode-locked Ti:Sapphire laser oscillator which serves as the main laser source for my most of experiments (2.2).

For the quantum dots experiment, I studied both high density and low density quantum dots samples. The most interesting part was the ability to address individual quantum dots without physically isolating the dots. This was done by sharp resonant pulse excitation into the dots (Sec. 3.2). Through studying the time-resolved multi-excitonic photoluminescence, I found some evidence of the process that a biexciton turns into a positive trion by tunneling out of an electron. With a well-prepared two-color double pulse, the conditional quantum gate operation for the exciton and biexciton system can be demonstrated in the future work.

For the oxide-confined multimode VCSELs, I clearly resolved the spatial distribution for different LG modes (Sec. 4.1). The preliminary data and simulation show the transverse mode-locking can be achieved with proper mode-spacing and dispersion compensation. I also studied the nonlasing mode dynamics of single-mode VCSELs. The possibility of a femtosecond polarization effect has been demonstrated (Sec. 4.2).

As discussed in the Appendix, the whispering-gallery mode dynamics of a GaAs microdisk laser were measured at the cryogenic temperature. The turn-on delay and the wavelength

shifting for the lasing mode were measured. Future detailed measurements of lasing mode with different pump location should help understanding of how the carriers diffuse.

APPENDIX

MICRODISK LASER

Semiconductor microresonators have a lot of interest as a very good condensed matter physics system and have a variety of possible applications. Semiconductor microresonators usually have sizes of $2\ \mu\text{m}$ to $15\ \mu\text{m}$ which are easy to incorporate in integrated optical circuits. Benefitting from small size and high optical confinement, microdisk lasers usually have very low threshold and small power consumption. Most prior work on microdisk lasers has focused on the static lasing threshold and wavelength measurements [83, 84, 85]. Luo et al. [86] did some dynamics measurement of GaAs/AlGaAs microdisk lasers. They found their microdisk lasers usually have more than 100 ps turn-on delay due to the carrier diffusion time, and this delay decreases with increasing pump power. In this chapter, some preliminary experiment data are shown for the emission dynamics of a GaAs microdisk laser at the cryogenic temperature.

A.1 WHIPERING GALLERY MODES

The lasing modes of microdisk lasers are called whispering-gallery modes, named after their acoustic counterparts. In Beijing, China, there is a “whispering wall” built in 1420 which has a diameter of 62 meter. The acoustic wave can travel along the whispering wall for several tens of meters due to precise and smooth surface of the wall. By contrast, the microdisk laser is around $10\ \mu\text{m}$ in diameter, which is too small for sound but suitable for an optical

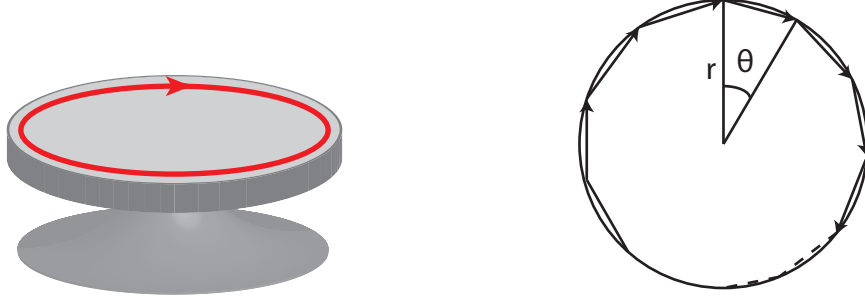


Figure 62: A cartoon of whispering gallery modes.

wave. At the interface of the microdisk and surrounding air, the discontinuity of refractive index provides a strong optical guiding effect. The optical wave experiences total internal reflection at the interface and circulates around the edge of the microdisk, as shown in Fig. 62.

The microdisk lasers I studied are GaAs microdisk lasers which are very similar to the samples in Ref. [83]. The microdisks are generated by electron-beam lithography and reactive ion etching. The disks have a diameter of 12.6 μm and contain four 10 nm GaAs quantum wells separated by $\text{Al}_{0.28}\text{Ga}_{0.72}\text{As}$ barriers. By undercutting with a selective wet etch, the 500 nm pedestals, made of $\text{Al}_{0.65}\text{Ga}_{0.35}\text{As}$, are formed. In order to reduce the surface recombination, the microdisks are passivated in ammonium sulphide and stabilized with a 30-nm-thick silicon nitride encapsulation [83].

Compared to the lateral dimension size of 12 μm , the thickness of the disk is very small, less than 100 nm. Optical modes are mostly confined in the two-dimensional disk, which reduce the calculation of the whispering gallery mode into a two-dimensional Helmholtz equation [83]

$$(\nabla^2 + k^2 n_{\text{eff}}^2)u = 0 \quad (\text{A.1.1})$$

where n_{eff} is the effective refractive index of microdisk and k is the laser wave vector. The solution for Eq. (A.1.1) is the well-known Bessel function,

$$u_{m,n}(R, \theta) \propto J_{m,n}(k_m^n n_{\text{eff}} r) \exp(im\theta) \quad (\text{A.1.2})$$

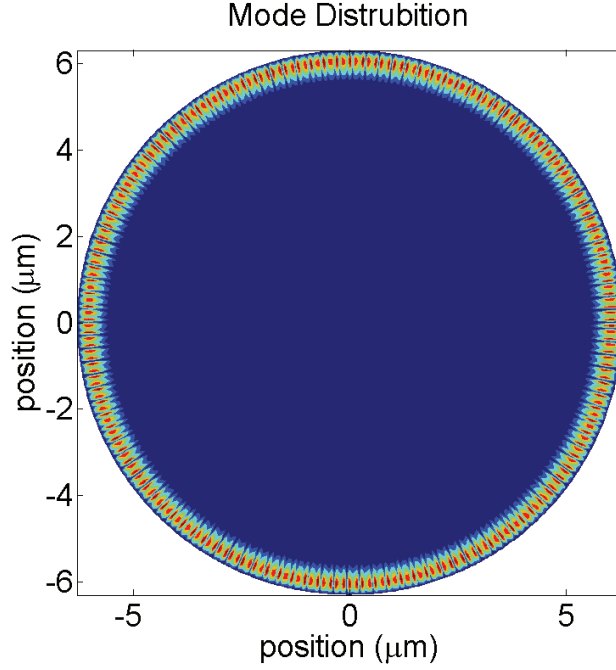


Figure 63: Simulated whispering gallery modes.

where r is the radius of microdisk.

The laser mode should propagate along the edge of the disk laser. Therefore, the boundary condition is the $n = 1$ zero of the Bessel function overlaps with the edge of the disk [83]. Fig. 63 shows a calculated whispering gallery mode on a disk with $6.3 \mu\text{m}$ radius and the lasing wavelength of 812 nm , from Eq. (A.1.2).

Fig. 64 shows a mode image for our microdisk laser. The microdisk laser was placed inside a continuous flow microcrystal and kept at the temperature of 10 K . The confocal microscope was used to collect the microdisk laser emission under the femtosecond laser pump. The two images in Fig. 64 are measured with different pump location. In the left image, the pump beam is located around the center of the disk. In the right image, the pump beam is located on the edge of the disk. As mentioned above, the lasing mode overlaps with the edge of the disk. Therefore, when pumping at the edge of disk, the lasing mode gets the maximum gain from the pump laser. As Fig. 64 shows, the left image is a nonlasing emission and the right image is a lasing mode. The lasing emission pattern (Fig. 64 is blurred and

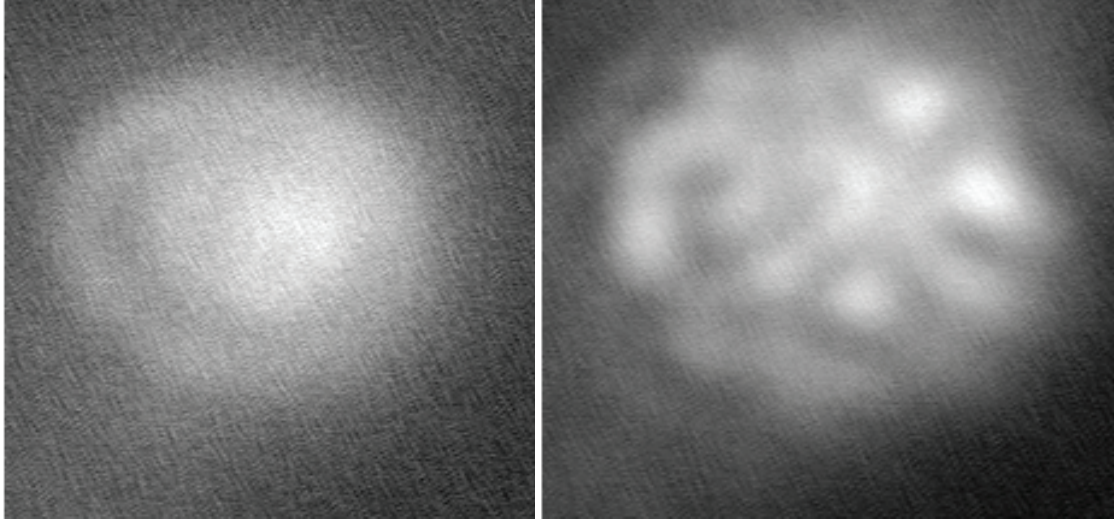


Figure 64: The measured whispering gallery modes image with different pump location, (a) on the disk center and (b) on the edge of the disk.

cannot resolve the actual mode distribution due to the limit resolution of our setup.

A.2 TIME DEPENDENT MEASUREMENTS

The dynamics of microdisk laser emission were investigated with a streak camera setup similar to Fig. 44. I did not use the pulse shaper in this experiment.

Fig. 65 is the emission dynamics of a microdisk laser after a femtosecond laser pulse. The first thing I noticed is that the lasing emission starts at about 15 ps after the pump laser arrival. This turn-on delay is much shorter than that of Ref. [86]. The carrier thermalization and cooling effect should contribute most to this turn-on delay. After the lasing started, the lasing wavelength shifted to longer wavelength with increasing time. This is can be understood in terms of the carrier induced refractive index change. With increasing time, the excited carrier density reduces and the refractive index will become smaller. From Eq. (A.1.1), we know the lasing wavelength should become longer. Another interesting

phenomena is that there are two peaks for the lasing mode. This splitting is due to clockwise whispering gallery mode and counter-clockwise whispering gallery mode interaction with each other.

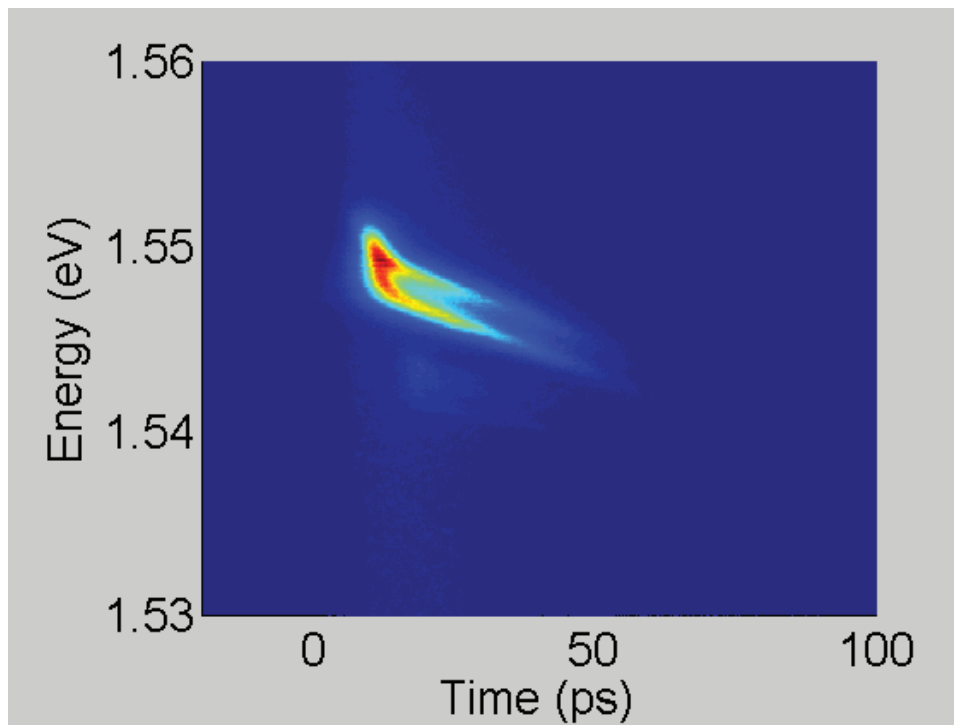


Figure 65: Time resolved whispering gallery modes.

BIBLIOGRAPHY

- [1] S.M. Sze and K.K. Ng. *Physics of Semiconductor Devices*. Wiley-Blackwell, 2007.
- [2] M.R. Brozel and G.E. Stillman. *Properties of Gallium Arsenide*. Inspec/IEEE, 1996.
- [3] C.W. Wilmsen, H. Temkin, and L.A. Coldren. *Vertical-cavity Surface-emitting Lasers: Design, Fabrication, Characterization, and Applications*. Cambridge University Press, 2001.
- [4] P.F. Moulton. Spectroscopic and laser characteristics of $\text{Ti:Al}_2\text{O}_3$. *Journal of the Optical Society of America B*, 3(1):125–133, 1986.
- [5] U. Keller. Recent developments in compact ultrafast lasers. *Nature*, 424(6950):831–838, 2003.
- [6] A.G. Baca and C.I.H. Ashby. *Fabrication of GaAs Devices*. Peter Peregrinus Ltd, 2005.
- [7] R.N. Hall, G.E. Fenner, J.D. Kingsley, T.J. Soltys, and R.O. Carlson. Coherent light emission from GaAs junctions. *Physical Review Letters*, 9(9):366–368, 1962.
- [8] Z.I. Alferov. Nobel Lecture: The double heterostructure concept and its applications in physics, electronics, and technology. *Reviews of Modern Physics*, 73(3):767–782, 2001.
- [9] H. Kroemer. A proposed class of hetero-junction injection lasers. *Proceedings of the IEEE*, 51(12):1782–1783, 1963.
- [10] A.Y. Cho and J.R. Arthur. Molecular beam epitaxy. *Progress in Solid State Chemistry*, 10(Part 3):157 – 191, 1975.
- [11] H.M. Manasevit. Single-crystal gallium arsenide on insulating substrates. *Applied Physics Letters*, 12:156, 1968.
- [12] D.W. Snoke. *Solid State Physics: Essential Concepts*. Addison-Wesley, 2009.
- [13] H. Kroemer. Quasi-electric and quasi-magnetic fields in nonuniform semiconductors. *RCA Review*, 18(3):332 – 342, Sept. 1957.

- [14] R. Dingle, W. Wiegmann, and C.H. Henry. Quantum states of confined carriers in very thin $\text{Al}_x\text{Ga}_{1-x}\text{As-GaAs-Al}_x\text{Ga}_{1-x}\text{As}$ heterostructures. *Physical Review Letters*, 33:827, 1974.
- [15] D. J. Eaglesham and M. Cerullo. Dislocation-free Stranski-Krastanow growth of Ge on Si(100). *Physical Review Letters*, 64(16):1943–1946, 1990.
- [16] A. Rastelli, S. Stuffer, A. Schliwa, R. Songmuang, C. Manzano, G. Costantini, K. Kern, A. Zrenner, D. Bimberg, and O.G. Schmidt. Hierarchical self-assembly of GaAs/AlGaAs quantum dots. *Physical Review Letters*, 92(16):166104–166104, 2004.
- [17] W.W. Chow and S.W. Koch. *Semiconductor-Laser Fundamentals: Physics of the Gain Materials*. Springer Verlag, 1999.
- [18] K. Iga. Surface-emitting laser-its birth and generation of new optoelectronics field. *Selected Topics in Quantum Electronics, IEEE Journal of*, 6(6):1201–1215, 2002.
- [19] E.W. Young, K.D. Choquette, S.L. Chuang, K.M. Geib, A.J. Fischer, and A.A. Allerman. Single-transverse-mode vertical-cavity lasers under continuous and pulsed operation. *Photonics Technology Letters, IEEE*, 13(9):927–929, 2002.
- [20] J. Shah. *Ultrafast Spectroscopy of Semiconductors and Semiconductor Nanostructures*. Springer Verlag, 1999.
- [21] F.X. Kartner. *Few-cycle Laser Pulse Generation and Its Applications*. Springer Verlag, 2004.
- [22] F.J. McClung and R.W. Hellwarth. Giant optical pulsations from ruby. *Journal of Applied Physics*, 33:828, 1962.
- [23] N. Taylor. *LASER: The Inventor, the Nobel Laureate, and the Thirty-year Patent War*. Simon and Schuster, 2001.
- [24] R.L. Fork, B.I. Greene, and C.V. Shank. Generation of optical pulses shorter than 0.1 psec by colliding pulse mode locking. *Applied Physics Letters*, 38:671, 1981.
- [25] T. Brabec, C. Spielmann, and E. Krausz. Mode locking in solitary lasers. *Optics Letters*, 16(24):1961–1963, 1991.
- [26] D.E. Spence, P.N. Kean, and W. Sibbett. 60-fsec pulse generation from a self-mode-locked Ti:Sapphire laser. *Optics Letters*, 16(1):42–44, 1991.
- [27] A. Weiner. *Ultrafast Optics*. John Wiley & Sons Inc, 2009.
- [28] Y.R. Shen. Electrostriction, optical Kerr effect and self-focusing of laser beams. *Physics Letters*, 20(4):378–380, 1966.

- [29] G. Agrawal. Nonlinear Fiber Optics. *Nonlinear Science at the Dawn of the 21st Century*, pages 195–211, 2000.
- [30] J.C. Diels and W. Rudolph. *Ultrashort Laser Pulse Phenomena*. Elsevier London, 2006.
- [31] B.E. Lemoff and C.P.J. Barty. Cubic-phase-free dispersion compensation in solid-state ultrashort-pulse lasers. *Optics letters*, 18(1):57–59, 1993.
- [32] R. Szipocs, K. Ferencz, C. Spielmann, and F. Krausz. Chirped multilayer coatings for broadband dispersion control in femtosecond lasers. *Optics Letters*, 19(3):201, 1994.
- [33] F. Gires and P. Tournois. Interféromètre utilisable pour la compression d'impulsions lumineuses modulées en fréquence. *Comptes rendus de l'Académie des sciences*, 258(5):6112–6115, 1964.
- [34] N. Matuschek, F.X. Kartner, and U. Keller. Theory of double-chirped mirrors. *IEEE Journal of Selected Topics in Quantum Electronics*, 4(2):197–208, 1998.
- [35] N. Matuschek, L. Gallmann, D.H. Sutter, G. Steinmeyer, and U. Keller. Back-side-coated chirped mirrors with ultra-smooth broadband dispersion characteristics. *Applied Physics B: Lasers and Optics*, 71(4):509–522, 2000.
- [36] H. Kogelnik and T. Li. Laser beams and resonators. *Applied Optics*, 5(10):1550–1567, 1966.
- [37] T. Brabec, C. Spielmann, P.F. Curley, and F. Krausz. Kerr lens mode locking. *Optics letters*, 17(18):1292–1294, 1992.
- [38] H.A. Haus. Theory of mode locking with a fast saturable absorber. *Journal of Applied Physics*, 46:3049, 1975.
- [39] C. Spielmann, P.F. Curley, T. Brabec, and F. Krausz. Ultrabroadband femtosecond lasers. *IEEE Journal of Quantum Electronics*, 30(4):1100–1114, 1994.
- [40] F. Krausz, M.E. Fermann, T. Brabec, P.F. Curley, M. Hofer, M.H. Ober, C. Spielmann, E. Wintner, and A.J. Schmidt. Femtosecond solid-state lasers. *IEEE Journal of Quantum Electronics*, 28(10):2097–2122, 1992.
- [41] H. Kogelnik, E. Ippen, A. Dienes, and C. Shank. Astigmatically compensated cavities for cw dye lasers. *IEEE Journal of Quantum Electronics*, 8(3):373–379, 1972.
- [42] A.P. Heberle, J.J. Baumberg, E. Binder, T. Kuhn, K. Kohler, and K.H. Ploog. Coherent control of exciton density and spin. *IEEE Journal of Selected Topics in Quantum Electronics*, 2(3):769–775, 1996.
- [43] D.W. Marquardt. An algorithm for least-squares estimation of nonlinear parameters. *Journal of the Society for Industrial and Applied Mathematics*, 11(2):431–441, 1963.

- [44] E. B. Treacy. Compression of picosecond light pulses. *Physics Letters A*, 28(1):34 – 35, 1968.
- [45] E.G. Loewen, M. Neviere, and D. Maystre. Grating efficiency theory as it applies to blazed and holographic gratings. *Applied Optics*, 16(10):2711–2721, 1977.
- [46] R.W. Boyd. *Nonlinear Optics*. Boston: Academic Press, Inc, 1992.
- [47] J.E. Midwinter and J. Warner. The effects of phase matching method and of uniaxial crystal symmetry on the polar distribution of second-order non-linear optical polarization. *British Journal of Applied Physics*, 16:1135, 1965.
- [48] B. Zhang, D.W. Snoke, and A.P. Heberle. Trion formation in GaAs-AlGaAs quantum dots by tunneling. *Submitted*, 2010.
- [49] Z. Yuan, B.E. Kardynal, R.M. Stevenson, A.J. Shields, C.J. Lobo, K. Cooper, N.S. Beattie, D.A. Ritchie, and M. Pepper. Electrically driven single-photon source. *Science*, 295(5552):102–105, 2002.
- [50] A. Barenco, D. Deutsch, A. Ekert, and R. Jozsa. Conditional quantum dynamics and logic gates. *Physical Review Letters*, 74(20):4083–4086, 1995.
- [51] D. Bimberg and C. Ribbat. Quantum dots: lasers and amplifiers. *Microelectronics Journal*, 34(5-8):323–328, 2003.
- [52] U. Bockelmann, W. Heller, A. Filoramo, and Ph. Roussignol. Microphotoluminescence studies of single quantum dots. I. Time-resolved experiments. *Physical Review B*, 55(7):4456–4468, 1997.
- [53] L. Landin, M.S. Miller, M.E. Pistol, C.E. Pryor, and L. Samuelson. Optical Studies of Individual InAs Quantum Dots in GaAs: Few-Particle Effects. *Science*, 280(5361):262–264, 1998.
- [54] D.V. Regelman, E. Dekel, D. Gershoni, E. Ehrenfreund, A.J. Williamson, J. Shumway, A. Zunger, W.V. Schoenfeld, and P.M. Petroff. Optical spectroscopy of single quantum dots at tunable positive, neutral, and negative charge states. *Physical Review B*, 64(16):165301, 2001.
- [55] C. Santori, G.S. Solomon, M. Pelton, and Y. Yamamoto. Time-resolved spectroscopy of multiexcitonic decay in an InAs quantum dot. *Physical Review B*, 65(7):073310, 2002.
- [56] M. Koch, K. Kheng, IC Robin, and R. André. Biexcitonic complexes and the decay dynamics of trion and exciton in a single CdSe quantum dot. *Physica Status Solidi (c)*, 3(11):3916–3919, 2006.
- [57] L. Wang, V. Křápek, F. Ding, F. Horton, A. Schliwa, D. Bimberg, A. Rastelli, and O.G. Schmidt. Self-assembled quantum dots with tunable thickness of the wetting layer: Role of vertical confinement on interlevel spacing. *Physical Review B*, 80(8):85309, 2009.

- [58] H. Gotoh, H. Ando, and T. Takagahara. Radiative recombination lifetime of excitons in thin quantum boxes. *Journal of Applied Physics*, 81(4):1785–1789, 1997.
- [59] M. Tsuchiya, T. Matsusue, and H. Sakaki. Tunneling escape rate of electrons from quantum well in double-barrier heterostructures. *Physical Review Letter*, 59(20):2356–2359, 1987.
- [60] A. Tackeuchi, T. Kuroda, K. Mase, Y. Nakata, and N. Yokoyama. Dynamics of carrier tunneling between vertically aligned double quantum dots. *Physical Review B*, 62(3):1568–1571, 2000.
- [61] S. Haacke, N.T. Pelekanos, H. Mariette, M. Zigone, A.P. Heberle, and W.W. Rühle. Tunneling dynamics in CdTe/(Cd, Zn) Te asymmetric double-quantum-well structures. *Solid State Communications*, 47:16643, 1988.
- [62] D. W. Snoke, J. Hübner, W. W. Rühle, and M. Zundel. Spin flip from dark to bright states in InP quantum dots. *Physical Review B*, 70(11):115329, 2004.
- [63] J.L. Osborne, A.J. Shields, M. Pepper, F.M. Bolton, and D.A. Ritchie. Photoluminescence due to positively charged excitons in undoped GaAs/Al_xGa_{1-x}As quantum wells. *Physical Review B*, 53(19):13002–13010, 1996.
- [64] J.J. Finley, P.W. Fry, A.D. Ashmore, A. Lemaitre, A.I. Tartakovskii, R. Oulton, D.J. Mowbray, M.S. Skolnick, M. Hopkinson, P.D. Buckle, et al. Observation of multi-charged excitons and biexcitons in a single InGaAs quantum dot. *Physical Review B*, 63(16):161305, 2001.
- [65] L. Allen and J.H. Eberly. *Optical Resonance and Two-level Atoms*. Dover publications, 1987.
- [66] B. Zhang, D.W. Snoke, and A.P. Heberle. Toward the transverse mode-locking of VCSELs. *Submitted*, 2010.
- [67] B. Zhang, D.W. Snoke, and A.P. Heberle. Ultrafast switching dynamics of nonlasing modes of vertical-Cavity surface-emitting lasers. *Submitted*, 2010.
- [68] P.J. Delfyett, D.H. Hartman, S.Z. Ahmad, and R.B. Bellcore. Optical clock distribution using a mode-locked semiconductor laserdiode system. *Lightwave Technology, Journal of*, 9(12):1646–1649, 1991.
- [69] D.J. Jones, S.A. Diddams, J.K. Ranka, A. Stentz, R.S. Windeler, J.L. Hall, and S.T. Cundiff. Carrier-envelope phase control of femtosecond mode-locked lasers and direct optical frequency synthesis. *Science*, 288(5466):635, 2000.
- [70] H. Kasuya, M. Mori, R. Goto, T. Goto, and K. Yamane. All optical mode locking of Fabry–Perot laser diode via mutual injection locking between two longitudinal modes. *Applied Physics Letters*, 75:13, 1999.

- [71] W. Jiang, M. Shimizu, R.P. Mirin, T.E. Reynolds, and J.E. Bowers. Femtosecond periodic gain vertical-cavity lasers. *IEEE Photonics Technology Letters*, 5(1):23–24, 1993.
- [72] R. Gordon, A.P. Heberle, and J.R.A. Cleaver. Transverse mode-locking in microcavity lasers. *Applied Physics Letters*, 81(24):4523 – 4525, 2002.
- [73] V. de Lange, K.J. Sun, and R. Gordon. Inside vertical-cavity surface-emitting lasers: Extracting the refractive index from spatial-spectral mode images. *IEEE Journal of Quantum Electronics*, 43(3):225–229, 2007.
- [74] S.F. Pereira, M.B. Willemsen, M.P. van Exter, and J.P. Woerdman. Pinning of daisy modes in optically pumped vertical-cavity surface-emitting lasers. *Applied Physics Letters*, 73(16):2239 – 2241, 1998.
- [75] W. Nakwaski and R.P. Sarzała. Transverse modes in gain-guided vertical-cavity surface-emitting lasers. *Optics Communications*, 148(1-3):63–69, 1998.
- [76] D.T.F. Marple. Refractive index of GaAs. *Journal of Applied Physics*, 35:1241, 1964.
- [77] M. Grabherr, R. Jager, R. Michalzik, B. Weigl, G. Reiner, and K.J. Ebeling. Efficient single-mode oxide-confined GaAs VCSEL’s emitting in the 850-nm wavelength regime. *IEEE Photonics Technology Letters*, 9(10):1304 – 6, 1997.
- [78] T. Yoshikawa, T. Kawakami, H. Saito, H. Kosaka, M. Kajita, K. Kurihara, Y. Sugimoto, and K. Kasahara. Polarization-controlled single-mode VCSEL. *Quantum Electronics, IEEE Journal of*, 34(6):1009–1015, 2002.
- [79] A.J. Ramsay, A.P. Heberle, and J.R.A. Cleaver. Polarization relaxation dynamics of surface-emitting lasers following resonant pulse injection. In *Conference on Lasers and Electro-Optics*. Optical Society of America, 2004.
- [80] M. Kauer, J.R.A. Cleaver, J.J. Baumberg, and A.P. Heberle. Femtosecond dynamics in semiconductor lasers: dark pulse formation. *Applied Physics Letters*, 72(13):1626 – 1628, 1998.
- [81] H. Kawaguchi. Bistable laser diodes and their applications: State of the art. *IEEE Journal on Selected Topics in Quantum Electronics*, 3(5):1254 – 1270, 1997.
- [82] T. Mori, H. Yamayoshi, and H. Kawaguchi. Low-switching-energy and high-repetition-frequency all-optical flip-flop operations of a polarization bistable vertical-cavity surface-emitting laser. *Applied Physics Letters*, 88(24):101102, 2006.
- [83] S.A. Backes, J.R.A. Cleaver, A.P. Heberle, J.J. Baumberg, and K. Köhler. Threshold reduction in pierced microdisk lasers. *Applied Physics Letters*, 74(2):176 – 178, 1999.
- [84] S.L. McCall, A.F.J. Levi, R.E. Slusher, S.J. Pearton, and R.A. Logan. Whispering-gallery mode microdisk lasers. *Applied Physics Letters*, 60(3):289, 1992.

- [85] R.E. Slusher, A.F.J. Levi, U. Mohideen, S.L. McCall, S.J. Pearton, and R. Logan. Threshold characteristics of semiconductor microdisk lasers. *Applied Physics Letters*, 63(10):1310–1312, 1993.
- [86] K.J. Luo, J.Y. Xu, H. Cao, Y. Ma, S.H. Chang, S.T. Ho, and G.S. Solomon. Dynamics of GaAs/AlGaAs microdisk lasers. *Applied Physics Letters*, 77:2304, 2000.
- [87] M. Abbarchi, F. Troiani, C. Mastrandrea, G. Goldoni, T. Kuroda, T. Mano, K. Sakoda, N. Koguchi, S. Sanguinetti, A. Vinattieri, et al. Spectral diffusion and line broadening in single self-assembled GaAs/ AlGaAs quantum dot photoluminescence. *Applied Physics Letters*, 93:162101, 2008.
- [88] I.A. Akimov, A. Hundt, T. Flissikowski, and F. Henneberger. Fine structure of the trion triplet state in a single self-assembled semiconductor quantum dot. *Applied Physics Letters*, 81:4730, 2002.
- [89] R. Gordon, A.P. Heberle, A.J. Ramsay, and J.R.A. Cleaver. Experimental coherent control of lasers. *Physical Review A*, 65(5):51803 – 1, 2002.
- [90] H.A. Haus. Mode-locking of lasers. *IEEE Journal of Selected Topics in Quantum Electronics*, 6(6):1173–1185, 2000.
- [91] K. Hodeck, I. Manke, M. Geller, R. Heitz, F. Heinrichsdorff, A. Krost, D. Bimberg, H. Eisele, and M. Dähne. Multiline photoluminescence of single InGaAs quantum dots. *Physica Status Solidi (c)*, 0(4):1209–1212, 2003.
- [92] F. Houzay, C. Guille, JM Moison, P. Henoc, and F. Barthe. First stages of the MBE growth of InAs on (001)GaAs. *Journal of Crystal Growth*, 81(1-4):67 – 72, 1987.
- [93] J.Y. Marzin, J.M. Gérard, A. Izrael, D. Barrier, and G. Bastard. Photoluminescence of single InAs quantum dots obtained by self-organized growth on GaAs. *Physical review letters*, 73(5):716–719, 1994.
- [94] G. Muñoz-Matutano et al. Exciton, biexciton and trion recombination dynamics in a single quantum dot under selective optical pumping. *Physica E*, 40(6):2100–2103, 2008.
- [95] G.A. Narvaez, G. Bester, and A. Zunger. Excitons, biexcitons, and trions in self-assembled (In, Ga) As/GaAs quantum dots: Recombination energies, polarization, and radiative lifetimes versus dot height. *Physical Review B*, 72(24):245318, 2005.
- [96] Z.G. Pan, S. Jiang, M. Dagenais, R.A. Morgan, K. Kojima, M.T. Asom, R.E. Leibenguth, G.D. Guth, and M.W. Focht. Optical injection induced polarization bistability in vertical-cavity surface-emitting lasers. *Applied Physics Letters*, 63:2999, 1993.
- [97] M.A. Reed, J.N. Randall, R.J. Aggarwal, R.J. Matyi, T.M. Moore, and A.E. Wetsel. Observation of discrete electronic states in a zero-dimensional semiconductor nanostructure. *Physical Review Letters*, 60(6):535–537, 1988.

- [98] M. Scheibner, T. Schmidt, L. Worschech, A. Forchel, G. Bacher, T. Passow, and D. Hommel. Superradiance of quantum dots. *Nature Physics*, 3(2):106–110, 2007.
- [99] A.M. Weiner, D.E. Patel, J.S. Wullert, and R.B. Bellcore. Programmable shaping of femtosecond optical pulses by use of 128-element liquid crystal phase modulator. *IEEE Journal of Quantum Electronics*, 28(4):908–920, 1992.